

THESIS

STORM MICROPHYSICS AND KINEMATICS AT THE ARM-SGP SITE USING DUAL
POLARIZED RADAR OBSERVATIONS AT MULTIPLE FREQUENCIES

Submitted by

Alyssa A. Matthews

Department of Atmospheric Science

In partial fulfillment of the requirements

For the Degree of Master of Science

Colorado State University

Fort Collins, Colorado

Fall 2014

Master's Committee:

Advisor: Steven Rutledge

Venkatachalam Chandrasekar

Russ Schumacher

Brenda Cabell

Copyright by Alyssa A. Matthews 2014

All Rights Reserved

ABSTRACT

STORM MICROPHYSICS AND KINEMATICS AT THE ARM-SGP SITE USING DUAL POLARIZED RADAR OBSERVATIONS AT MULTIPLE FREQUENCIES

This research utilizes observations from the Atmospheric Radiation Measurement (ARM) Climate Research Facility at the Southern Great Plains location to investigate the kinematic and microphysical processes present in various types of weather systems. The majority of the data used was collected during the Mid-latitude Continental Convective Cloud Experiment (MC3E), and utilizes the network of scanning radars to arrive at a multi-Doppler wind retrieval and is compared to vertical wind measurements from a centrally located profiling radar. Microphysical compositions of the storms are analyzed using a multi-wavelength hydrometeor identification algorithm utilizing the strengths of each of the radar wavelengths available (X, C, S). When available, a comparison is done between observational analysis and simulated model output from the Weather Research Forecasting model with Spectral-bin Microphysics (WRF-SBM) using bulk statistics to look at reflectivity, vertical motions, and microphysics.

ACKNOWLEDGEMENTS

I would like to acknowledge my family for their support, and my boyfriend, Joseph Hardin, for the tremendous amount of help and support he has given me. I would also like to thank my advisor, Dr. Steven Rutledge, for his help as well and for his patience and wisdom in guiding my work. I also must thank my committee (Dr. Chandra, Dr. Russ Schumacher, and Dr. Brenda Dolan) for their help and willingness to donate some of their time to help this work along. Finally I would like to thank my Radarmet group members for all of their help and conversation. This research is supported by the DOE ASR grant DE-SC0007016.

TABLE OF CONTENTS

ABSTRACT	ii
ACKNOWLEDGEMENTS	iii
LIST OF TABLES	vi
LIST OF FIGURES	vii
Chapter 1. Introduction	1
1.1. Importance of Model Comparisons	2
1.2. MC3E	3
1.3. Organization	5
Chapter 2. Background	7
2.1. Dual-Polarized Radar	7
2.2. Multi-Doppler Analysis Previous Work	14
Chapter 3. Methodology	18
3.1. Quality Control	18
3.2. Velocity Corrections	22
3.3. Convective-Stratiform Partitioning	23
3.4. Gridding	24
3.5. Multi-Doppler	24
3.6. S-band Profiling Radar	26

3.7. Microphysical Categorization.....	26
3.8. Model	28
Chapter 4. Discussion	30
4.1. Case Analysis.....	30
Chapter 5. Conclusion	88
5.1. Future Work.....	93
BIBLIOGRAPHY	95

LIST OF TABLES

3.1	Reflectivity and differential reflectivity biases for each radar used for each case analyzed.	21
3.2	Characteristics of the scanning radars surrounding the SGP Central Facility used in this research.....	23

LIST OF FIGURES

1.1	Map of radar, profiler, rain guage, and disdrometer location used in this study. Dashed lines are distances in km from the ARM-SGP Central Facility, while solid black and red circles are the dual-Doppler lobes between XSE and CSAPR, and XSE and XSW radars, respectively.	4
2.1	Dual-polarized radar transmits electromagnetic waves in the horizontal and vertical planes. Image courtesy of NOAA NSSL NOAA (2014)	8
2.2	Example of velocity folding. Raw velocity is shown on the left, with a Nyquist velocity of 16.8 ms^{-1} . Corrected velocity is shown on the right with no folding. ...	9
2.3	Z_{dr} as drop shape becomes more oblate. Image from Polarimetric Weather Radar (Bringi and Chandrasekar, 2001)	11
2.4	Z_{dr} as the axis ratio ($frac{AB}$) changes for different types of hydrometeor (Herzogh and Jameson, 1992)	12
2.5	This figure shows the vertical velocities from the dual-Doppler (lines) and profiler (dots). Blue is the minimum vertical velocity, red is the maximum, and green is the mean. The height of the maximum updraft and the maximum of the mean updraft occurs at a height of approximately 6 km for this case. Collis et al. (2013)	17
3.1	Example of radome attenuation. To the Northeast of the radar, the reflectivity drops quickly with range.	19

3.2	Non-Meteorological Echo (yellow circle). This echo has no velocity pattern, no signal quality value, but shows up on reflectivity scans.....	22
3.3	Example of the weighting scheme for the multi-wavelength hydrometeor identification algorithm used in this study.	28
3.4	Hydrometeor Classification for the WRF-SBM over the 43 mass bins and 7 species.	29
4.1	Skew-T showing surface lifted parcel (grey) at 9 UTC from LMN.....	31
4.2	Surface analysis for 9 UTC.....	32
4.3	Surface analysis with overlaid radar from 09 UTC showing surface temperature (filled), surface winds (black barbs), 500 mb winds (green barb), CAPE (color contours), dew points (dashed lines), cell tracking (orange contour). Plot courtesy of Brody Fuchs in the CSU-RADARMET research group.....	33
4.4	Swaths of storm motion through the 08-1130 UTC time period of reflectivity (left), velocity (center), and MWHID (right). Dots show disdrometer locations clustered around the CF.....	34
4.5	Comparison of interpolated profiler and composite radar reflectivity (a, c) and vertical winds (b,d) for 25 April 2011.....	35
4.6	Statistical comparison of profiler vertical winds versus dual-Doppler derived vertical winds. Warm colors indicate updraft, cool colors indicate downdraft, with black indicating the combined mean.....	37
4.7	Gridded image of reflectivity at 2 km with overlaid winds (left) and of hydrometeor classification (right) at 1001 UTC on 25 April 2011.....	38

4.8	Mean vertical velocity from 08-1130 UTC over the entire gridded domain. Purple shows overall mean, red shows updraft velocity, and blue shows downdraft velocity	39
4.9	Reflectivity (a), mean vertical velocity (b), and up/down split mean vertical velocity (c) for the five times chosen to evaluate storm evolution.....	40
4.10	Frequency of each hydrometeor category as a function of height for each of the five chosen times for the 25 April case.....	42
4.11	Reflectivity from the radar (top) and model (bottom) at 0900 UTC.....	43
4.12	Reflectivity CFADs showing radar observations (left) and WRF-SBM simulations (right) for the 25 April 2011 case.....	45
4.13	Vertical Velocity CFADs showing dual-Doppler derived (left) and model simulated (right) vertical motions.....	46
4.14	Normalized frequency of each hydrometeor category with height for Drizzle (DZ), Rain, (RN), Ice Crystals (CR), Aggregates (AG), Wet Snow (WS), Low Density Graupel (LDG), High Density Graupel (HDG), Hail (HA) and Big Drops/Melting Hail (BD/MH).....	48
4.15	Cross section of reflectivity (upper left), vertical velocity (upper right), HID (lower left), and confidence in the HID category (lower right) for the WRF-SBM simulated data. The black outline is the 0 dBZ contour.....	50
4.16	HID frequency for the WRF-SBM simulation with no reflectivity threshold.....	51
4.17	Cross section of the radar observations at 0939 UTC.....	52
4.18	Surface analysis and frontal positions for 0730 UTC on 1 May 2011.....	53

4.19	12 UTC sounding for Lamont, Oklahoma.....	54
4.20	CAPPI of reflectivity (left) and HID (right) with overlaid wind vectors taken at 2 km at 1330 on 01 May 2011.....	55
4.21	Mean vertical velocity over 11-1330 UTC split into upward and downward motions. Upward motion is shown in red and downward motion is shown in blue. Overall mean is purple.....	56
4.22	Maximum and minimum vertical velocity present over the studied region between 11 and 1330 UTC. Purple depicts maximum wind speeds and red depicts minimum wind speeds.....	57
4.23	Mean vertical velocities for the three times chosen (1120, 1210, 1300 UTC).....	58
4.24	Mean vertical velocity split by upward and downward motion for each of the chosen three times (1120, 1210, 1300 UTC).....	59
4.25	Frequency of hydrometeor classification for each category for each case.....	61
4.26	Surface analysis and frontal positions at 1030 UTC for 20 May case.....	62
4.27	03 UTC sounding for Lamont, Oklahoma.....	63
4.28	2 km constant altitude plot of reflectivity with overlaid wind vectors at 0931 UTC.....	64
4.29	Mean vertical velocity split by upward and downward motions over the SGP domain and between 6 and 10 UTC.....	65
4.30	Maximum and minimum wind at each height over the 6 - 10 UTC time period in the SGP region.....	66

4.31	Mean winds for four selected times (0635, 0730, 0828, 0931 UTC).	67
4.32	Mean upward and downward motions for the four selected times (0635, 0730, 0828, 0931).	68
4.33	Frequency of hydrometeor classification for each category for each case.	69
4.34	Surface analysis and frontal positions.	70
4.35	Surface analysis with overlaid radar from 2230 UTC showing surface temperature (filled), surface winds (black barbs), 500 mb winds (green barb), CAPE (color contours), dew points (dashed lines), cell tracking (orange contour). Plot courtesy of Brody Fuchs in the CSU-RADARMET research group.	71
4.36	18 UTC sounding for Lamont, Oklahoma for the 23 May case.	72
4.37	CAPPI taken at 2 km at 2230 UTC showing reflectivity with overlaying wind vectors.	73
4.38	Mean vertical velocities, also split into upward and downward motions.	74
4.39	Minimum and maximum vertical wind velocities.	75
4.40	Mean vertical velocity for four selected time steps (2134, 2209, 2237, 2336 UTC) on 23 May	76
4.41	Mean vertical velocities split into upward and downward components for the four selected times (2134, 2209, 2237, 2336).	77
4.42	Frequency of hydrometeor classification for each category for each case. At this time, the red line depicting 23 May 2011 is of interest.	78
4.43	Lightning source density from the Lightning Mapping Array in Oklahoma.	79

4.44	Surface analysis and frontal positions.....	80
4.45	12 UTC sounding for Lamont, Oklahoma.....	81
4.46	2 km cappi showing reflectivity with overlying wind vectors at 0948 UTC.....	82
4.47	Mean vertical velocities split into upward and downward motion over the entire analysis time period and domain.	83
4.48	Maximum and minimum vertical wind speeds over the entire analysis time period and domain.	84
4.49	Mean vertical velocities for 0705, 0811, 0909, and 0940 UTC.....	85
4.50	Mean vertical velocities split into upward and downward motions for 0705, 0811, 0909, and 0940 UTC.....	86
4.51	Normalized height frequency of hydrometeor category for the 25 February case. .	87
5.1	Multi-Doppler vertical wind means split into upward and downward motion for storms in which the radar topped up to at least 20 dBZ for all cases examined during MC3E.	90
5.2	Frequency of classification for each hydrometeor category for each case examined during MC3E.	92

CHAPTER 1

INTRODUCTION

Convective clouds and storms are often difficult to model, yet they are an important part of the climate system. They heat the atmosphere through diabatic processes, can suppress future cloud formation or even aid in the creation of new clouds and storms, and they provide a sink for water vapor in the atmosphere through precipitation. The coarse resolutions of climate and most cloud models are unable to adequately account for the complex cloud processes in play. At the same time, the convective parameterization schemes used in the models are computationally efficient but gloss over detailed physical processes. Further, there is still a lack of understanding of many of the processes involved in both cloud and precipitation life cycles. In order to address these issues, field campaigns provide valuable observational data, allowing for a direct comparison of model output storm characteristics. Indeed, this was a major focus of the Midlatitude Continental Convective Clouds (MC3E) campaign, which will be discussed later in this chapter. This research develops a framework for analyzing field campaign data in order to provide comprehensive comparisons with numerical models.

A goal of this project is to provide a robust observational methodology that may be applied to any season, region, or precipitation radar wavelength. The methodology created will be discussed in more detail later, but has been shown to work for many different types of convective storms, cool weather “transition” precipitation, and winter precipitation events. Five cases are analyzed and presented in this thesis. Four of these cases were obtained during MC3E, while the final case was a winter event in 2013.

1.1. IMPORTANCE OF MODEL COMPARISONS

Predictive types of models provide advanced warning of potential weather impacts, but in order to do this in the most accurate way they must accurately reflect the three-dimensional cloud structure, storm evolution (including the development of the different types of precipitation in them), and the dependence of these on the atmospheric environment. Observational analysis provides a way to look into these issues. Through the use of multiple radars of various wavelenths and scanning types, hydrometeor identification algorithms, and multi-Doppler wind syntheses, models may become more accurate in both location of storm and storm strength.

For one case analyzed during the MC3E field campaign, a statistical comparison between the Weather Research and Forecasting model coupled with Spectral-Bin Microphysics (WRF-SBM) and observations of vertical velocities and hydrometeor classifications is performed, providing valuable insight into the differences between storm simulation and observations. In many of the cases studied, a comparison with the models was not feasible due to model inaccuracy or dynamics at play, such as cold pools, that the model was unable to simulate. In these cases, the case studies are useful by themselves, as they provide a comprehensive understanding of storms in the Oklahoma region for precipitation types, development, and three dimensional wind analysis.

1.2. MC3E

MC3E was a field campaign utilizing both Department of Energy (DOE) and NASA instruments in order to study the characteristics of precipitating clouds as well as the environments in which they formed with an end goal of improving cloud convective, mesoscale, and global models (DOE goal) and Global Precipitation Measurement (GPM) algorithms (NASA goal). MC3E ran from mid April to early June 2011 centered on the DOE Southern Great Plains research facility maintained by the Atmospheric Radiation Measurement (ARM) program. The site consisted of a dense disdrometer network, rain gauges, profiling radars, and cloud and precipitation radars. Two aircraft, the NASA ER-2 and the UND Citation, were also used to study precipitation and microphysical processes within the clouds. The ER-2 contained the High-Altitude Imaging Wind and Rain Airborne Profiler (HIWRAP), allowing for radar analysis looking down at Ku/Ka frequencies, while the UND Citation contained instruments and cameras for analyzing the hydrometeor types in the clouds. The locations of the ground instruments utilized in this research are shown in Fig.1.1.

This analysis focused on the network of scanning precipitation radars, while using other instruments for comparisons and validation of the results. There were three X-band radars (referred to by their location relative the the central facility, CF, eg. XSW for the X-band radar located to the southwest of the CF). These radars were located approximately 20 to 25 km apart and are able to scan over a 40 km range. They scanned over a 6 minute period consisting of 360 degree PPIs (plan position indicator) at 22 elevations, with the lowest elevation being 0.5 degrees and the highest being 50 degrees. However, during this

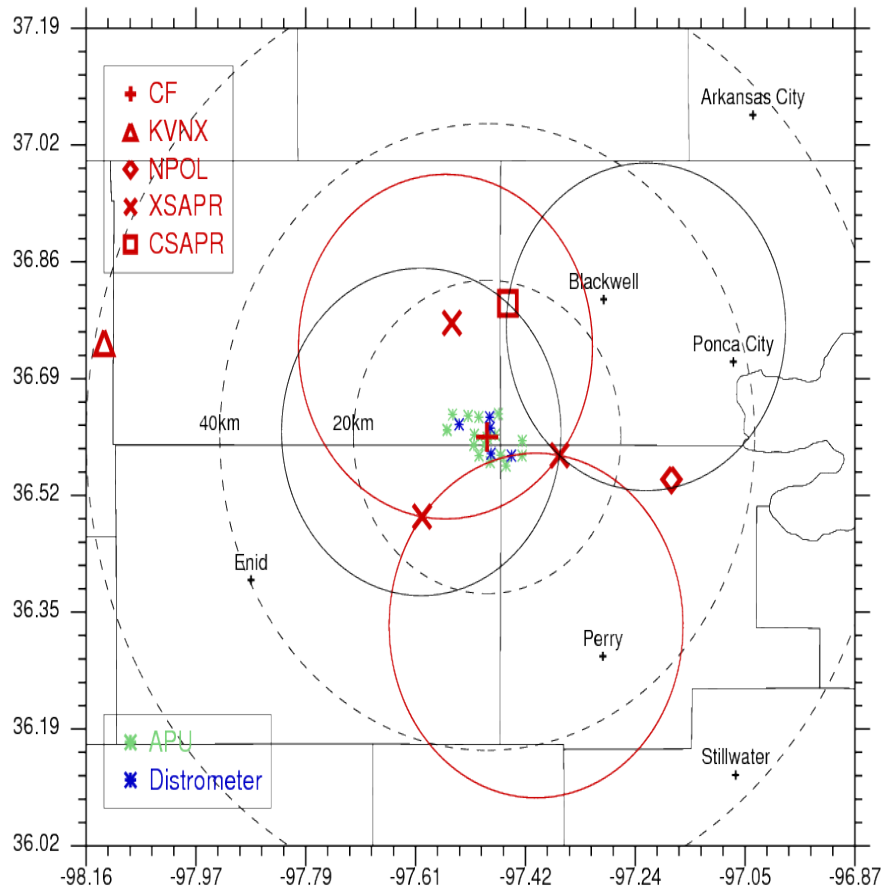


FIGURE 1.1. Map of radar, profiler, rain gauge, and disdrometer location used in this study. Dashed lines are distances in km from the ARM-SGP Central Facility, while solid black and red circles are the dual-Doppler lobes between XSE and CSAPR, and XSE and XSW radars, respectively.

campaign XNW was experiencing errors in the pointing angle and was therefore not used in this analysis.

The C-band radar (CSAPR) installed at SGP was also used in this analysis. It also scanned in 360 degree PPIs, but with 17 elevation angles, from 0.5 to 42 degrees, every 6 minutes. The S-band radar utilized was the Vance Air Force Base WSR-88D S-band radar (KVNK) as it had recently been upgraded to have polarimetric capabilities. It was located approximately 60 km from the CF, and provided long wavelength coverage. Because of

the range to storms of interest, KVNIX also routinely "topped" storms of interest, which the X-band radars were unable to do at times. Also present was the NASA S-Band Dual-Polarization Radar (NPOL). This radar was not used in analysis, as it is a mobile radar and not a permanent fixture at SGP. During MC3E it would also switch to range height indicator (RHI) scans or sector scans for coordinated flights, which made it difficult to use for statistical analysis. For this research, focus was placed on using ARM-DOE X- and C-band radars to illustrate the use of the permanent instruments at SGP. An S-Band profiler located at the CF was used to (in part) validate wind analysis. Soundings were launched from nearby Lamont, Oklahoma (KLMN) every three hours during the MC3E field campaign, and continue to be launched every 6 hours, providing good coverage of the atmospheric environment in which the storms are forming. MC3E also deployed a sounding network, providing more soundings than just at Lamont, Oklahoma. These soundings were merged into one product which was used to auto-unfold velocities using a four-dimensional doppler dealiasing (4DD) algorithm in PyArt, an open source python module for analysis of radar data (Heistermann et al., 2014), by supplying information about the advection of the storms.

1.3. ORGANIZATION

This research focuses on the case studies from the Northern Oklahoma region, both during MC3E and from a winter event. The organization of this thesis is as follows. In chapter 2, we will cover the previous work done utilizing dual-Doppler analysis as well as hydrometeor identification algorithms. We will also discuss the model used for comparison to one case. In chapter 3 we will discuss the methodology used in the analysis of the case studies. In chapter 4, each case study will be discussed in detail individually, then the storm analysis

will be compared to get a better understanding of the differences in each case. Finally, we will wrap up the research discussion with the findings and conclusions in chapter 5.

CHAPTER 2

BACKGROUND

2.1. DUAL-POLARIZED RADAR

In this study, all radars used are dual-polarized, meaning they can transmit electromagnetic waves in both the horizontal and vertical planes, as shown in Fig.2.1. In a basic sense, polarized radars provide information on the shape, phase, and orientation of precipitation particles, information that is not possible with a single polarization radar. Polarimetric variables will be discussed later in this section. Dual-polarimetric radars may also provide improved rainfall estimates, as well as a better indication of hail versus heavy rain, which would allow for more accurate flood or severe storm warnings with a larger lead time (Rinehart, 2010). Hydrometeor classifications may also be determined through the available variables, as was shown by Dolan and Rutledge (2009). Data are binned with range into so called range bins, which depend on the pulse length transmitted by a radar. For a typical one microsecond pulse, the range bin depth is 150 m.

The radar transmits electromagnetic waves into the atmosphere. When these waves encounter a hydrometeor, the hydrometeor absorbs the energy, and reradiates the wave. This return wave is then measured by the radar (Bringi and Chandrasekar, 2001). Often, these targets are moving towards or away from the radar. This causes a frequency shift between the EM waves transmitted from the radar and the EM waves reradiated back from the particle to the radar, also called the Doppler shift (Rinehart, 2010). This is related to the velocity of the particle. Velocity scans from a radar show the radial component of the particle's motion only. In order to get zonal, meridional, and vertical motions, multi-Doppler

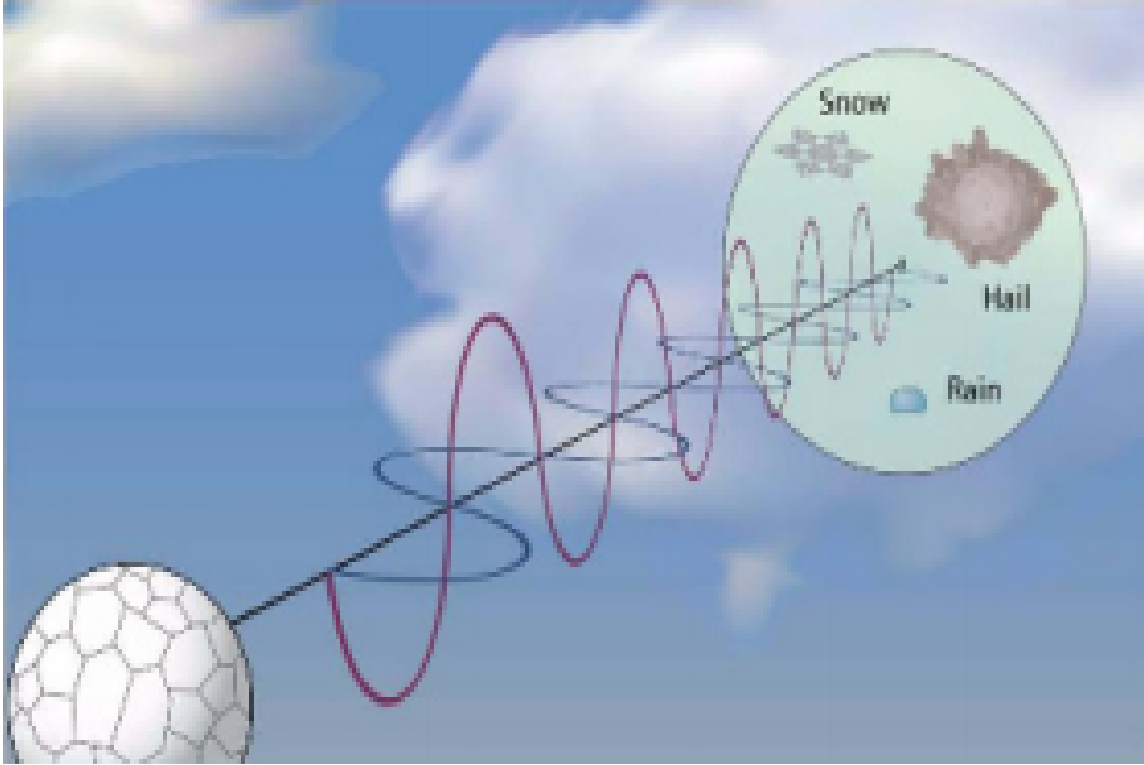


FIGURE 2.1. Dual-polarized radar transmits electromagnetic waves in the horizontal and vertical planes. Image courtesy of NOAA NSSL NOAA (2014)

analysis must be performed, which will be discussed in the following chapter. The maximum Doppler velocity is called the Nyquist velocity, and may be calculated as:

$$V_{max} = \frac{\lambda PRF}{4}$$

where λ is the wavelength of the radar used, in meters. The PRF, or Pulse Repetition Frequency, is the number of pulses emitted per second, and also affects the maximum range of the radar as $R_{max} = \frac{c}{2PRF}$, where c is the speed of light (Rinehart, 2010). Increasing the PRF will increase the maximum velocity that may be sampled unambiguously, but will decrease the maximum range invoking the possibility of second trip echoes. This is known as the Doppler Dilemma (Rinehart, 2010)), which illustrates the struggle in finding a

balance between the Nyquist velocity and maximum (unambiguous) range. When particles are moving at a speed higher than the Nyquist velocity, folding occurs. For example, if the Nyquist velocity is $\pm 15 \text{ m s}^{-1}$ and a hydrometeor is moving at a speed of 25 m s^{-1} away from the radar, the radar would loop from $+15 \text{ m s}^{-1}$ to -15 m s^{-1} and begin measuring toward 0 from there, so the radar would interpret the hydrometeor's speed as -5 m s^{-1} toward the radar. A visual example of Nyquist folding is shown in Fig.2.2. Areas where there is an abrupt transition from red to purple colors, or vice versa, are regions where folding has occurred. This must be corrected prior to analysis. Methods for correcting used in this research will be discussed in the next chapter.

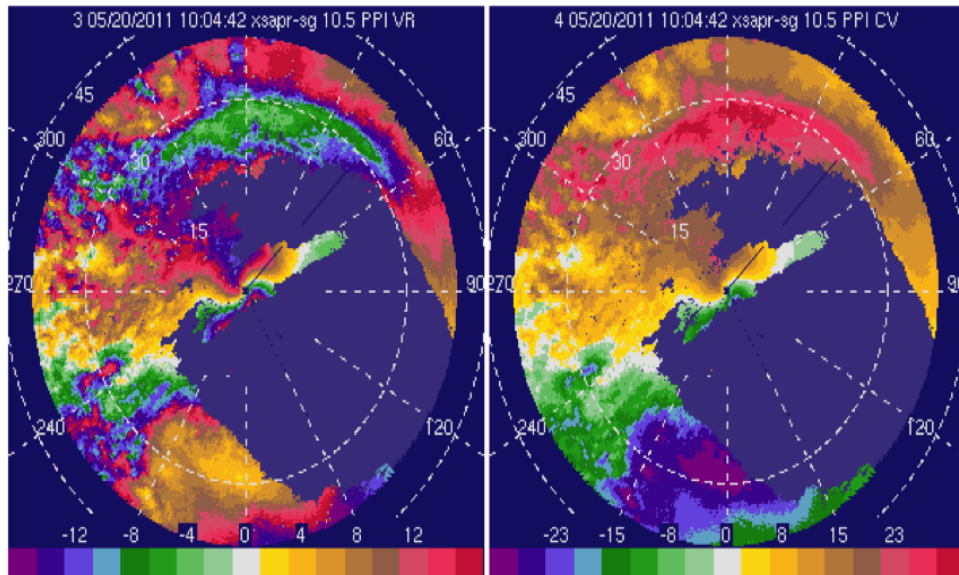


FIGURE 2.2. Example of velocity folding. Raw velocity is shown on the left, with a Nyquist velocity of 16.8 m s^{-1} . Corrected velocity is shown on the right with no folding.

One of the main variables examined using a radar is the reflectivity. This is a measurement of the returned energy, following scatter of the transmit wave from a collection of scatterers. Radar reflectivity depends on particle diameter and particle concentration. For

example, hail is very large so it would reflect a large amount of energy back to the radar and return a high value of reflectivity. An area of heavy rainfall would contain many drops and would also have a high reflectivity.

The reflectivity at the horizontal polarization (Z_h) may be calculated as follows (Bringi and Chandrasekar, 2001):

$$Z_h = \frac{\lambda^4}{\pi^5 |K_p|^2} \int_D |S_{hh}(r, D)|^2 N(D) dD$$

where λ is the wavelength of the radar, K_p is the dielectric coefficient, S_{hh} is the horizontal element of the scattering matrix for both transmitted and backscattered waves, D is the drop size diameter, r is the axis ratio of the hydrometeor, and $N(D)$ is the drop size distribution over the range bin sampled, but is often assumed to be the Marshall-Palmer size distribution (Marshall and Palmer, 1948). Vertical bars denote the magnitude of the element they surround. A similar calculation may be done to retrieve the vertically polarized reflectivity. For Rayleigh backscatter, S_{hh} increases as nearly D^6 , so that we may say (Bringi and Chandrasekar, 2001)

$$|S_{hh}|^2 \approx D^6$$

This shows that reflectivity may be approximated to be a function of the sixth moment of the drop size distribution (Bringi and Chandrasekar, 2001).

Differential reflectivity, or Z_{dr} , is the ratio of the horizontal returned power to the vertical returned power, and is a function of drop shape, phase (water vs. ice), and size (Bringi and Chandrasekar, 2001). It may be calculated as:

$$Z_{dr} = \frac{\int |S_{hh}(r, D)|^2 N(D) dD}{\int |S_{vv}(r, D)|^2 N(D) dD}$$

where S_{vv} is the vertical element of the scattering matrix for both transmitted and backscatter waves. This variable is ideal for determining the shape of the drop. A more spherical hydrometeor, such as hail or small rain drops, will have a near zero Z_{dr} value. As drops grow, they are more properly viewed as oblate spheroids, thereby increasing Z_{dr} , as shown in Fig.2.3. Herzegh and Jameson (1992) showed how Z_{dr} changes with a change in axis ratio (A/B where A and B are the semi-minor and semi-major axes), and found that more oblate shapes (A is greater than B) had a higher Z_{dr} , as shown in Fig.2.4.

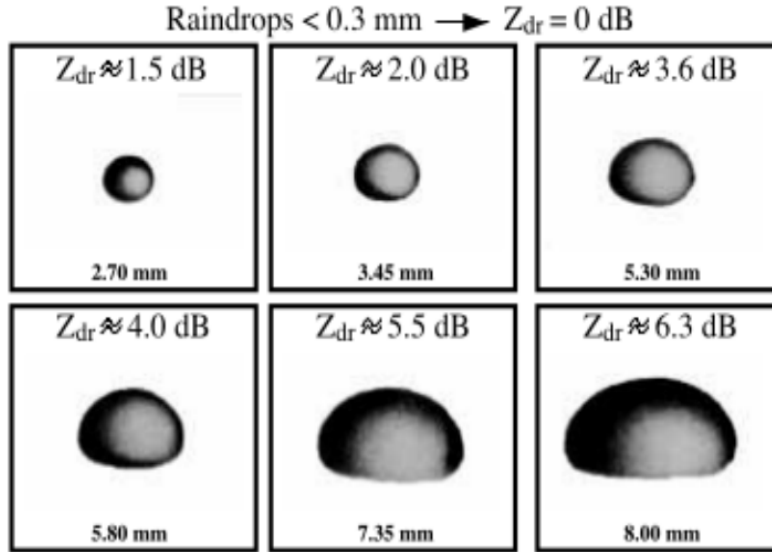


FIGURE 2.3. Z_{dr} as drop shape becomes more oblate. Image from Polarimetric Weather Radar (Bringi and Chandrasekar, 2001)

The measure of the cumulative phase change as the pulse propagates through the atmosphere is called Φ_{dp} , or the propagation differential phase (Bringi and Chandrasekar, 2001). This parameter is unique because it is independent of power and immune to attenuation.

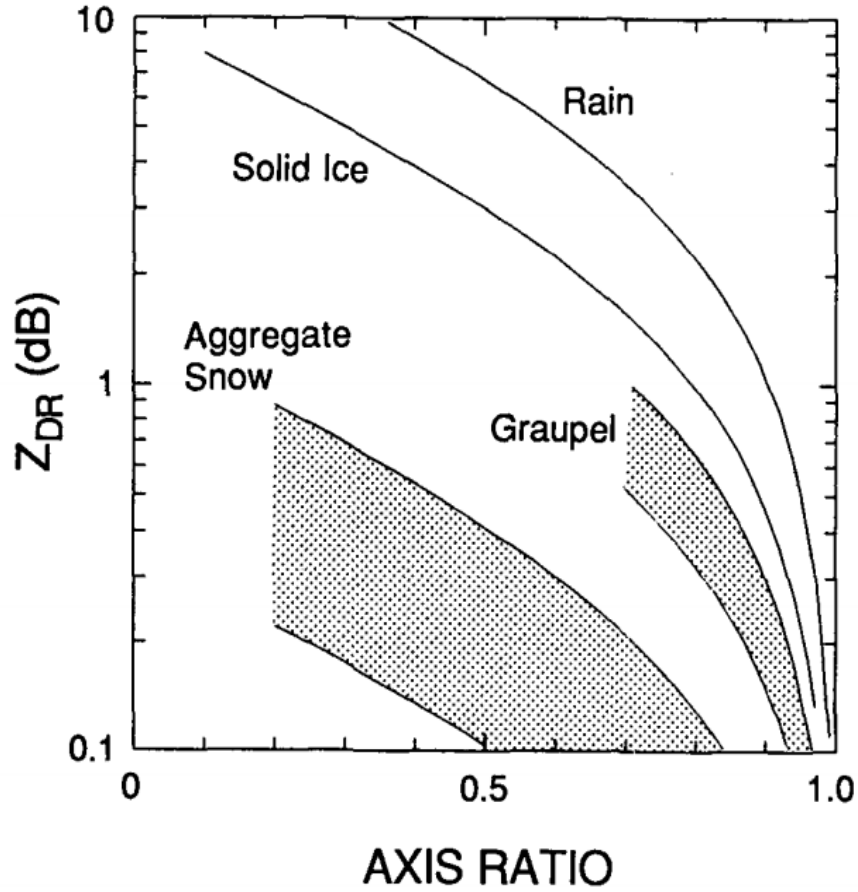


FIGURE 2.4. Z_{dr} as the axis ratio ($fracAB$) changes for different types of hydrometeor (Herzogh and Jameson, 1992)

In a medium of oblate raindrops, when horizontally and vertically polarized waves move through this medium there is more dielectric material in the horizontal than the vertical, so the horizontal wave's phase (Φ_h) will change more over a given distance than the vertical wave's phase (Φ_v). Therefore, the differential phase may be calculated at each range bin as (Rinehart, 2010):

$$\Phi_{dp} = \Phi_h - \Phi_v$$

The phase change will be larger in areas of heavy precipitation, and also depends heavily on the path length of the pulse. In non-Rayleigh scattering regimes, phase fluctuations may be caused by the phase shift from backscattered EM waves (δ), which can be found from the difference between the total phase and the propagation differential phase.

K_{dp} , or specific differential phase, is the range derivative of Φ_{dp} . It may be calculated from Hubbert and Bringi (1995) in terms of degrees of phase shift per kilometer along the radial as:

$$K_{dp} = \frac{\Phi_{dp}(r_2) - \Phi_{dp}(r_1)}{2(r_2 - r_1)}$$

where r is the range in km along the radial, while the 2 in the denominator accounts for the trip out to the range interval in question and back to the radar by the pulse. A target with a near zero K_{dp} will be randomly oriented or almost spherical in shape. A positive value indicates that the target is larger in the horizontal than in the vertical, such as raindrops, while a negative value means the targets are larger in the vertical than the horizontal, such as some forms of graupel and vertically aligned ice (Rinehart, 2010).

The co-polar correlation coefficient, or ρ_{hv} , is the correlation between the horizontally and vertically polarized pulses at the same location and time (Rinehart, 2010) and may be calculated as:

$$|\rho_{hv}| = \frac{\langle nS_{vv}S_{hh} \rangle}{(\langle n|S_{hh}|^2 \rangle \langle n|S_{vv}|^2 \rangle)^{\frac{1}{2}}}$$

as shown by Bringi and Chandrasekar (2001; Eq. 7.41a). This variable can provide information about the shape of drops, degree of melting, and the mixture of particles within

a volume. Rain would have a value of approximately 1, whereas hail, snow, graupel, and ice crystals would have smaller values (slightly less than one) due to their irregular shapes, random orientations, and mixes of water and ice. ρ_{hv} can also be affected by noise, which causes a decrease in the correlation, meaning that as the signal-to-noise ratio gets small, ρ_{hv} decreases. For mixtures of ice and water, values of ρ_{hv} can be considerably smaller than 0.9.

By utilizing each of the polarimetric radar variables, a hydrometeor classification algorithm may be created, as was done by many studies, such as Liu and Chandrasekar (2000), Baldini et al. (2005), Dolan and Rutledge (2009) (henceforth D09), and Dolan et al. (2013) (henceforth D13). D09 and D13 used simulations from a T-matrix scattering model of different types of hydrometeors to create one-dimensional fuzzy logic membership beta functions, which can then be applied to radar data to arrive at a hydrometeor classification for a given range bin or grid block. The hydrometeor classification scheme used in this research was based on D09 and D13, and will be discussed in more detail in the following chapter.

2.2. MULTI-DOPPLER ANALYSIS PREVIOUS WORK

There have been a multitude of previous studies using dual- or multi-Doppler methods in various applications as well as integrating these winds with a hydrometeor classification to examine the inner workings of the clouds and storms.

One study by Ray et al. (1980) used single and multi-Doppler radar observations to examine a tornadic storm on 20 May 1977 in central Oklahoma. Previously, focus had been on single-Doppler methods to determine three dimensional storm motions through implied areas of convergence and divergence. This study compared the different methods and found that with more information (i.e. more radars available), the wind analysis had a smaller

error, but found that there was little difference between the two radar analysis and the four radar analysis in terms of estimated error. They also found that there should be no more than a few minutes between scans in order to minimize storm motion or evolution effects, and that the radar scans in convective cases should include elevation angles greater than 30 degrees so that particle fall speed may be approximately estimated (Ray et al., 1980).

On 19 May 1977, a squall line formed in Oklahoma. Kessinger et al. (1987) studied the convective and stratiform structure of this system using multiple Doppler analysis using the NSSL 1977 Spring Program radars (S-bands Norman, Cimaron, and CHILL, and C-band NCAR CP-4). Kessinger found that in general, flow parallel to the squall line was stronger than the perpendicular flow. Kessinger et al. (1987) also found that the updrafts tilted toward the west at low levels and toward the east at upper levels in the mature convective region.

In 1991, a study was completed on a squall line in Southern Germany by Meischner et al.(1991). This study used single-Doppler analysis to arrive at zonal and meridional flow patterns as well as determining hail sizes and distinguishing regions of rain from regions of rain-hail mixtures. Their findings revealed that so-called big drops existed in the feeder clouds of the squall line and played an important role in the hail formation process (Meischner et al., 1991).

More recently, a study was done by Dolan and Rutledge (2010) that used the CASA IP1 network of four X-band radars in central Oklahoma to examine kinematic and microphysical interactions in the 10 June 2007 convective storms. They used the D09 hydrometeor classification algorithm to arrive at the microphysical composition of the storms, and the

NCAR-CEDRIC package to perform multi-Doppler analysis to arrive at the kinematics. It was found that the updraft development lead to graupel formation, which was followed by intra-cloud lightning, with cloud to ground lightning beginning once high density graupel was found at mid-levels. As more graupel was suspended in the updraft, a downdraft begins forming, bringing precipitation to the surface, causing CG flashes to decrease.

Collis et al. (2013) examined the statistics of storm updraft velocities in Darwin, Australia during the Tropical Warm Pool International Cloud Experiment (TWP-ICE) using dual-Doppler analysis, which was also compared to the vertical velocities observed by a nearby profiler. They found that the profiler is unable to fully capture the three dimensional storm structure as it is a point-time measurement.

In examining the vertical velocity profile, they found the mean height of the maximum updraft to occur at approximately 6 to 8 km above ground, as shown in Fig.2.5, which is lower than was found in a previous modeling study by Wu et al. (2009), who found this occurred at a height of 12 km in the WRF model they ran.

A study by Fujiyoshi et al. (1998) examined longitudinal snowbands containing convective cloud systems near Ishikari Bay, Hokkaido Japan on 15 January 1992 using two X-band radars to provide dual-Doppler kinematics. In general, they studied the horizontal wind component as their snow bands did not have strong vertical motions. They did find, however, that the updrafts were found to the front of the systems, and were responsible for transporting ice and snow toward the rear of the bands, where it evaporated outside the clouds causing a downdraft.

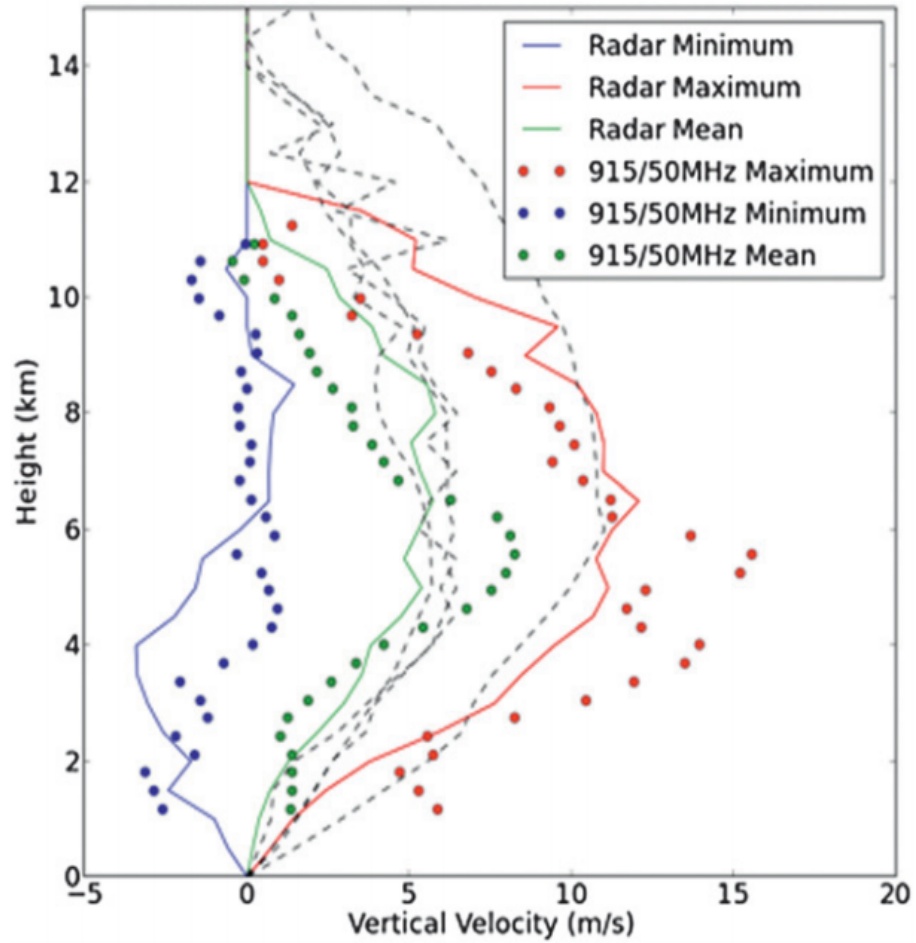


FIGURE 2.5. This figure shows the vertical velocities from the dual-Doppler (lines) and profiler (dots). Blue is the minimum vertical velocity, red is the maximum, and green is the mean. The height of the maximum updraft and the maximum of the mean updraft occurs at a height of approximately 6 km for this case. Collis et al. (2013)

CHAPTER 3

METHODOLOGY

This section discusses what was done to quality control the radar data, such as correcting for biases and attenuation. We also present the methodology for analyzing the data.

3.1. QUALITY CONTROL

The first step in analyzing data is to ensure the data set is of high quality. For many of the cases analyzed during MC3E, the storms rained heavily on the radomes of the CSAPR and the two XSAPRS, causing a significant drop in reflectivity with range, such as that shown in figure 3.1; this is termed radome attenuation. This made these times unusable for kinematic and microphysical analysis. If the scans suffering from this were only a small portion of the ideal time period, they were removed from analysis. If the radar was contaminated by radome attenuation for a longer portion of the ideal time frame, the analysis time period was cut short. This was done for the 20 May 2011 case, as a strong squall line moved over the radars and we were unable to get data from the strongest portion of the storm or during the period of the trailing stratiform region.

All four of the radars used suffered from reflectivity and differential reflectivity biases. The differential reflectivity biases were calculated using vertically pointing scans when available, horizon-to-horizon RHI scans (Ryzhkov et al., 2005)), or from a high elevation angle scan through stratiform rain when neither of the other types of scans listed were available. In these chosen scan types and regions of precipitation, it is assumed that the radars should see a Z_{dr} of 0 dB. Histograms were created in these regions using the NCAR SOLOii editing

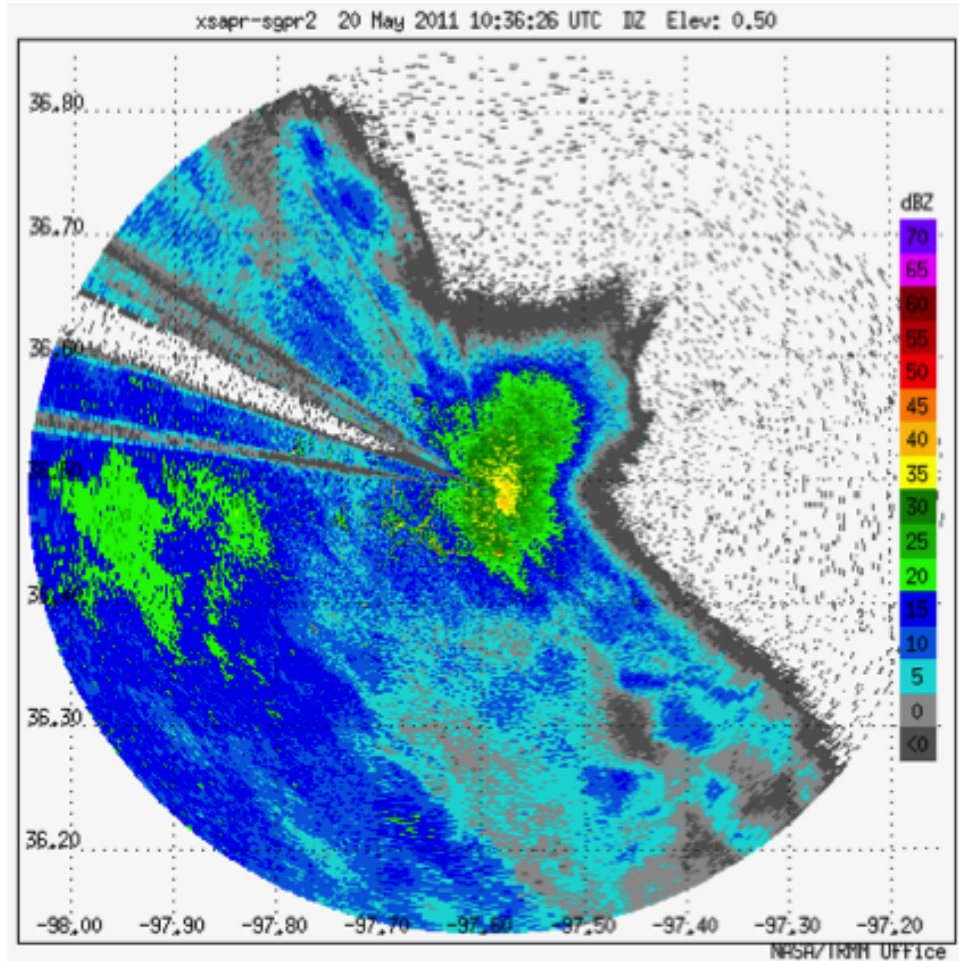


FIGURE 3.1. Example of radome attenuation. To the Northeast of the radar, the reflectivity drops quickly with range.

package and the mean of the histogram was used as the Z_{dr} bias. Once the Z_{dr} bias had been accounted for, the reflectivity bias could be found and corrected. This was done using self-consistency techniques (Gorgucci et al., 2006) with relations derived from 2-D video disdrometer scattering simulations. This method utilizes a calculated K_{dp} and a corrected differential reflectivity in areas with no non-meteorological echos. Self-consistency assumes a relationship between K_{dp} , Z_{dr} , and Z_h as in equation 12 from Ryzhkov et al. (2005):

$$Z = a + b * \log(K_{dp}) + c * Z_{dr}$$

Here the coefficients a, b, and c are determined for each radar wavelength from 2DVD scattering simulations. The reflectivity offset is then determined by incrementally adjusting Z from Z_{min} to Z_{max} to match the following integrals (equations 14 and 15 from Ryzhkov et al. (2005)):

$$I_1 = \int_{Z_{min}}^{Z_{max}} \langle K_{dp}(Z) \rangle n(Z) dz$$

$$I_2 = \int_{Z_{min}}^{Z_{max}} 10^{-\frac{a}{b} + \frac{Z}{b} - \frac{c \langle Z_{dr}(Z) \rangle}{b}} n(Z) dz$$

where $n(Z)$ is defined as the number of data pixels, or gates, for a given 1 dB interval of reflectivity between the limits of the integral. When the integrals match, this Z_h is the correct value, and the difference between this and the original is the offset.

The Z and Z_{dr} biases are listed in Table 3.1. The Southwest XSAPR (XSW) had the largest Z_{dr} bias, of approximately -3.6 dB for most of the cases. Overall we found KVNK to have consistent biases over each case in both reflectivity and Z_{dr} , while CSAPR was consistent for reflectivity only and varied for Z_{dr} for upwards of 1 dB for each case. The XSAPRs varied widely in reflectivity biases but were relatively consistent for differential reflectivity biases. After these corrections, the data is assumed to be calibrated to within 0.2 dB for Z_{dr} and 1 dB for reflectivity.

Another problem was a large decreasing trend in differential phase over a short range. This caused issues when calculating specific differential phase (K_{dp}). During calculations, delta effects due to Mie scattering, meaning that the backscatter differential phase gets noisy in Mie scattering regimes, making it difficult to remove from Φ_{dp} calculations and therefore

TABLE 3.1. Reflectivity and differential reflectivity biases for each radar used for each case analyzed.

Radar	20110425		20110501		20110520		20110523		20130225	
	Z_h (dBZ)	Z_{dr} (dB)	Z_h	Z_{dr}	Z_h	Z_{dr}	Z_h	Z_{dr}	Z_h	Z_{dr}
XSW	-9.0	-3.6	-3.27	-3.9	-3.27	-3.9	-7.1	3.4	-10.8	-3.9
XSE	-10.5	0.32	-6.7	0.3	-8.95	0.15	-9.1	0.5	N/A	N/A
CSAPR	0.0	1.6	0.0	1.6	0.0	0.0	0.0	0.25	0.0	2.1
KVNX	3.0	0.25	3.0	0.25	3.0	0.25	3.0	0.25	3.0	0.25

caused positive and negative variations in K_{dp} with range. Methodology from Wang and Chandrasekar (2009) was chosen to calculate K_{dp} , as it produced the smoothest results with fewer range oscillations noted.

The XSAPRs and CSAPR were also corrected for both attenuation and differential attenuation, using methods from Lim and Chandrasekar (2006), where $\alpha_h = 0.28$ at X-band and $\alpha_h = 0.113$ for C-band, and α_h is defined as the specific attenuation at the horizontal polarization and may be calculated as:

$$\alpha_h(r) = a[Z_h(r)]^b[Z_{dr}(r)]^c$$

where the coefficients b and c are dependent on the drop size distribution, while a is dependent on temperature. The values used in this research were obtained using the Beard and Chuang (1987) model for raindrop size at -10°C .

Differential attenuation values (α_{dp}) are the difference between the horizontal polarization attenuation and the vertical polarization attenuation. Attenuation correction was found to work well at both X- and C- band, while differential attenuation correction was found to be insufficiently corrected in some cases, especially at C-band. Therefore, the CSAPR data was additionally thresholded on $Z_{dr} < -2\text{dB}$.

Finally, non-meteorological echo was removed using thresholds on the correlation coefficient (< 0.7 for heights < 2.5 km), signal quality (SQ, < 0.5), and the standard deviation of the differential phase. An example of a non-meteorological echo is shown in figure 3.2, depicting second trip echoes within the yellow circle.

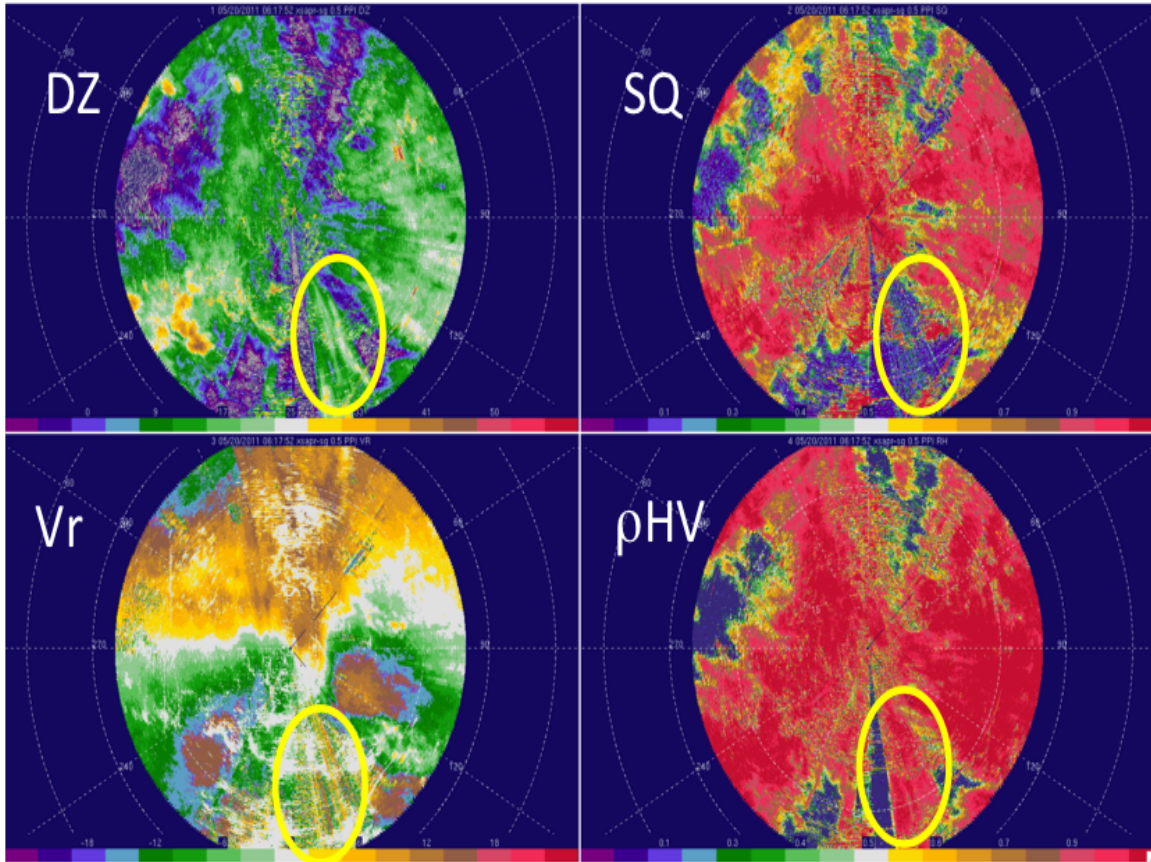


FIGURE 3.2. Non-Meteorological Echo (yellow circle). This echo has no velocity pattern, no signal quality value, but shows up on reflectivity scans.

3.2. VELOCITY CORRECTIONS

For all of the MC3E cases, the velocity scans were folded due to the Nyquist velocities of the radars, listed in Table 3.2. This was done primarily by hand using SOLOii. This method was done for both XSAPRs for all cases, as well as KVNx for the 25 April and 23 May cases. For CSAPR and the remaining cases for KVNx, velocities were unfolded

using a four-dimensional dealiasing (4DD) algorithm (James and Houze Jr, 2001) in Py-ART (Heistermann et al., 2014) This method was found to be reasonably accurate, but not without error. Scans were spot checked using SOLOii to unfold any areas that were missed by the algorithm. While hand-unfolding still had to be completed on poorly unfolded regions, the 4DD algorithm was found to save a significant amount of time and was therefore used on the remaining KVNx cases, as well as CSAPR for all cases. In order to minimize spot-correction, non-meteorological echo and noise were removed prior to running the algorithm, as this created fewer areas of bad unfolding on storm edges or in areas with non-meteorological echoes. For the winter case examined, no unfolding was necessary at any of the available radar wavelenths.

TABLE 3.2. Characteristics of the scanning radars surrounding the SGP Central Facility used in this research.

Radar	Wavelength (cm)	Volume Update Time (min)	Nyquist Velocity (ms^{-1})	Maximum Range
XSW	3.2	6	17.2	40
XSE	3.2	6	16.8	40
CSAPR	5.5	6	16.52	120
KVNx	11	4.5	26.75	>150

3.3. CONVECTIVE-STRATIFORM PARTITIONING

A convective - stratiform partitioning based on Steiner et al. (1995) was applied to both the radar observations as well as any simulated cloud model data. Steiner et al. (1995) uses three criteria to distinguish a convective area. The first selection is based on intensity. If a grid point has 40+ dBZ then it is convective. Next is the peakedness of the remaining points. If the reflectivity at a particular point is significantly greater than the average background reflectivity, even if that point is not 40+ dBZ, then it is considered convective. Finally, for

each convective gridpoint identified by one of the previous categories, all gridpoints surrounding the convective gridpoint are categorized as convective if they fall within a reflectivity dependent radius that increases stepwise with increasing background reflectivity.

3.4. GRIDDING

All of the radars were gridded to a cartesian grid centered on the Central Facility (CF) of the SGP using the NCAR REORDER package. The horizontal and vertical grid spacing was 1 km, with the lowest grid level in the vertical being 1 km MSL. The domain size was 120 km in the horizontal for the wind retrievals and 200 km in the horizontal for the microphysical retrievals. The vertical grid spacing was 18 km in the vertical. This enabled the data to be more readily compared between radars. The grid spacing of 1 km was chosen because it created the best vertical resolution in the XSAPR data, as they reach the highest elevation angles and these elevation angles are more spread apart as they reach upper levels.

3.5. MULTI-DOPPLER

Using the gridded data, velocity data was input into the NCAR CEDRIC package (Mohr and Miller, 1983)) from all available radars within 3 minutes of each synthesis time. In most cases, all four radars were available. When they were not, a synthesis of 3 radars was used. This provided an over-determined dual-Doppler with the addition of one or two radars depending on scan times and availability. This provides the best ability to correctly assess the upper boundary conditions and lower boundary conditions, as well as maximizes coverage area and minimizing error. In this method, all radars present are used to arrive at multiple Doppler winds in as much area as possible, often analyzing over an area multiple times with

different radars (Ray and Sangren, 1983)). A dual-Doppler analysis consisting of just two radars was not used in this research. The volumes of each radar were advected to a common time using the 700 mb wind direction and speed from the Lamont, OK (LMN) sounding at the closest available time. Due to the scanning strategy of the DOE radars, the synthese times are approximately 6 minutes apart. In order to account for the precipitation fall speed contribution to the resulting wind field, a fall speed (V_t) - reflectivity (Z_h) relationship based on Giangrande et al. (2013) was used. Hydrometeor-specific V_t - Z relationships were determined by a simple hydrometeor classification between dry snow, graupel and hail, rain, and wet snow (using the HID described in section 3.7), with no correction applied for the wet snow category. The returned fall speed from the following equations is in ms^{-1} .

$$\begin{aligned}
 (1) \quad & V_t = 3.15 * Z_h^{0.098} && \textit{Rain} \\
 (2) \quad & V_t = 2.2 + \sqrt{Z_h} && \textit{Graupel/Hail} \\
 (3) \quad & V_t = 1.0 && \textit{Dry snow}
 \end{aligned}$$

The calculated fall speeds at each radar grid point were then read into CEDRIC, where the maximum fall speed at each point from the available radars was calculated. This maximum value was then used to remove fall speed from the radial velocity before the 3D wind field was calculated from MASS2. Vertical wind speeds were then calculated from the convergence calculated using the zonal and meridional flow output by MASS2 using the variational integration technique (INTEGR) (O'Brien, 1970; Dolan and Rutledge, 2010).

The estimated error in the wind retrievals used by this method is 1 ms^{-1} (Nelson and Brown, 1987; Dolan and Rutledge, 2010). One source of error could be that the radars are not sufficiently 'topping' the storm to close the upper boundary condition. By adding the S-band KVN_X radar, our analysis appears to largely avoid this source of error. Gridding errors, sampling the lower boundary condition, and advection corrections could also contribute to the 1 ms^{-1} estimated error. Additional errors are introduced by the assumed fall speed relations, particularly in the graupel and hail regions, which had a large spread in the empirical data shown in Giangrande et al. (2013).

3.6. S-BAND PROFILING RADAR

The S-band vertically pointing profiler, located at the CF, provides measurements of total vertical motion (combined fall speed and air motions) every minute from 200 m near the surface to a height of 16 km. This made it ideal for comparisons with the multi-Doppler radar analysis. First, however, the data had to be interpolated to the radar volume times of approximately 6 minute intervals and 1 km vertical resolution. The fall speed maximum derived from the scanning radars and output by CEDRIC was removed at each grid point, so that comparisons may now be done between the vertical velocities of the multi-Doppler synthesis and the profiling radar.

3.7. MICROPHYSICAL CATEGORIZATION

The multi-wavelength hydrometeor identification algorithm (MWHID) used is a derivative of the D09 and D13 methodology discussed previously. This algorithm uses the best aspects of each radar wavelength to determine the hydrometeor type at a given grid point.

For instance, X-band is best in regions of small ice crystals (Thompson et al., 2014), but is not good at detecting hail and graupel due to Mie scattering effects and attenuation. C-band radars would be good at identifying melting hail due to resonance effects resulting in large Z_{dr} values. S-band is good at identifying hail because the dominance of the Rayleigh regime leads to increasing reflectivity as hail size increases. Each of these benefits and complications were taken into account and each radar wavelength 'weighted' by ability to identify each hydrometeor type. The algorithm consists of ten categories: drizzle (DZ), rain (RN), hail (HA), big drops/melting hail (BD), low density graupel (LDG), high density graupel (HDG), aggregates (AG), wet snow (WS), ice crystals (CR), vertically aligned ice crystals (VI), and unknown (UNK), where the unknown category means the multi-wavelength HID failed to identify a hydrometeor agreed on by the most radars, such as when all radar hydrometeor identifications thought the particle type was something different. Big drops are drops with a diameter greater than 5 mm, and may indicate the presence of melting hail. The multi-wavelength HID methodology is outlined in figure 3.3, which also shows an example of big drops. In the black circle, KVNIX classified this area as big drops. Since this wavelength of radar is trusted for big drop identification, it gets weighted by 8 and therefore the HID array contains BD 8 times. CSAPR identifies this as hail, but due to effects from Mie scattering, this is not as trusted and is only added one time to the array. The XSAPR combined product identified high density graupel in this region, which is not trusted significantly at X-band, and therefore it was added two times. The mode of this array is then taken, and the multi-wavelength hydrometeor identification classifies this area within the black circle as big drops.

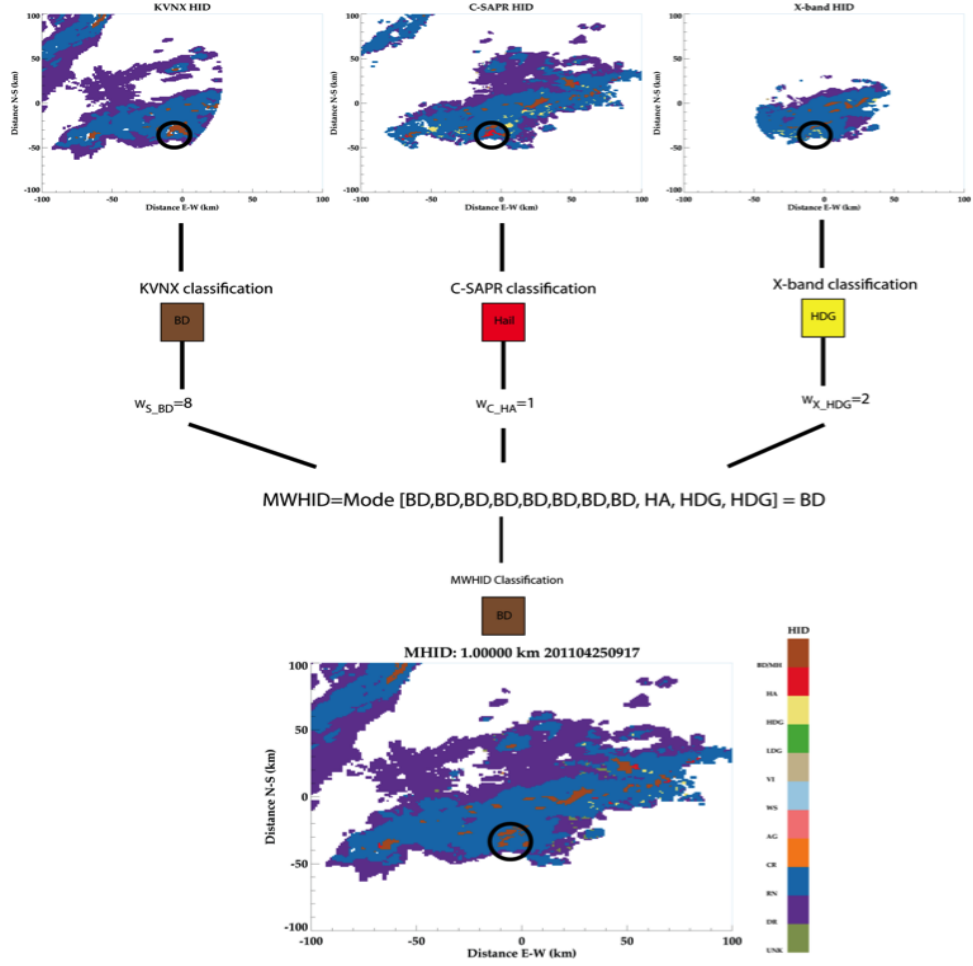


FIGURE 3.3. Example of the weighting scheme for the multi-wavelength hydrometeor identification algorithm used in this study.

3.8. MODEL

For one case, a comparison is done using the Weather Research Forecasting model with Spectral-bin Microphysics, or WRF-SBM. This model was developed and run by NASA Goddard Space Flight Center (GSFC) (Iguchi et al., 2012a,b) to resolve complex microphysical phenomena in many environments. The SBM is part of the Hebrew University Cloud Model (Khain and Sednev, 1995; Khain et al., 2011). Within clouds, hydrometeors are classified as water drops, ice crystals, aggregates, graupel, and hail. Particle size distributions are calculated over 43 mass bins ranging in size from nucleation particles to hail stones.

Melting fractions are also calculated for the large ice categories, while riming is included for aggregates. In order to compare the model simulation to the radar observations, the WRF-SBM must be classified into similar hydrometeor categories. The 43 bins over 7 species are subdivided into HID categories according to assumptions on phase, size, and density of each particle, as shown in figure 3.4. These are reflectivity weighted, and will only be classified for echoes with reflectivities higher than 0 dBZ. S-band reflectivity was simulated through the simulator G-SDSU (Goddard Satellite Data Simulator Unit) (Matsui et al., 2014), which simulates radar reflectivity by accounting for bin by bin microphysics for each hydrometeor category, simulated over a column at S-band.

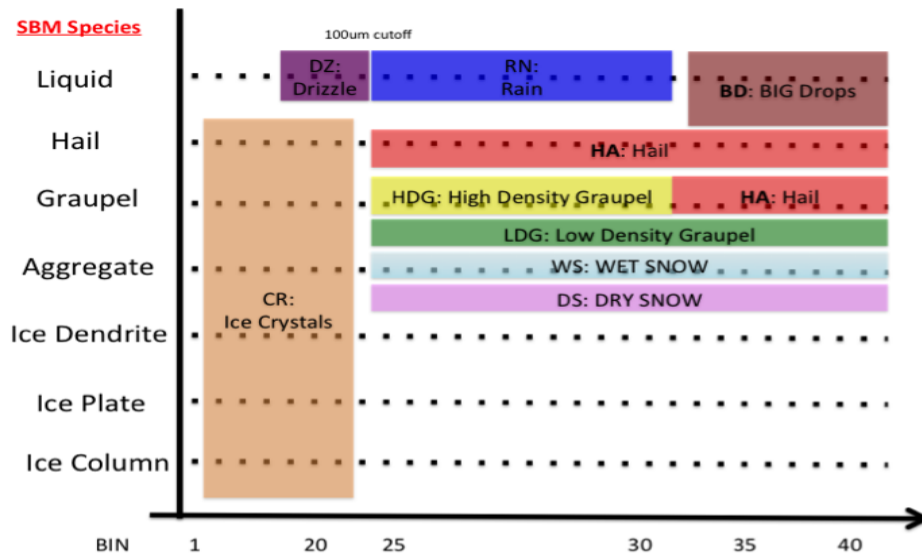


FIGURE 3.4. Hydrometeor Classification for the WRF-SBM over the 43 mass bins and 7 species.

CHAPTER 4

DISCUSSION

In this chapter, we will discuss the findings from five analyzed cases. For the first case, 25 April 2011, a validation of the multi-Doppler vertical winds will be done using the profiler to show accuracy of the vertical motions found using the scanning radars. This was done for only this one case as the storms did not hit the profiling radar on any of the other cases examined. A comparison to the WRF-SBM will also be done for this case. Throughout each case, the same methodology will be used to analyze the kinematics and microphysics of the storm.

4.1. CASE ANALYSIS

4.1.1. 25 APRIL 2011. On this day, soundings throughout the early hours UTC showed little sign of instability, with no convective available potential energy (CAPE) and a large inversion, though it was quite saturated and had a low lifted condensation level (LCL) around 922 mb (or 500 m above ground), as shown in the 9 UTC sounding in figure 4.1. A value we can calculate from the sounding is the warm cloud depth, which is calculated as the distance between the LCL and the height of the 0° C isotherm. For this case, the warm cloud depth was relatively thick at 3.1 km due to the low LCL.

The surface map (figure 4.2) on this day showed a stationary front located to the southeast of the SGP site at 9 UTC, turning into a warm front at 12 UTC and pushing into the SGP region, weakly forcing organized elevated convection.

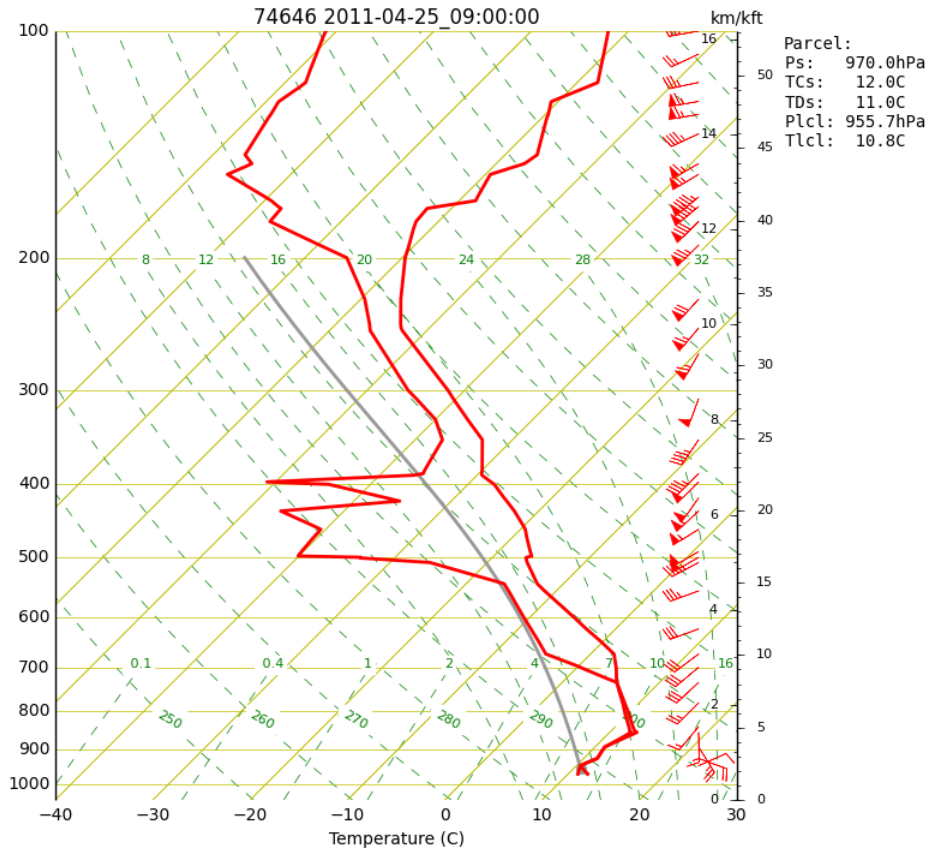


FIGURE 4.1. Skew-T showing surface lifted parcel (grey) at 9 UTC from LMN.

In figure 4.3, the atmospheric conditions at the time of storm development can be seen at 09 UTC. Surface based CAPE is very low, as no contours appear on the plot. However, when looking at the CAPE calculated from the most unstable air parcel, it reaches values of approximately 1000 Jkg^{-1} . There is a good amount of shear between the surface and 500 mb levels. Surface temperatures are fairly cool, around 18 to 21 °C with dew points of approximately 13 °C so the air was quite moist as is supported by the sounding previously discussed.

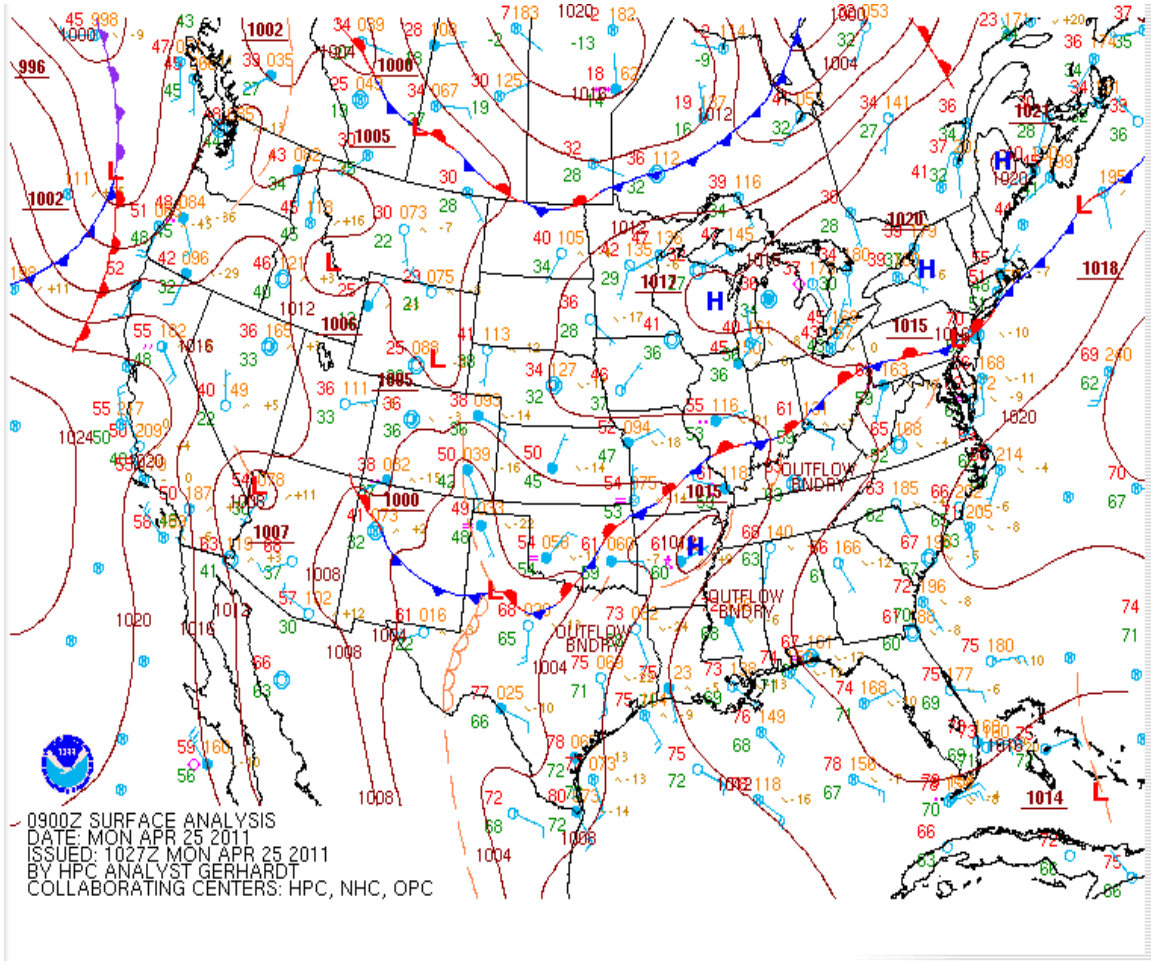


FIGURE 4.2. Surface analysis for 9 UTC.

An east-west oriented convective line developed (as shown at the 09 UTC hour in figure 4.3) in the early hours and propagated over the SGP instruments. This is classified as elevated convection, as it occurred during the early morning hours and had no surface convergence feature (Wilson and Roberts, 2006). Data on this day were obtained from the CSAPR, XSE, XSW, and KVNK radars for further analysis. The time period chosen for analysis was 08-1130 UTC as this time period had the most operational instruments with the least amount of radome attenuation. The XSW radar did exhibit some radome attenuation at 10 UTC, so at that time only a three radar multi-Doppler analysis was done.

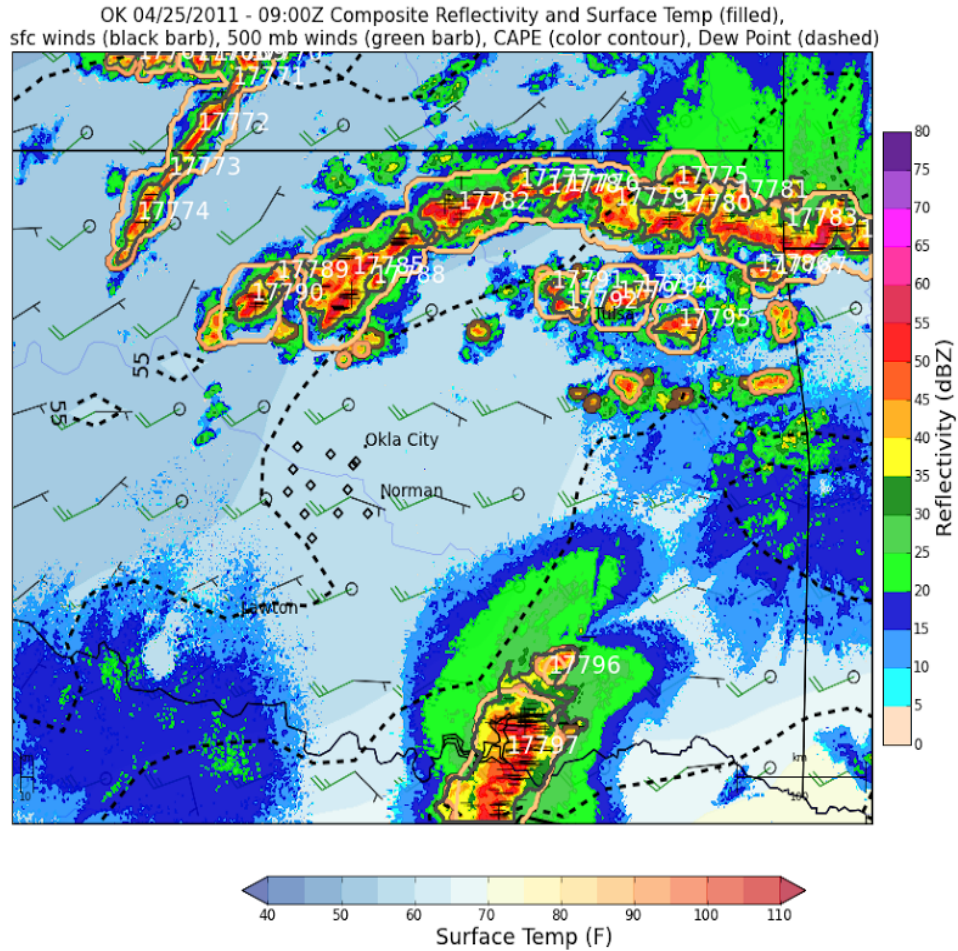


FIGURE 4.3. Surface analysis with overlaid radar from 09 UTC showing surface temperature (filled), surface winds (black barbs), 500 mb winds (green barb), CAPE (color contours), dew points (dashed lines), cell tracking (orange contour). Plot courtesy of Brody Fuchs in the CSU-RADARMET research group.

Through the course of the time period chosen for analysis, storms moved from southwest to northeast across the SGP site. The majority of the stronger storms missed the CF, including the S-band profiler, as shown in the swaths in figure 4.4, where the swath is the the maximum reflectivity at each grid point and at each time taken over the SGP domain.

4.1.1.1. *Comparison of Dual-Doppler Vertical Winds.* For this case, zonal, meridional, and vertical winds were derived from three or four radar multi-Doppler analysis. The three radar multi-Doppler analysis was used in time periods where there was not a scan within

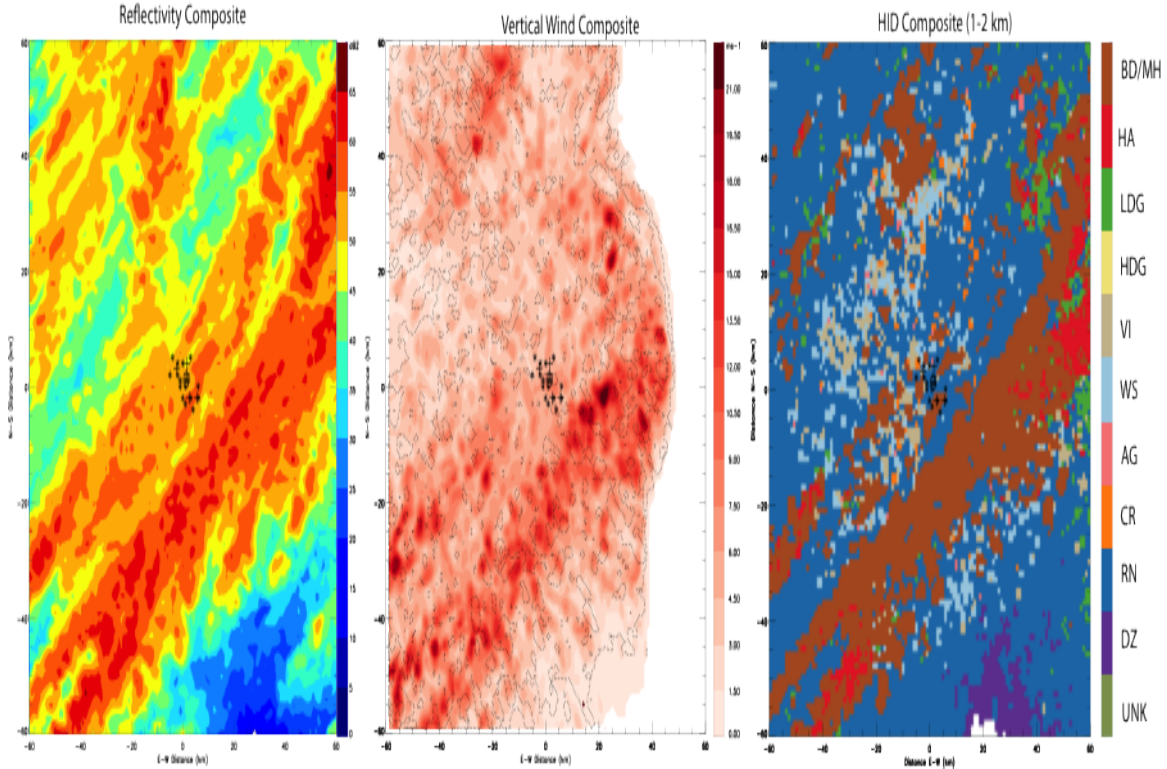


FIGURE 4.4. Swaths of storm motion through the 08-1130 UTC time period of reflectivity (left), velocity (center), and MWHID (right). Dots show disdrometer locations clustered around the CF.

three minutes of the synthesis time for one radar, or if one radar was experiencing radome attenuation.

Firstly, to show relative accuracy of the derived vertical winds using this analysis method, we will examine a comparison to the S-band profiler located at the central facility, where the scanning radar analysis is taken from the 1 km grid point surrounding the CF. Figure 4.5 shows this comparison, where the reflectivity from the radar is the maximum reflectivity from each available radar at each point. The reflectivities compared relatively well, although in general the radar recorded stronger reflectivities that extended to greater heights compared to the profiler. This difference is likely due to the method for arriving at the radar reflectivity, where the maximum value from each radar is taken at each grid point. The radar data is also

for the 1 km box surrounding the profiler, and therefore may include stronger reflectivities. Vertical velocity values also compared well, particularly in the convective updraft regions (red shades), in terms of both strength and location, while downdraft regions were disagreed in terms of both strength and location, with the profiler showing more downdraft regions than the radar.

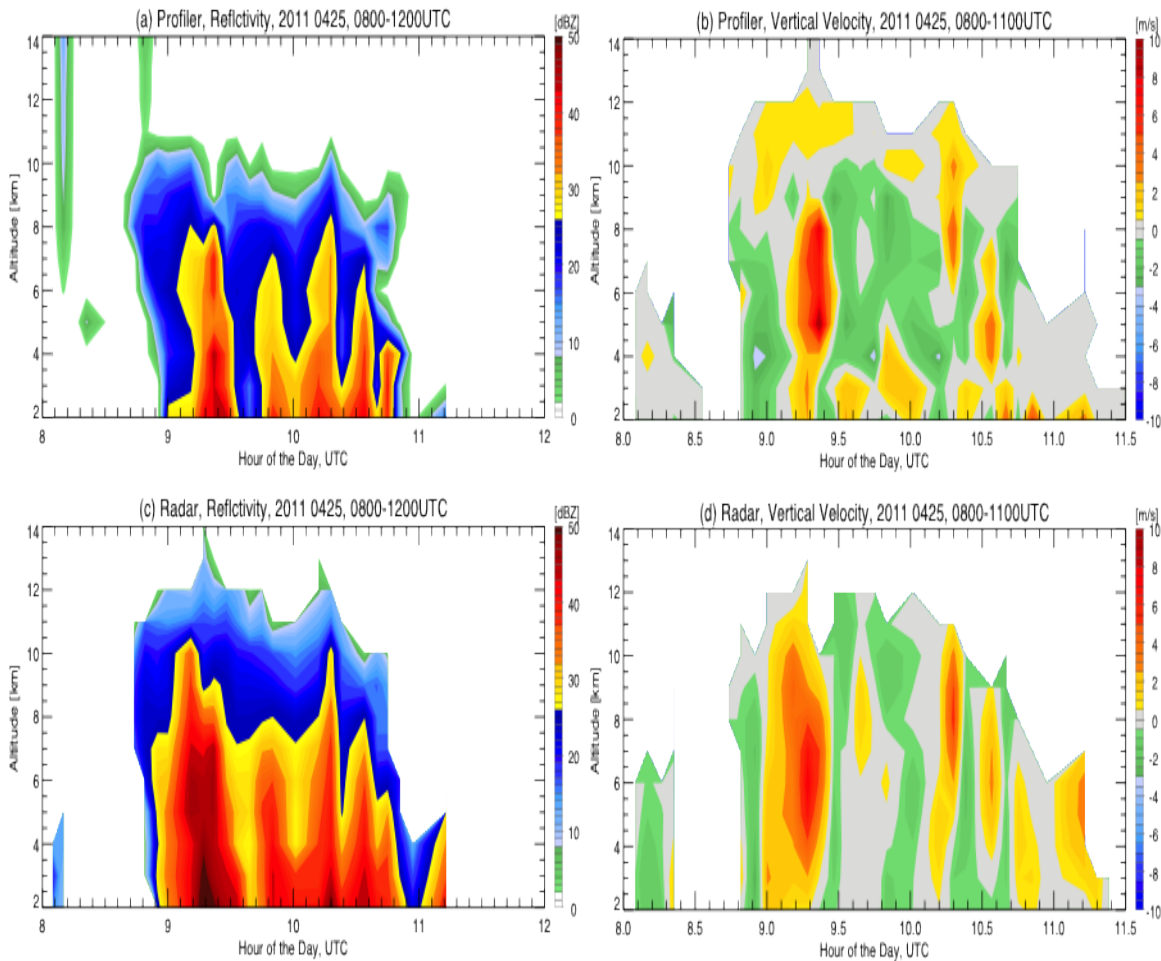


FIGURE 4.5. Comparison of interpolated profiler and composite radar reflectivity (a, c) and vertical winds (b,d) for 25 April 2011.

When examining statistics in more detail, as shown in figure 4.6, the magnitudes of the updrafts generally agreed to within the expected error value of 1 ms^{-1} . Both the profiler and the radar derived vertical winds saw the mean values peak at approximately 8 km in

height. The maximum updraft has more variation in the higher resolution profiler data than the radar derived winds, but both have a similar shape and have peaks at approximately 5.5 km in height. In contrast, the downdraft regions have the largest differences. Below approximately 10 km, the profiler measures vertical wind speeds that are consistently larger than those found by the multi-Doppler analysis for both mean and maximum downdraft velocities. In general the difference is still on the order of 1 m s^{-1} in most areas. These larger downdraft values contribute to the overall mean velocity by making it more consistent at 0 m s^{-1} , while the multi-Doppler vertical wind speed means exhibit upward motion dominating in the mid to upper levels of the atmosphere and downward motions dominating the lower regions of the storm and the extreme upper regions.

The differences between the profiler and dual-Doppler winds noted above may be attributed to a number of things. First, the profiler data was smoothed to match the resolution of the radar data in both time and space, while the multi-Doppler winds were shown only for the column directly above the profiler. The large varying areas of updraft are likely caused by the high resolution of the profiler data, resulting in higher values. Another reason for the differences could be due to the difficulty of the scanning radars to detect surface divergence due to beam geometry (Nelson and Brown, 1987). There may also be errors in the fall speed being applied to the profiler.

Based on this comparison, we conclude that the multi-Doppler wind analysis is able to recover vertical motions to within 1 m s^{-1} with a bias for underestimating downward motions and may therefore be used in this and other cases to examine the three dimensional kinematic structure of convective storms.

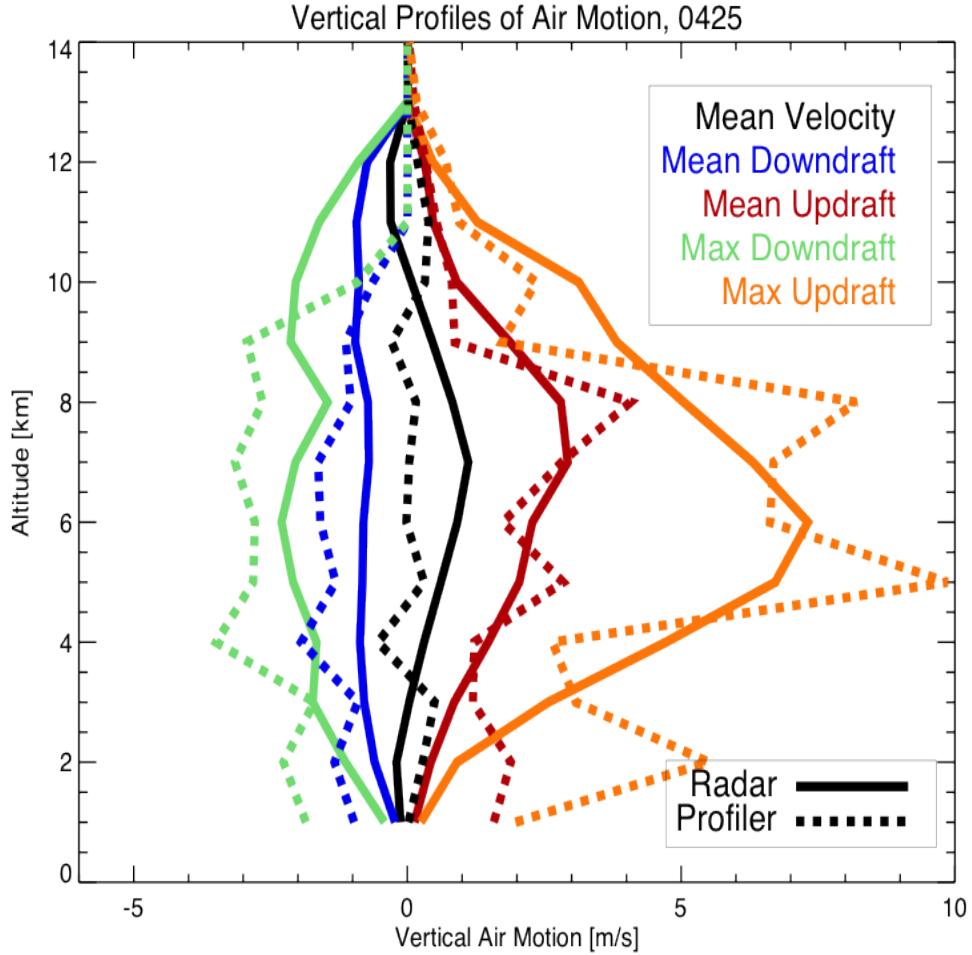


FIGURE 4.6. Statistical comparison of profiler vertical winds versus dual-Doppler derived vertical winds. Warm colors indicate updraft, cool colors indicate downdraft, with black indicating the combined mean.

4.1.1.2. *Kinematic and Microphysical Analysis.* On this day, the storms could be described as organized elevated convection with a general southwest to northeast movement, as shown in figure 4.7 at approximately 1000 UTC. The horizontal winds were around 10 to 20 ms^{-1} and were stronger in convective cores. At this time, based on hydrometeor identification results, there was a small amount of hail located in the northeast area of the gridded domain, as well as big drops scattered throughout, while rain dominated the region studied.

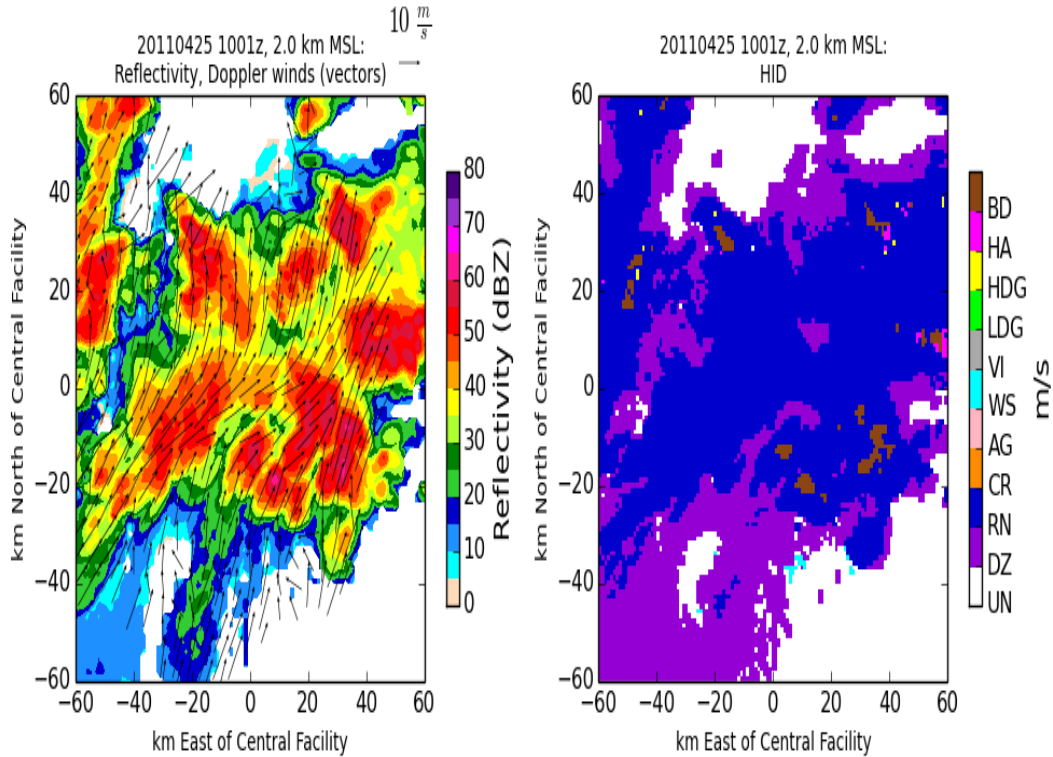


FIGURE 4.7. Gridded image of reflectivity at 2 km with overlaid winds (left) and of hydrometeor classification (right) at 1001 UTC on 25 April 2011

Total mean wind over the analysis domain and storm time frame of 0800 to 1130 UTC are shown in figure 4.8. The total mean vertical wind speed is generally slightly upward over the entire height of the storms. Mean downward motion has a maximum of -1.2 m s^{-1} and occurs at heights ranging from 4 km to 7 km, while the updraft has a maximum mean of 2.5 m s^{-1} occurring at 7 km in height. Mean echo top is also shown to be approximately 14 km.

In order to examine the evolution of storms during this case, five times were selected over the course of the analysis period, shown in figure 4.9. These times are: 0933 UTC, 1001 UTC, 1023 UTC, 1040 UTC, and 1123 UTC. The strongest reflectivities occurred during the first two times (0933 and 1001 UTC). At 0933 UTC, the strong reflectivities corresponded to stronger winds in both mean vertical motion and updraft and downdraft motion. The

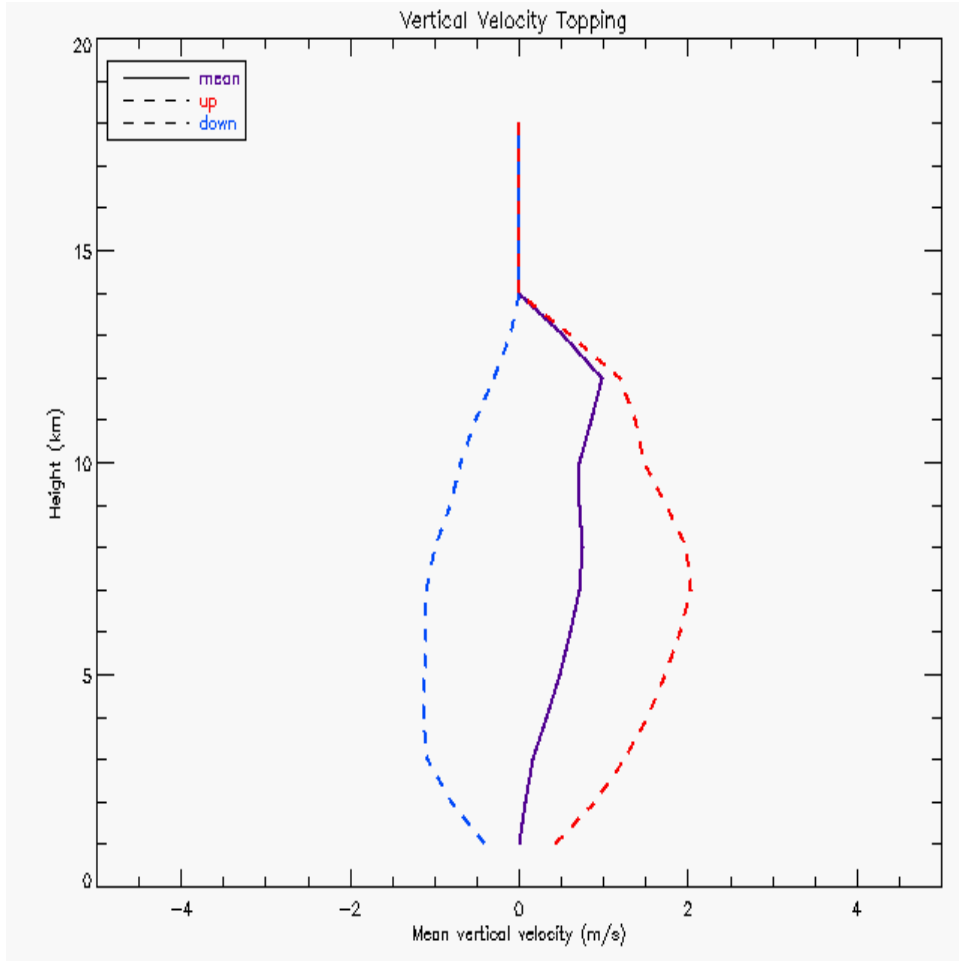


FIGURE 4.8. Mean vertical velocity from 08-1130 UTC over the entire gridded domain. Purple shows overall mean, red shows updraft velocity, and blue shows downdraft velocity

following timestep, 1001 UTC, showed nearly similar but slightly decreased reflectivity and a much lower mean vertical windspeed at mid levels, as well as weaker upward motion. Downward motion stayed approximately the same. At 1023 UTC, reflectivities continued to decrease. Mean vertical motion stayed approximately constant below 7 km and decreased at the upper levels. Updraft and downdraft speeds decreased in magnitude slightly. At 1040 UTC, reflectivity values were again decreased, this time more so in the lower troposphere below approximately 7 km. However, the mean winds strengthened at mid levels, where

downdrafts had slowed and updrafts had increased slightly. Finally, at 1123 UTC, the mean reflectivity decreased significantly and contained a brightband signature common in stratiform precipitation at around 4 km, which is consistent with the melting height found using the above sounding. Mean vertical winds decreased uniformly but especially at mid levels. Echo top height also decreased to around 11 km.

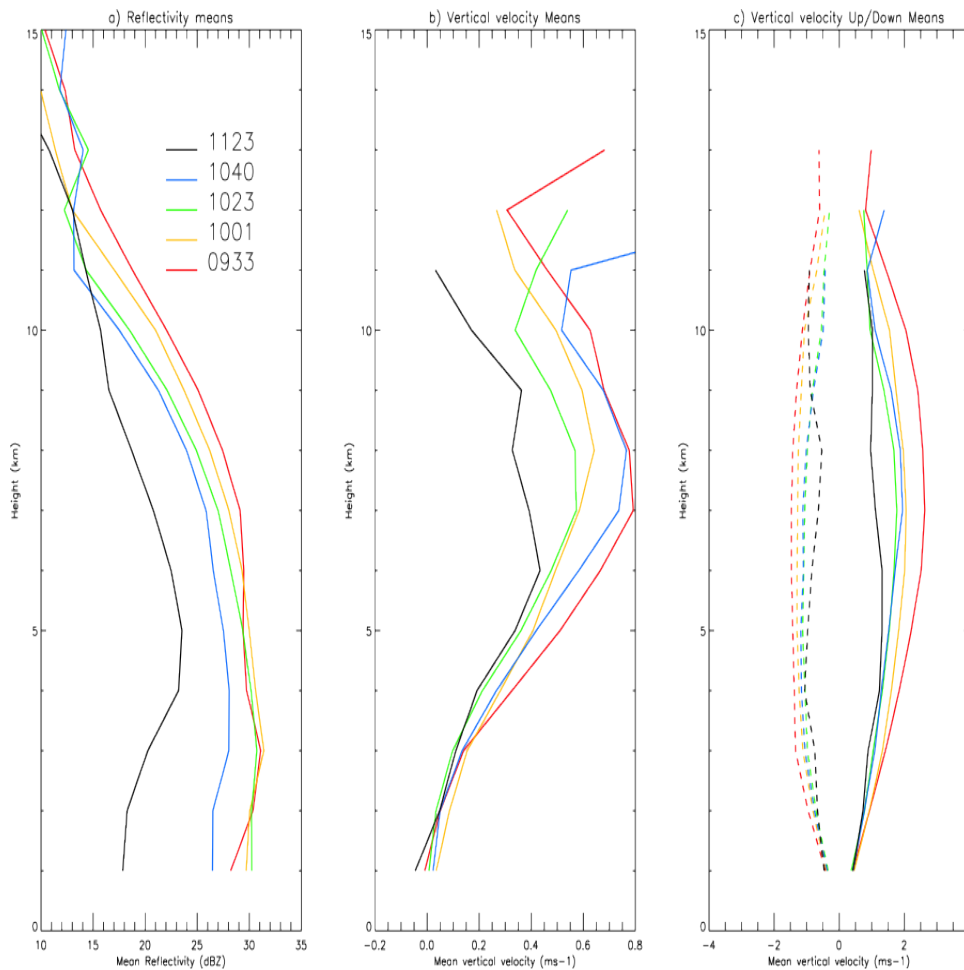


FIGURE 4.9. Reflectivity (a), mean vertical velocity (b), and up/down split mean vertical velocity (c) for the five times chosen to evaluate storm evolution.

In examining the hydrometeor classification over these five times in figure 4.10 we find that for 0933 and 1001 UTC, the times that contained the strongest upward motion, were also associated with the most frequent occurrence of hail and big drops near the surface, and

high density graupel (HDG) in the midlevels. As the vertical velocities decreased, more low density graupel (LDG) was found. This occurs because the lower vertical motions are unable to support the larger and heavier ice particles, plus supercooled water contents available for riming are also reduced. At the earlier (stronger) time periods, the height of the peak hail, LDG, and HDG was high, and lowered as storms grew weaker. In the wet snow category, there was a peak at the height of the melting layer, around 4 km. This was at its largest frequency for 1123 UTC, when the echo pattern was highly stratiform in nature. This time was also dominated by drizzle hydrometeors instead of rain and had the highest occurrence of ice crystals and aggregates above the melting layer. Throughout each time, except the final time, there is a large amount of hail shown at mid levels, but it does not appear to reach the surface with the same frequency. Instead, big drops are found at the surface, more so during the stronger times (0933 and 1001 UTC). The Storm Prediction Center showed no severe hail reports in the region of study. Therefore, it is likely that in this case the big drops were likely formed through melting hail and graupel rather than collision-coalescence, as the warm cloud depth was deep, giving the hail ample time to melt.

4.1.1.3. *Model Comparison.* This case provides a unique opportunity to statistically compare the radar observations to the simulated storm output from the WRF-SBM model. In order to do this, a convective-stratiform partitioning based on the method presented in Steiner et al. (1995) was applied to both the radar observations and the model simulated reflectivity. Reflectivity was then partitioned into shallow or deep categories, where shallow was any column with an echo top height less than 6 km. The model simulated reflectivity

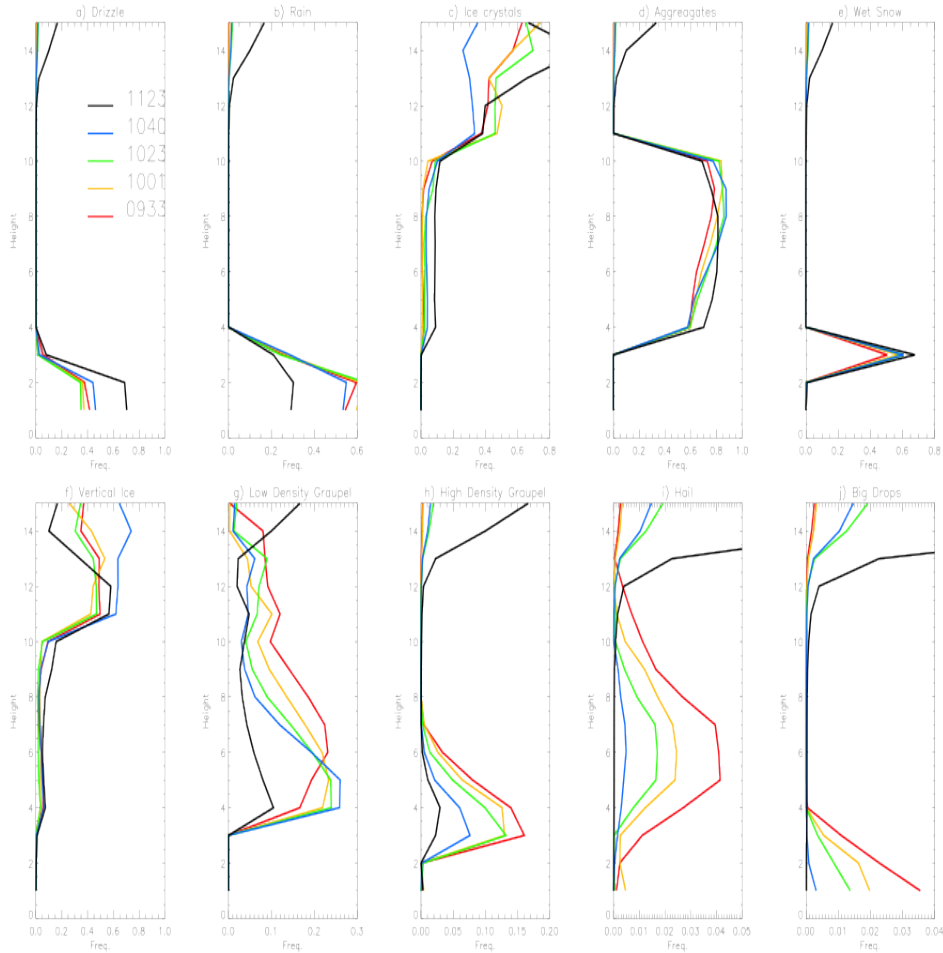


FIGURE 4.10. Frequency of each hydrometeor category as a function of height for each of the five chosen times for the 25 April case.

over a 100 km by 100 km area centered on the SGP central facility, which matches the microphysical retrieval domain for radar observations but is larger than the kinematic retrieval domain of 60 x 60 km. Both radar and model have a 1 km vertical grid spacing. The model did relatively well with its analysis of the storm, as shown in Fig. 4.11, where storms are of similar shape and organization. However, the model analyzes a much larger region, and saw these storms further to the south of the SGP site, so direct comparison could not be done. Statistical comparison of storm domain was instead utilized to compare the kinematic and microphysical properties of the case.

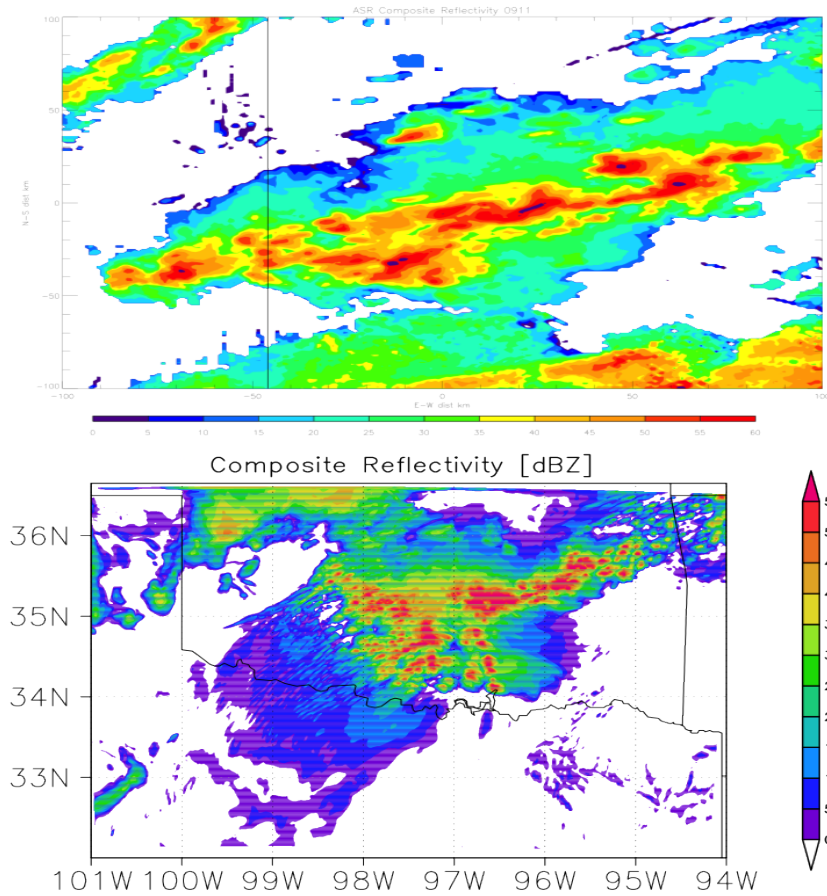


FIGURE 4.11. Reflectivity from the radar (top) and model (bottom) at 0900 UTC.

First, we will examine the reflectivity and kinematics through Contoured Frequency by Altitude Diagrams (CFADs). Figure 4.12 shows the reflectivity CFADs for the radar and model, where the observed radar reflectivity is a combined product from XSW, XSE, CSAPR, and KVNK data. In the shallow regions, both model and radar see up to a maximum reflectivity of 50 dBZ. This increases to 65 dBZ for the deep convective regions. Around the melting layer, the model shows a slight bulge in the deep convective region that reaches approximately 70 dBZ, while the observations do not have this bulge. The deep convective regions also have a tendency towards an increased reflectivity at low levels and decreased at

the upper levels, whereas the model simulated reflectivity has a slight curve to lower reflectivities near the surface. It appears the model simulations therefore have a more stratiform like brightband signature at the melting layer even in regions of deep convection. This may have occurred due to the way the model simulates reflectivity as a column, similar to a profiler observation, which would enhance any melting layer signatures. Another possible reason is that the Steiner et al. (1995) method has a tendency to include some deep stratiform columns in the deep convective category due to the reflectivity biases intrinsic in the WRF-SBM model. A sensitivity study was conducted by T. Matsui on this model using different convective-stratiform classification methods, and found that a method based on updraft velocity was the most accurate for the model, though this was not true for the radar analysis.

Next, vertical velocity CFADs were analyzed (Figure 4.13). At a quick glance, it can be seen that the observed and simulated vertical velocities are in relative agreement as they have similar shapes. However, differences in the maximum and minimum values are present. Both model and radar observations agree that there is a peak in updraft speed around 7.5 km, but disagree in the magnitude of this peak. The radar shows it to be near 20 m s^{-1} , while the model shows it as 30 m s^{-1} . These are both associated with the deep convective regions of the storms. The radar observations also show midlevel downdrafts of slightly larger values near -12 m s^{-1} , whereas the model does not show any downdraft larger than -10 m s^{-1} . Another difference between the model and radar vertical velocities is cloud top height. The radar observations are limited to 13 km in height, while the model sees increasing velocities at higher levels, with a peak height of 16 km. The shallow CFADs compare well,

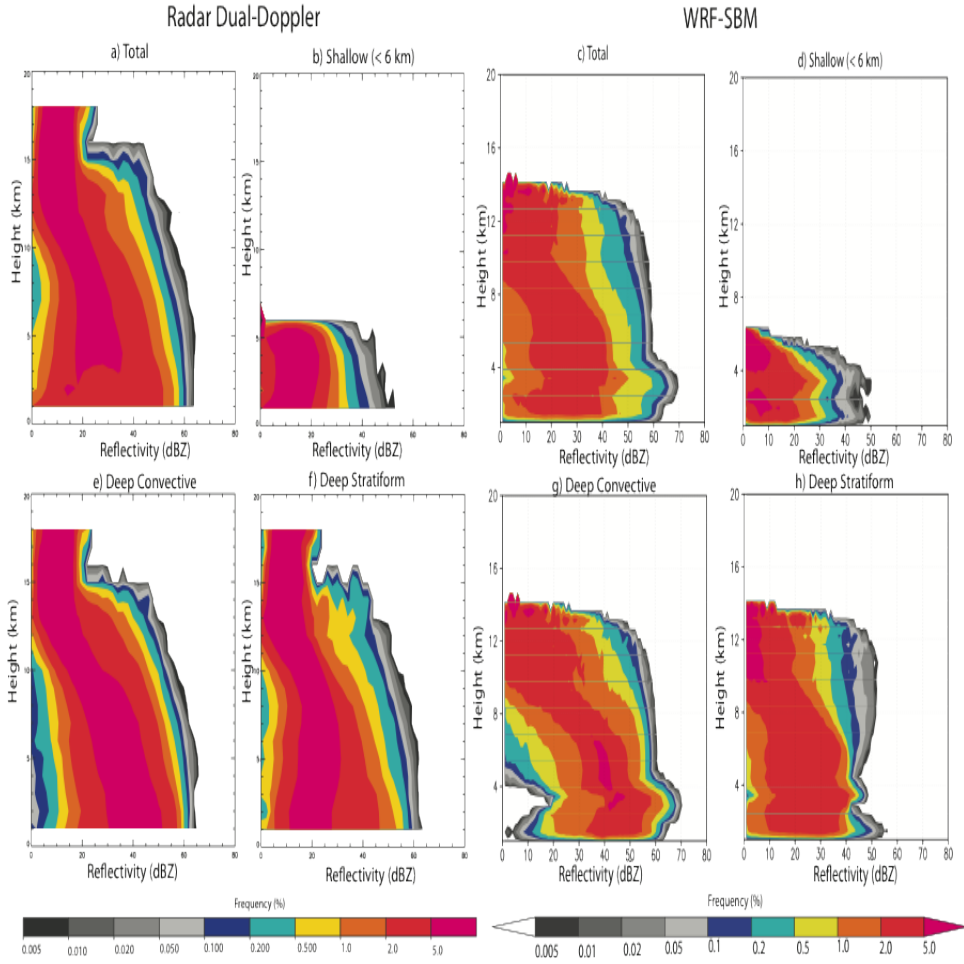


FIGURE 4.12. Reflectivity CFADs showing radar observations (left) and WRF-SBM simulations (right) for the 25 April 2011 case.

with all magnitudes less than $|8| \text{ ms}^{-1}$, although the model sees a small peak at the height of the melting layer height. The deep stratiform region is the most different in both shape and magnitude. The model sees larger updraft speeds, peaking to 20 ms^{-1} at a height of 5 km, while the radar observations only reach 10 ms^{-1} and do not have a clear maximum peak height. These maximum values are too high for typical stratiform precipitation, but these only occur in less than 0.1 % of the time. This is likely due to a possible convective stratiform partition misclassification, especially in the model. Overall, the model simulated

vertical velocities have stronger updrafts and weaker downdrafts than those from the radar multi-Doppler derived vertical velocities.

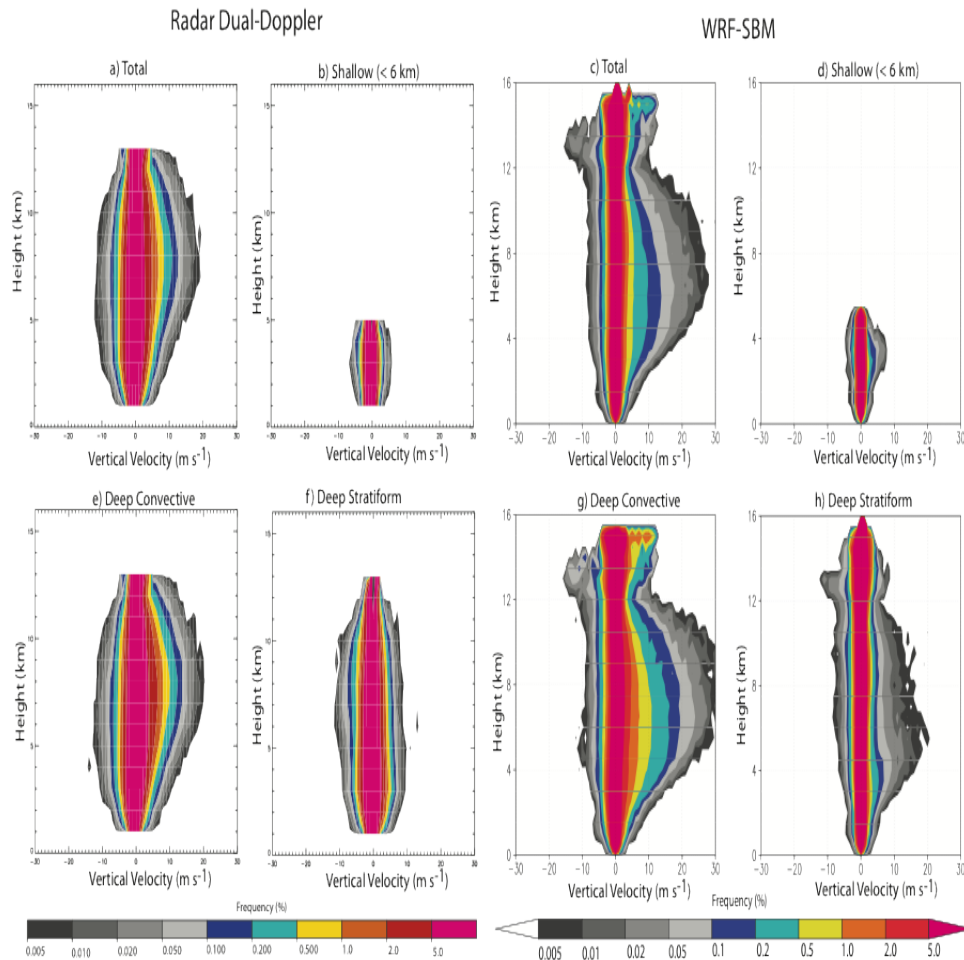


FIGURE 4.13. Vertical Velocity CFADs showing dual-Doppler derived (left) and model simulated (right) vertical motions.

Finally, the microphysical properties of the storms were statistically compared. Figure 4.14 shows the normalized frequency of each hydrometeor category at each height. The shallow stratiform region compared well, with aggregates (AG) dominating the area above the melting layer mixed with some ice crystals (CR) and low density graupel (LDG). Wet snow dominated the melting layer in both the model and radar results, at approximately 3 to 4 km in height. Below the melting layer, radar observations were dominated by drizzle

(DZ, >80%) while rain (RN, 80%) dominated in the model simulations. The model also showed rain above the melting layer, associated with supercooled liquid water droplets aloft that the radar observations did not identify. Between the model and the radar observations, the deep stratiform region was similar below 10 km, although the model also noted the presence of high density graupel (HDG) aloft and saw hail (HA) and big drops (BD) at the surface. The radar observations again saw drizzle dominating below the melting layer, while the model was dominated by rain and also saw some supercooled liquid water drops above the melting layer. Above 10 km, the radar observations showed the clouds to consist mostly of ice crystals, while the model saw appreciable amounts of ice crystals, aggregates, and low density graupel, mixed with a small amount of high density graupel. In the deep convective regions, the agreement between radar and model was similar again below 10 km. The model shows a higher frequency hail and big drops at low levels, with some hail even reaching the surface, whereas the observations see hail aloft and only big drops at the surface, both in lower frequencies than the simulations. The presence of hail at the surface noted in the model was not observed in the region, as there were no hail reports associated with storms on this day. Above 10 km, once again, drastic differences were found between the MWHID run on the radar analysis and the microphysical classifications of the model simulations. The radar observations show a majority of ice crystals with a mix of low density graupel, while the model shows a mix of all the ice hydrometeor categories, except wet snow, in large fractions.

In order to better understand the differences noted in the statistical comparisons between the hydrometeor classifications for the radar and model simulation, we must look at a vertical cross section from both. Due to location and timing differences, exact cores are

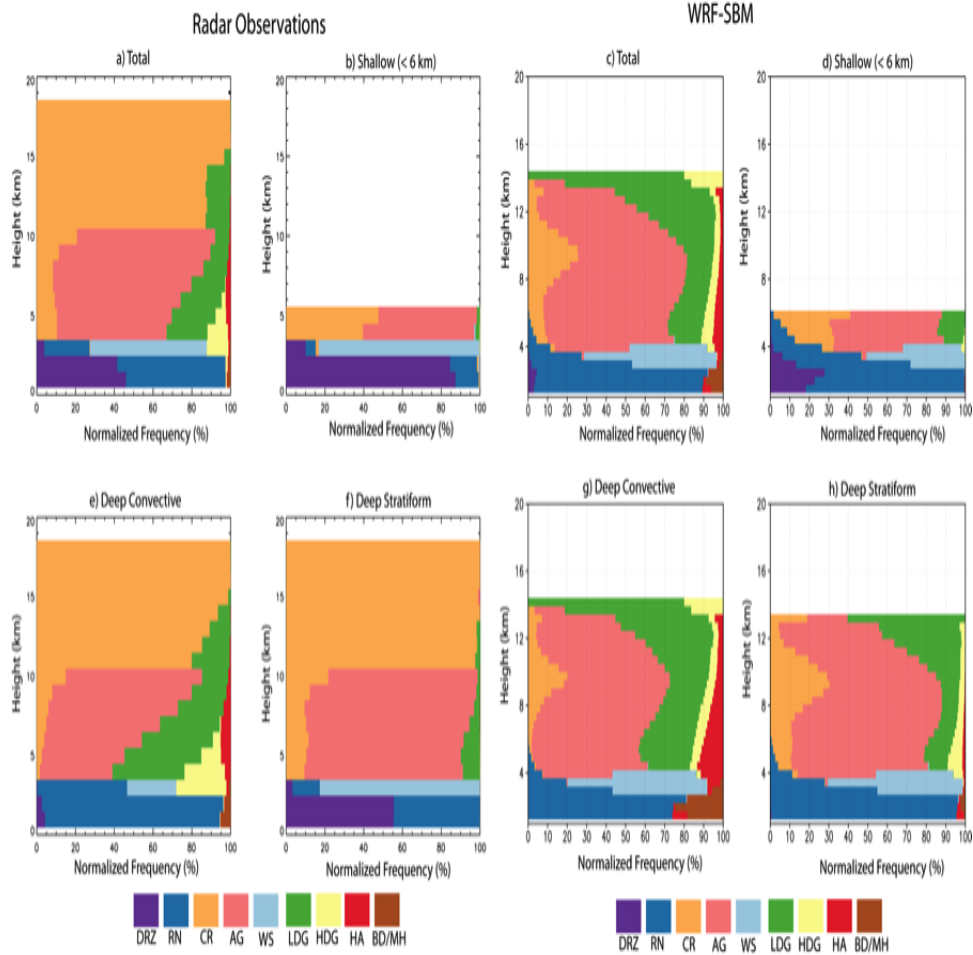


FIGURE 4.14. Normalized frequency of each hydrometeor category with height for Drizzle (DZ), Rain, (RN), Ice Crystals (CR), Aggregates (AG), Wet Snow (WS), Low Density Graupel (LDG), High Density Graupel (HDG), Hail (HA) and Big Drops/Melting Hail (BD/MH).

not compared, but we will be comparing convective volumes of similar intensity and vertical development. Both cores chosen for cross sectional analysis have reflectivities of 60 dBZ, 40 dBZ reflectivities up to 10 km, and echo tops around 12 km. The model hydrometeor classification is noisier due to the inability to resolve 1 km features. However, a general pattern still emerges that is useful for comparison. Figure 4.15 shows the model cross section which will be discussed first.

In figure 4.15, the black line represents the 0 dBZ threshold for reflectivity used for HID model statistics in figure 4.14. In the HID profile, this means that the majority of ice crystals aloft and drizzle below the melting layer were not shown in the statistical analysis. There is also a region of low confidence (less than 40%) at the transition in classification between aggregates and ice crystals, as well as around regions of big drops. Confidence is high in the convective core above the melting layer and in the stratiform region, and is moderate in other regions surrounding the convective core. The model also showed hail cores aloft that were surrounded by low density graupel, and revealed aggregates in regions of weaker echoes near storm edges and in the stratiform region on the downshear side of the storm. Confidence is highest in the hail cores and decreases quickly in the surrounding region of low density graupel. The low to moderate confidence surrounding the convective core suggests that the model has a mix of many different hydrometeor types in these regions.

Without the 0 dBZ threshold, the statistical comparison has much better agreement, as shown in figure 4.16 a, b, e, f compared with the observations in figure 4.14. Ice crystals now dominate above 10 km in height, and below drizzle is now present in the shallow regime below the melting layer. Therefore, it can be concluded that the model underestimated the radar reflectivity of ice crystals and drizzle.

Comparing this cross-section to one from the radar observations (figure 4.17), we see similar trends of hail aloft encircled by low density graupel, and big drops below the hail at the surface. It is difficult to compare the vertical velocities, as the model cross section has many small cores and the radar cross section has one main core. However, it can be noted that in the stratiform region, the radar observations show more downward motion while

WRF-SBM 25 April 2011 09 UTC

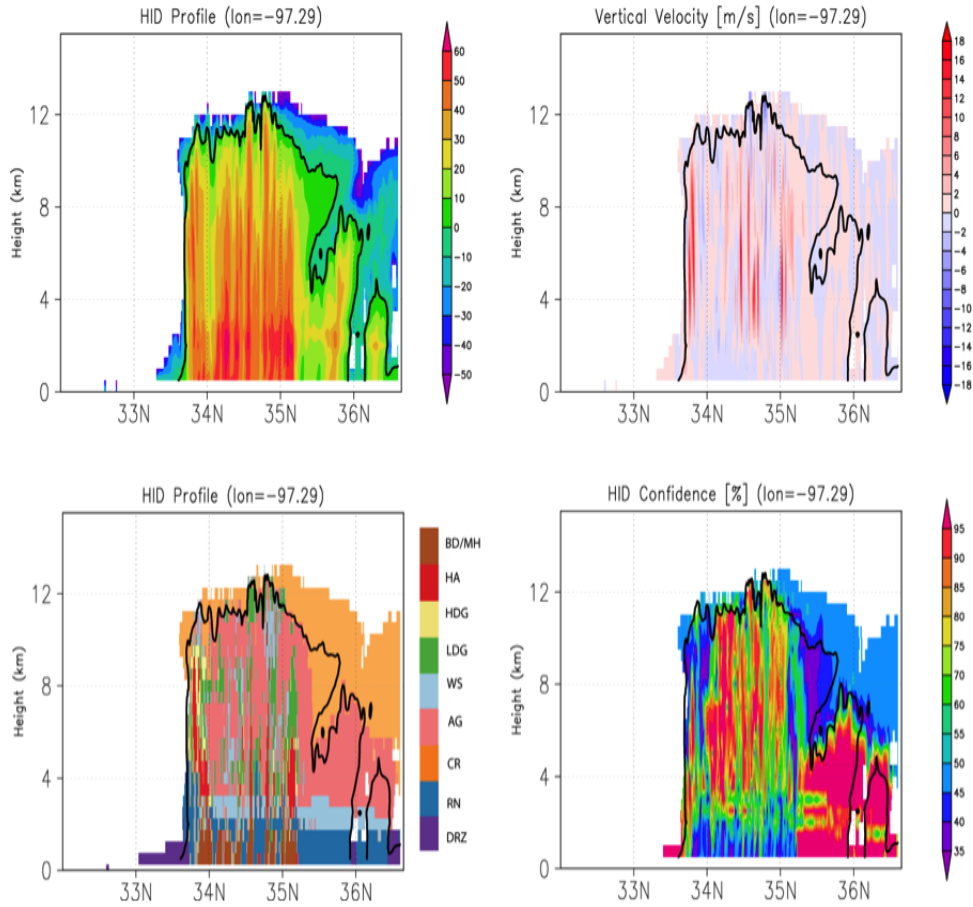


FIGURE 4.15. Cross section of reflectivity (upper left), vertical velocity (upper right), HID (lower left), and confidence in the HID category (lower right) for the WRF-SBM simulated data. The black outline is the 0 dBZ contour.

the model shows a mix of weak upward and downward motions. It may also be noted that the upward and downward motion cores are similar in magnitude and altitude. Both the model and the observations show an association between hail and big drops. The model big drops are directly caused by melting hail, as these big drops are greater than 5 mm, a size that would result in drop breakup if they were completely liquid through vortex instability O'Brien (1961). Assuming a density of 900 kgm^{-3} means that a high density graupel particle with a diameter of 5.25 mm would form a drop of 5 mm in diameter through melting. Similar

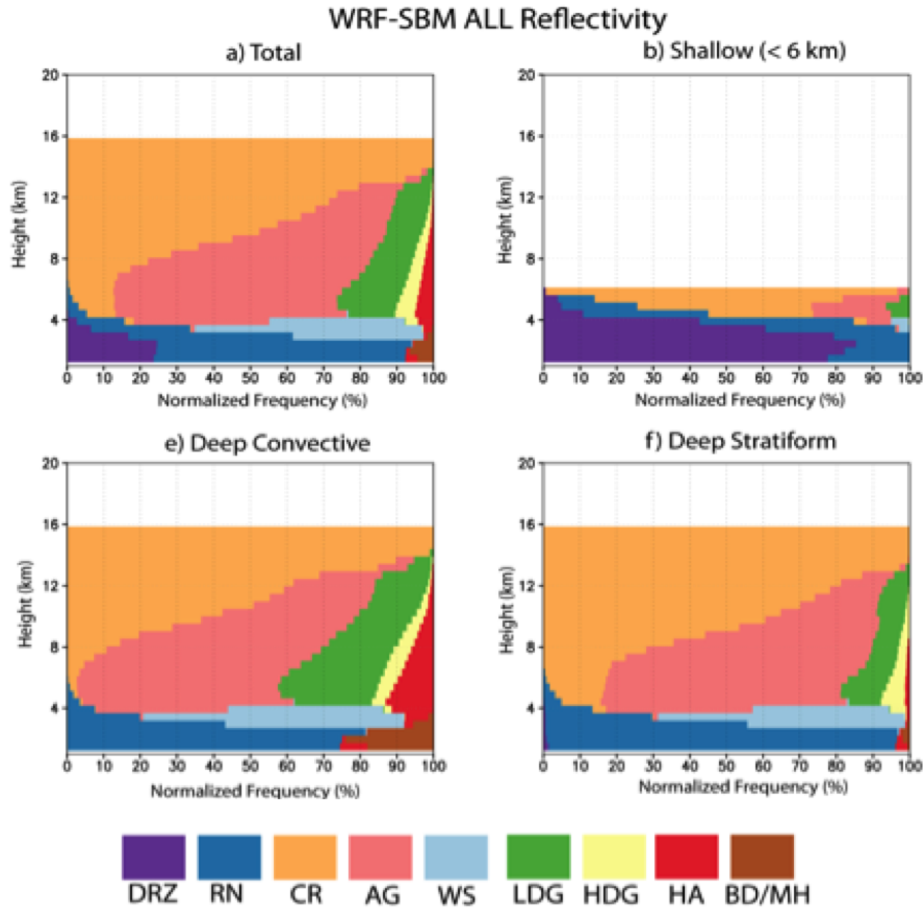


FIGURE 4.16. HID frequency for the WRF-SBM simulation with no reflectivity threshold.

calculation for a low density graupel particle reveals that a 7 mm particle would have to exist in order to melt to a 5 mm or greater drop diameter, which is not physical. Therefore, the big drops were likely formed from melting high density graupel or hail in the warm cloud depth as the particles fell.

One major source of the differences between the microphysical analysis of the radar and the model is how the hydrometeor classification was applied. The radar observations examine size and density characteristics indirectly through polarimetric signatures, while the model uses reflectivity in a weighted manner based on the theoretical definitions of these

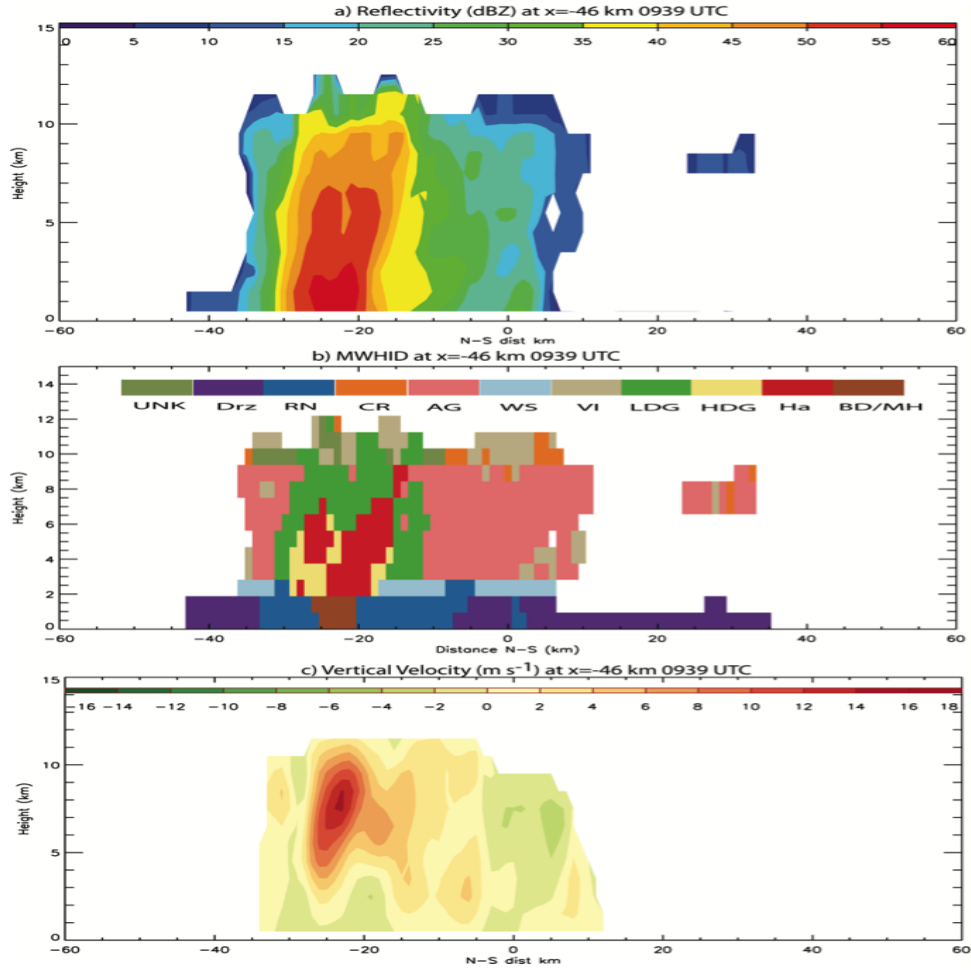


FIGURE 4.17. Cross section of the radar observations at 0939 UTC

characteristics. For instance, membership beta function of the multi-wavelength HID has wide slope factors and restricts high density graupel to occur between temperatures of ± 10 °C, which could result in a relatively small vertical extent of its classification in the observations. The model has no temperature restriction on graupel. Another reason for the differences could be the ambiguity between categories. There is little distinction between high density graupel and low density graupel other than HDG having a slightly higher reflectivity and lower Z_{dr} . Further, the aggregate category tends to be the background (i.e., default) category selected in regions where another category does not fit in the radar analysis. This

implies that in the radar analysis, regions of aggregates may be close to another category, one that the model simulation may have classified in the region. Had that category been classified instead of aggregates, the comparison between model and observations may have more similarities.

4.1.2. 1 MAY 2011. This day began colder than expected for Oklahoma in May. A cold front had just gone through the day before (figure 4.18) and left behind dry, cool surface air. These conditions are shown in the sounding in figure 4.19, which is more characteristic of transitional spring weather in this region.

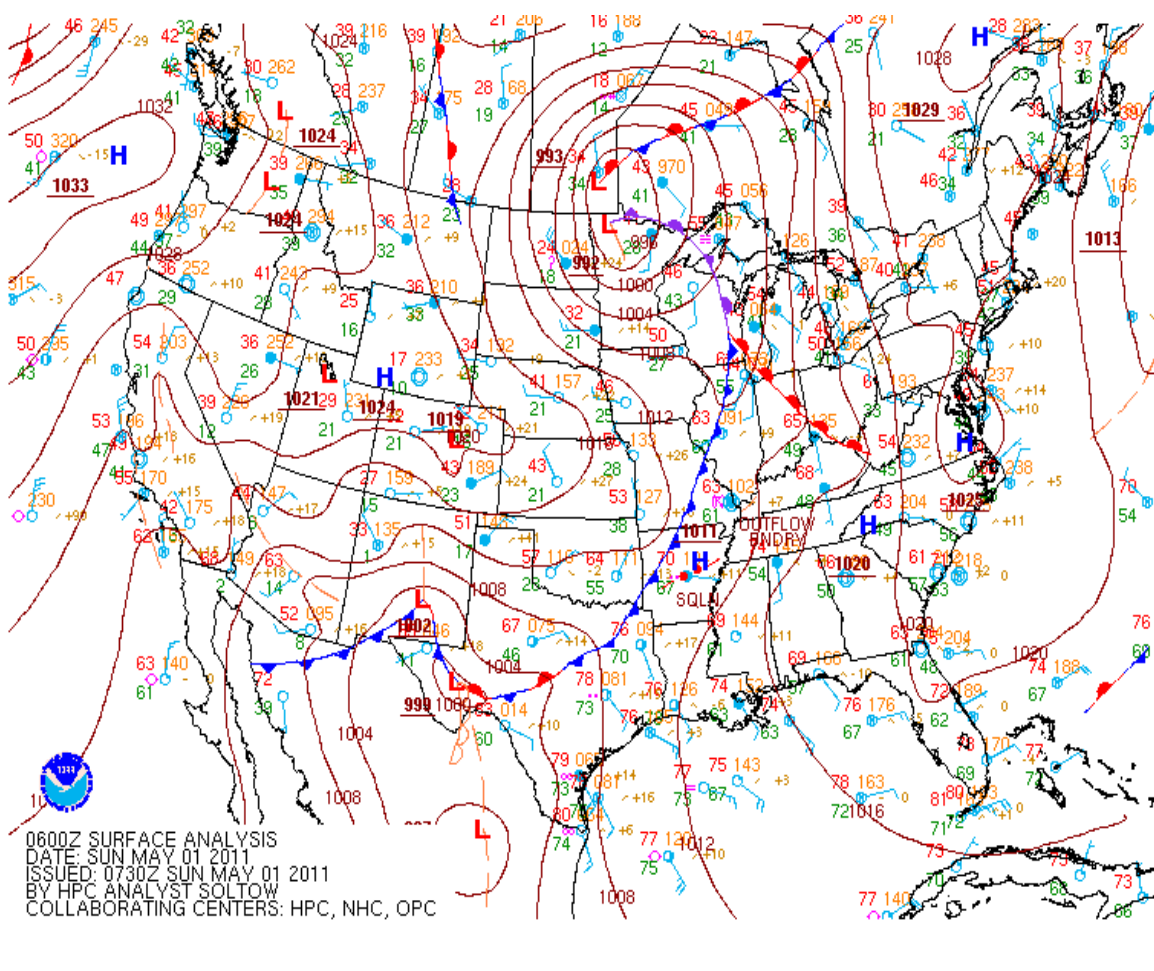


FIGURE 4.18. Surface analysis and frontal positions for 0730 UTC on 1 May 2011.

The sounding also showed a high LCL at approximately 750 mb. This LCL was above the 0 ° C isotherm and therefore there was no warm cloud depth. There was also no CAPE. The cool dry surface air was topped with moist air from the south, leading to a moist sounding at upper levels with a large dry area near the surface. This meant that any precipitation that formed was most likely derived from cold cloud processes.

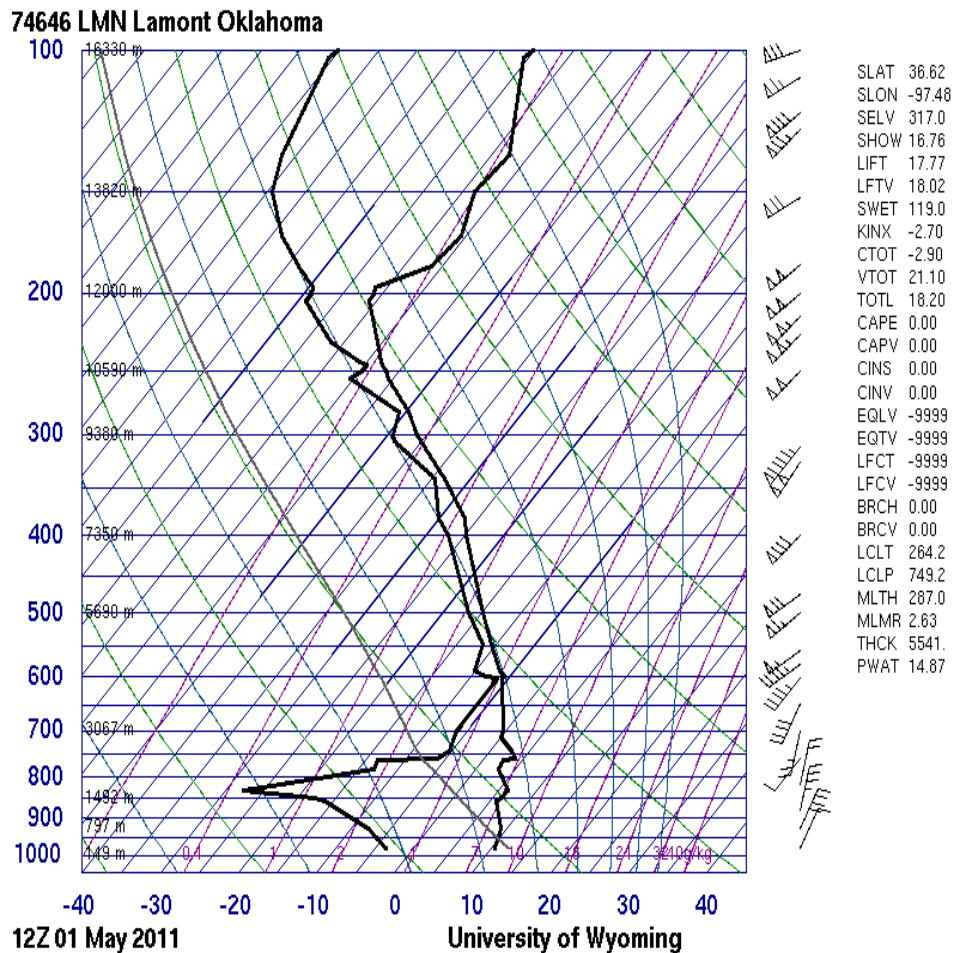


FIGURE 4.19. 12 UTC sounding for Lamont, Oklahoma.

Precipitation began to form behind the cold front and moved through the SGP area to the southeast. There was no reflectivity above 50 dBZ present on this day. A representative reflectivity image taken at 1330 UTC is shown in figure 4.20, overlaid with wind vectors.

Radars available this day were KVNX, CSAPR, XSW, and XSE. The time period chosen for study was 11-1330 UTC, as this was the only time when there was precipitation in the SGP region.

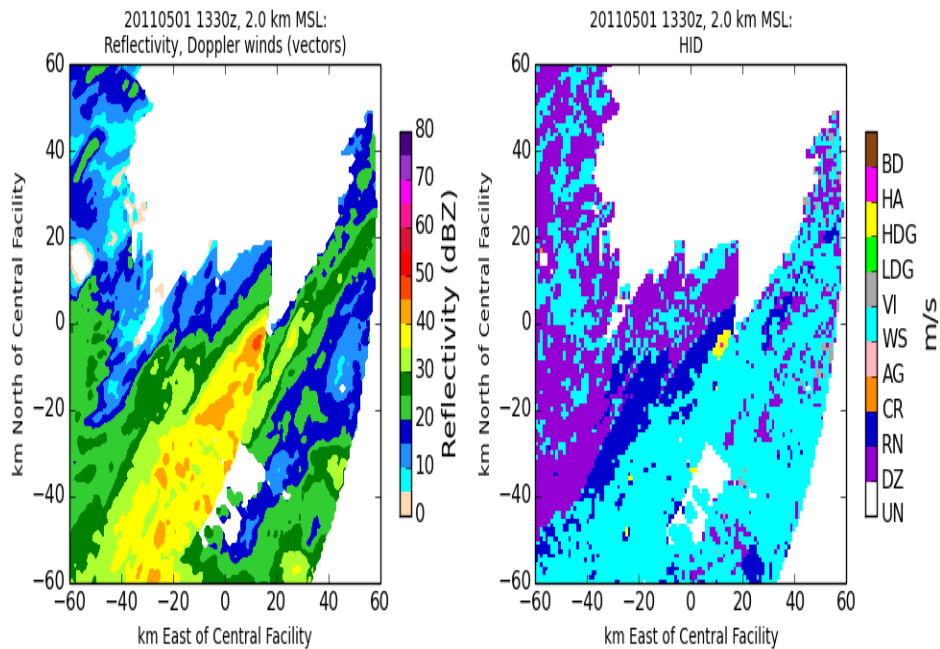


FIGURE 4.20. CAPPI of reflectivity (left) and HID (right) with overlaid wind vectors taken at 2 km at 1330 on 01 May 2011.

4.1.2.1. *Kinematics.* Due to the more stratiform, cold weather nature of the precipitation on this day, storms generally topped out at approximately 9 km. Mean vertical winds were weak, never more than 1 m s^{-1} in the updraft while just barely reaching -1 m s^{-1} in the downdraft, as can be seen in figure 4.21. Means hovered near 0 m s^{-1} but tended toward downward motion near the surface, perhaps induced by low level evaporation. The upward

motion peaked at 3.5 km in height, while the downdraft motion peaked slightly lower at 3 km. Both upward and downward motions showed an irregular shape with a secondary peak of smaller magnitude at approximately 7 km. This is due to the

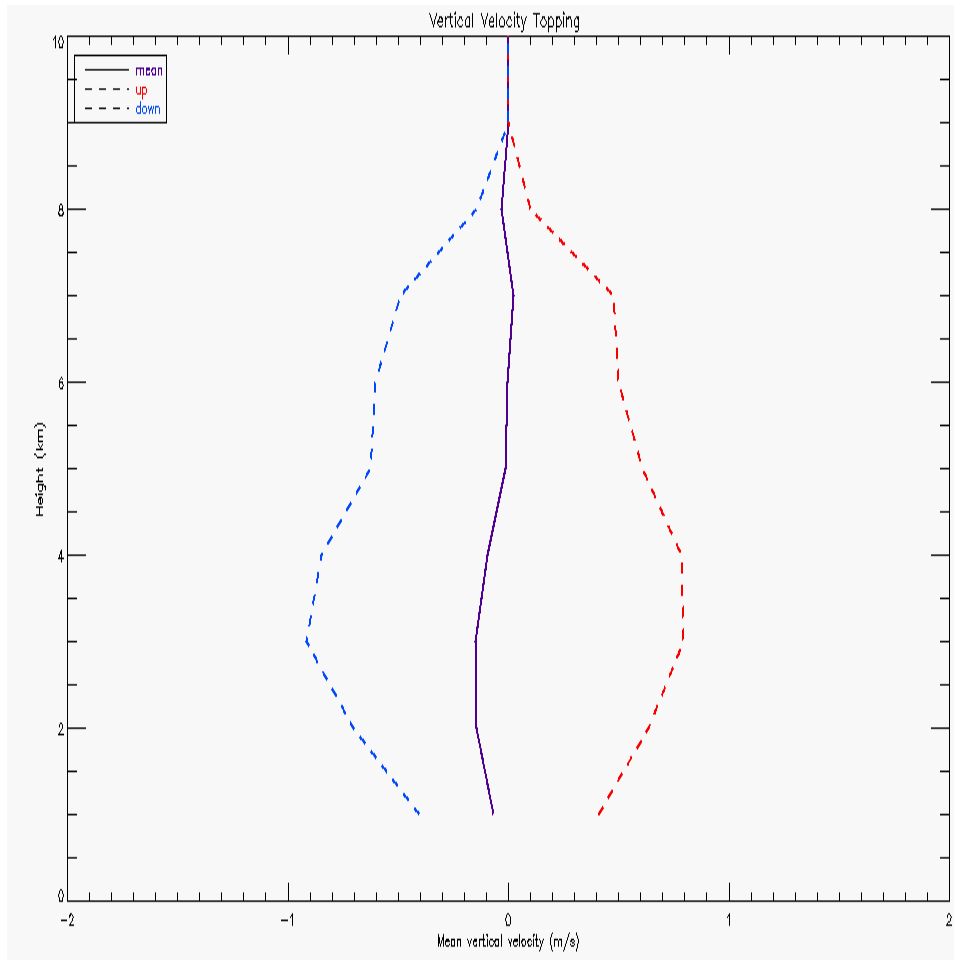


FIGURE 4.21. Mean vertical velocity over 11-1330 UTC split into upward and downward motions. Upward motion is shown in red and downward motion is shown in blue. Overall mean is purple.

The maximum vertical winds (figure 4.22) were 15 ms^{-1} upward and -10 ms^{-1} downward. These numbers likely come from a stronger more convectively driven cell that passed over or near the grid box over the SGP site. The updraft peak occurred at 5 km in height while the downdraft peak occurred lower at 4 km in height.

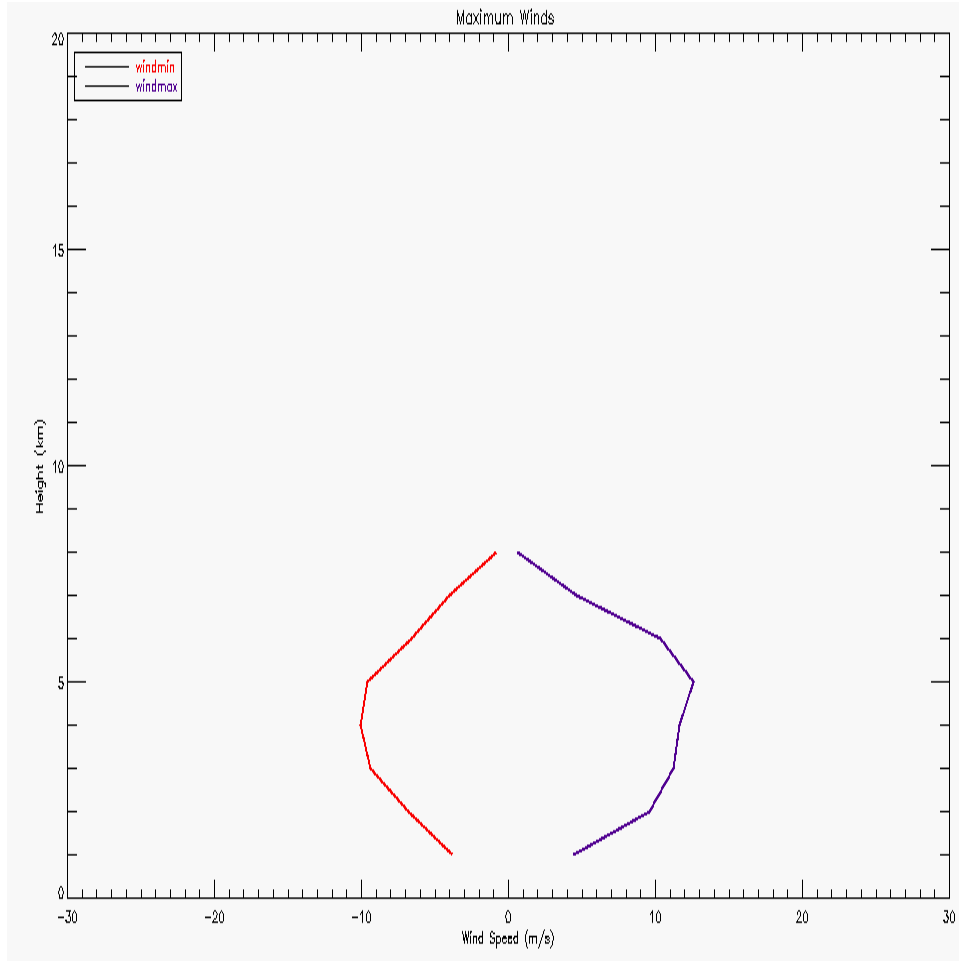


FIGURE 4.22. Maximum and minimum vertical velocity present over the studied region between 11 and 1330 UTC. Purple depicts maximum wind speeds and red depicts minimum wind speeds.

In order to better understand the evolution of the storm, we next examine three timesteps of vertical winds. In figure 4.23, red is the earliest time of 1120 UTC and also has the strongest mean vertical motion with no overall downdraft influence. The mean winds decrease with time at 1210 UTC and again decrease to being dominated completely by the downdraft at 1300 UTC. The final time (1300 UTC) also has the shallowest echo top height of just 5 km. This implies that the storm was most convective at the beginning of the time

period of study and was dissipating and becoming more stratiform towards the end of the time period.

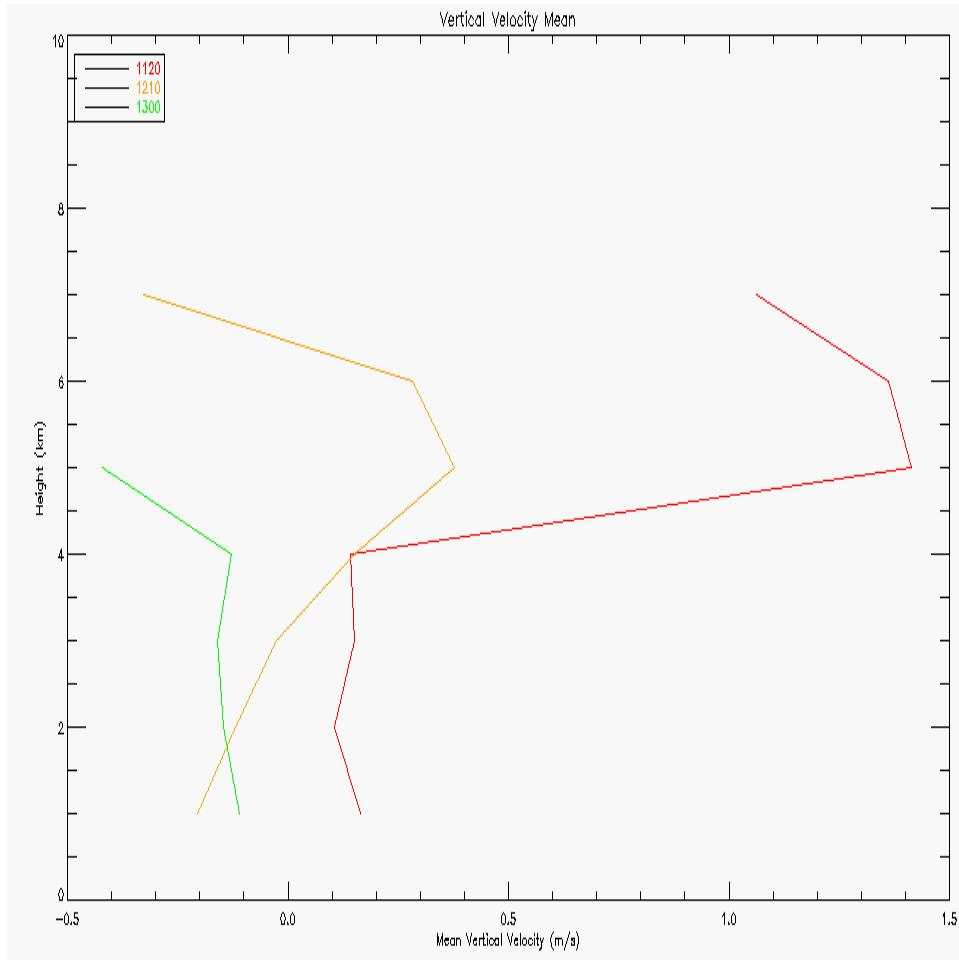


FIGURE 4.23. Mean vertical velocities for the three times chosen (1120, 1210, 1300 UTC)

Splitting the vertical motion means between upward and downward motion can also provide useful insight into the storm evolution. In figure 4.24, the first time of 1120 UTC is dominated almost completely by upward motion at the top of the storm, with a small contribution from the downward motion below. The upward motion peaks at just under 2 m s^{-1} at a height of 7.5 km. The next time has very little upward motion, and stays constant at 0.5 m s^{-1} while the downdraft shows a double peak structure, with the strongest one being

-1 ms^{-1} at 3 km in height and the weaker peaking at just under 1 ms^{-1} at a height of 6 km. This middle time period has the same echo top height as the first (strong) time, but due to the weakening updraft and strengthening downdraft at upper levels it is clear that the echo is beginning to dissipate. The final time has the strongest downward motion, reaching nearly -2 ms^{-1} at a height of 3 km. This time has an updraft resembling the first time in magnitude at 1.5 ms^{-1} , but peaks much lower at just 3 km. Downdrafts dominate over upward motion as the storm dissipates and becomes more shallow. The echo top in the final time is the lowest, at 5 km.

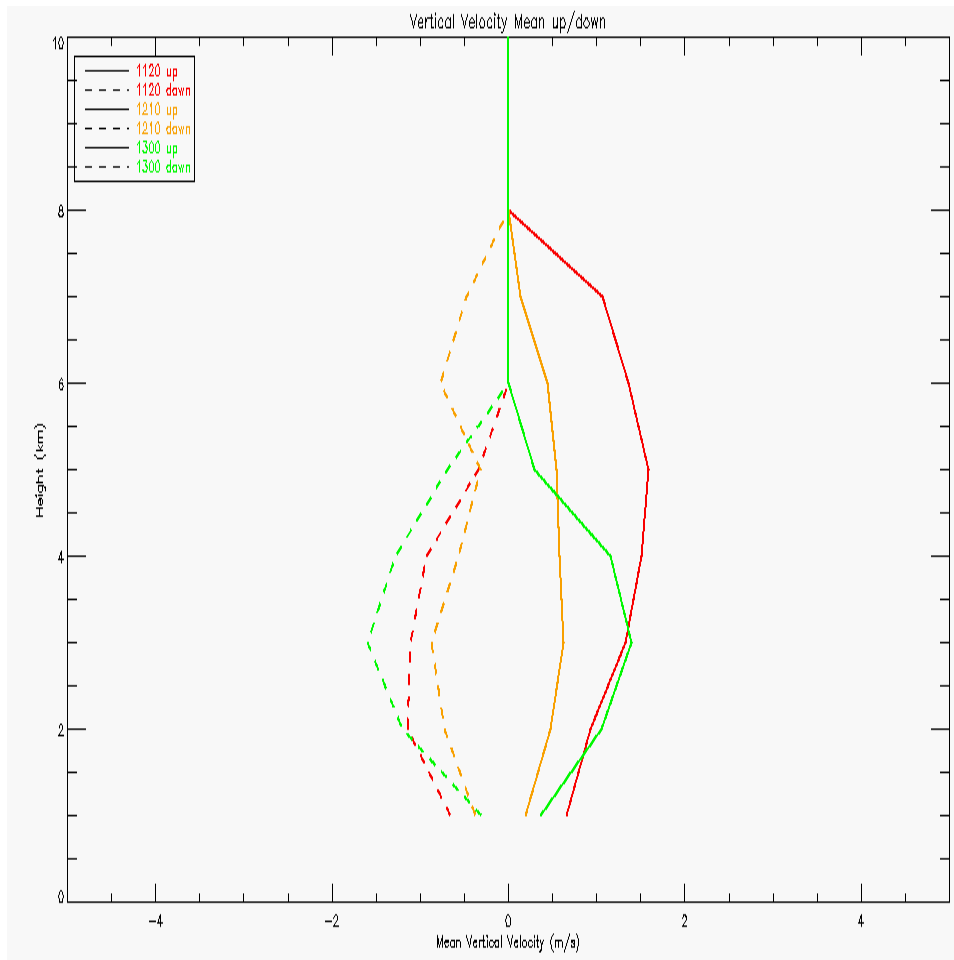


FIGURE 4.24. Mean vertical velocity split by upward and downward motion for each of the chosen three times (1120, 1210, 1300 UTC).

4.1.2.2. *Microphysics*. Finally, in the analysis of this case, we will examine the hydrometeor classifications present. In figure 4.25, this case is shown in purple. The HID show rain and drizzle at the surface, with ice crystals (IC), vertically oriented ice (VI) and aggregates aloft. The vertical ice category is generally noted in strong electric fields in electrified convection, which is not present in this case. However, later in the day from 16 UTC to 18 UTC, convective storms moved through producing frequent lightning. The vertical ice noted at this time may be due to a developing electrical charge in the atmosphere, or it may be a misclassification of the hydrometeor algorithm. Interestingly, wet snow is found not only to have a peak at the height of the melting layer, as expected, but also to be present at the surface, indicating that there may have been transitional season precipitation during this case. In the MC3E research logs, a present scientist noted 'sleet' falling at the surface. This confirms the hypothesis that this day exhibited a transitional weather pattern, although 'sleet' and 'wet snow' are not the same, and the log may not have occurred at the same time as the radar indicated surface wet snow. The melting layer also contained a peak in low density graupel and high density graupel, with the frequency of these extending upward toward the top of the storm. The particles that reached the highest heights were aggregates, ice crystals, and vertical ice, although vertical ice had the highest peak of these. Not surprisingly, there were no big drops or hail found on this day due to the more stratiform nature of this case, and the abundance of small ice particles aloft.

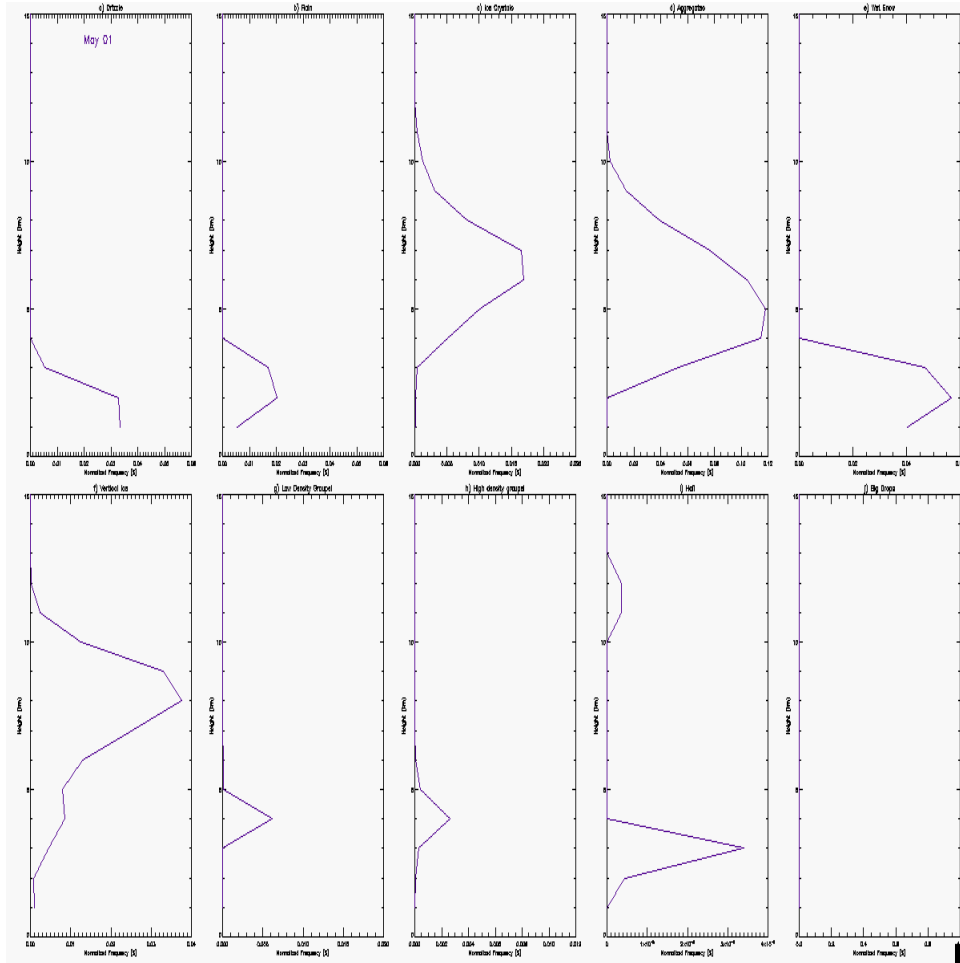


FIGURE 4.25. Frequency of hydrometeor classification for each category for each case.

4.1.3. 20 MAY 2011. This day was set up to be an ideal case day for many involved in the MC3E data collection. There was a cold front directly to the west of the SGP site, with a squall line to the west of the SGP already formed in the early hours of the day (figure 4.26). Temperatures at the surface were warm, at 24 °C with dewpoints of approximately 19 °C. Therefore, the atmosphere was warm, moist and primed for convection to occur.

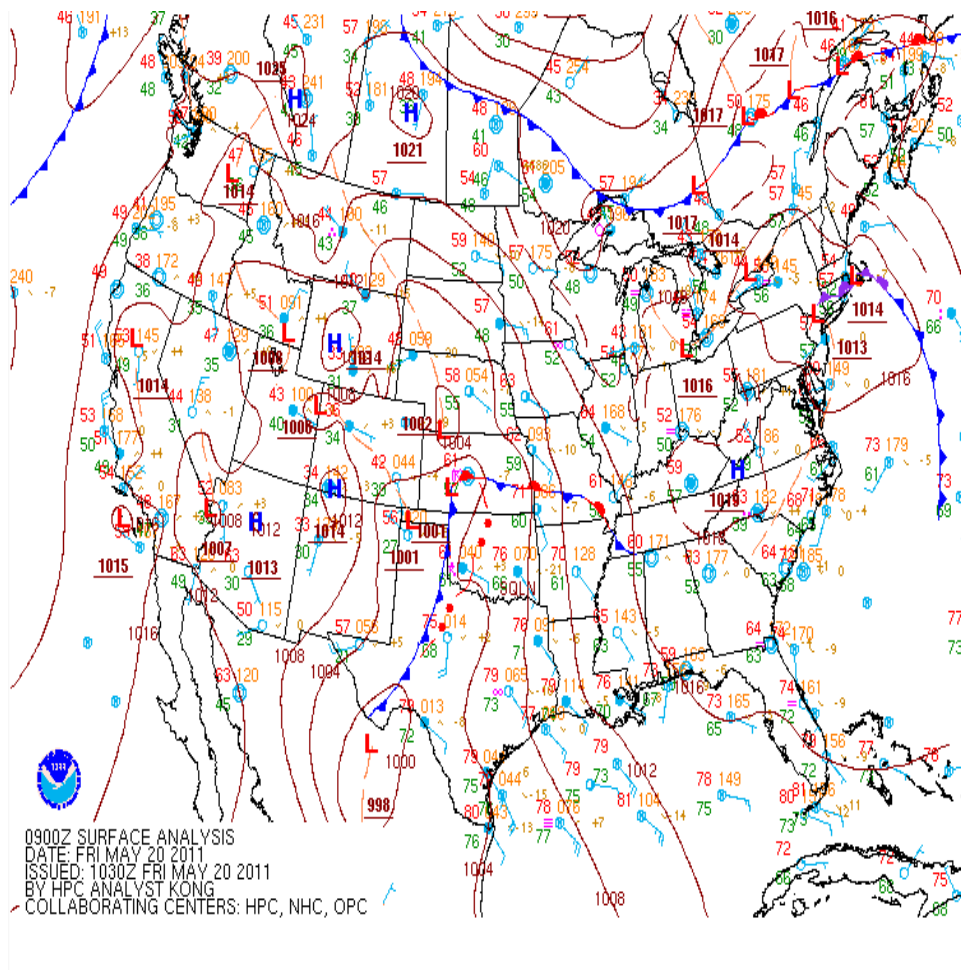


FIGURE 4.26. Surface analysis and frontal positions at 1030 UTC for 20 May case.

The sounding, however, in the evening hours at 3 UTC showed a small inversion inhibiting the release of instability (figure 4.27). Storms began forming to the west of the SGP at around 6 UTC. Unfortunately, we have no soundings during the storm initiation or development, as

something had gone wrong with the soundings launched from KLMN (Lamont, Oklahoma), and all times after 3 UTC only reached approximately 700 mb in height. At this time, the LCL is low, at approximately 900 mb.

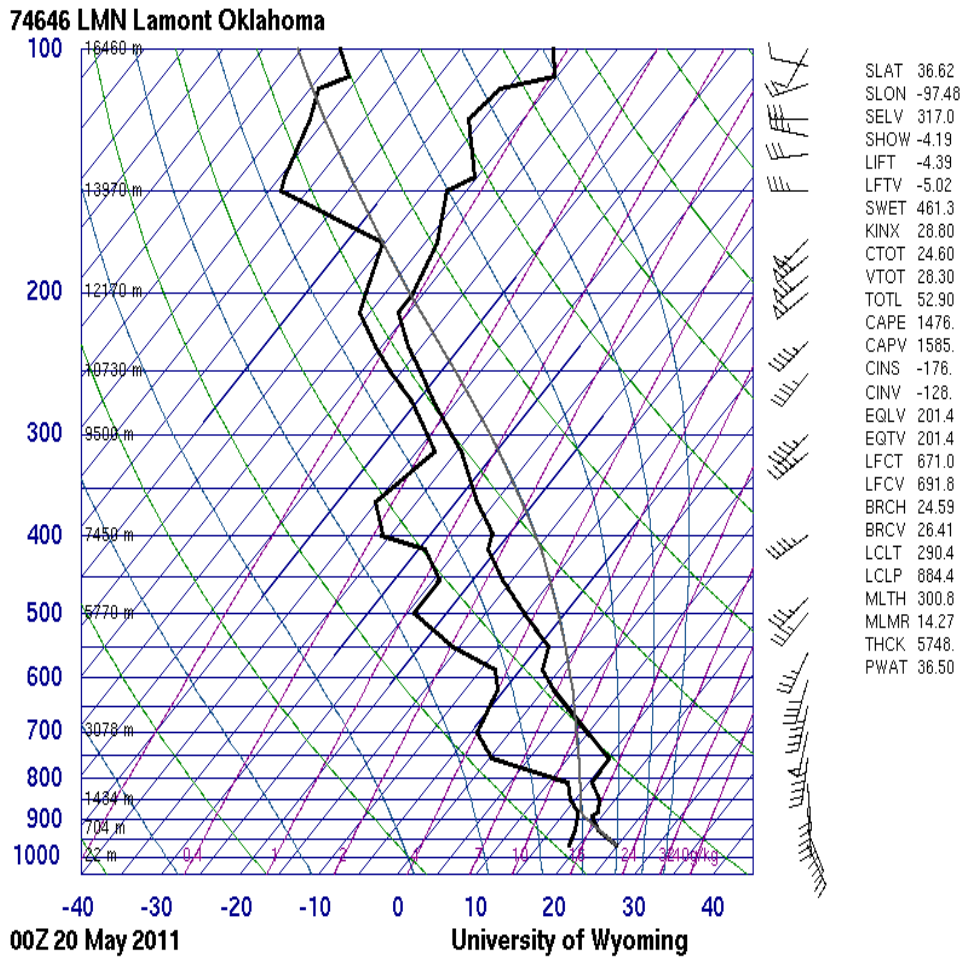


FIGURE 4.27. 03 UTC sounding for Lamont, Oklahoma.

The time period selected for analysis for this case was 6 - 10 UTC. This particular time period was chosen as storms began entering the SGP domain at around 6 UTC. A squall line quickly organized over this time to the west of the SGP and began moving east and hit the radars just before 10 UTC. Between 6 and 10 UTC, storm cells formed ahead of the squall line and moved east through the SGP domain. Unfortunately, we were unable to recover

any kinematic or microphysical details of the squall line, as the heavy rain associated with it caused serious radome attenuation for both the XSW and XSE radars. Figure 4.28 shows a time just before the squall line moved over the XSE radar and one of the last times at which wind data was available. High reflectivity values were present to 70 dBZ. The wind vector field showed convergence at the leading edge of the squall line. The horizontal winds are strong in the inflow and ahead of the storm, reaching values of over 20 ms^{-1} .

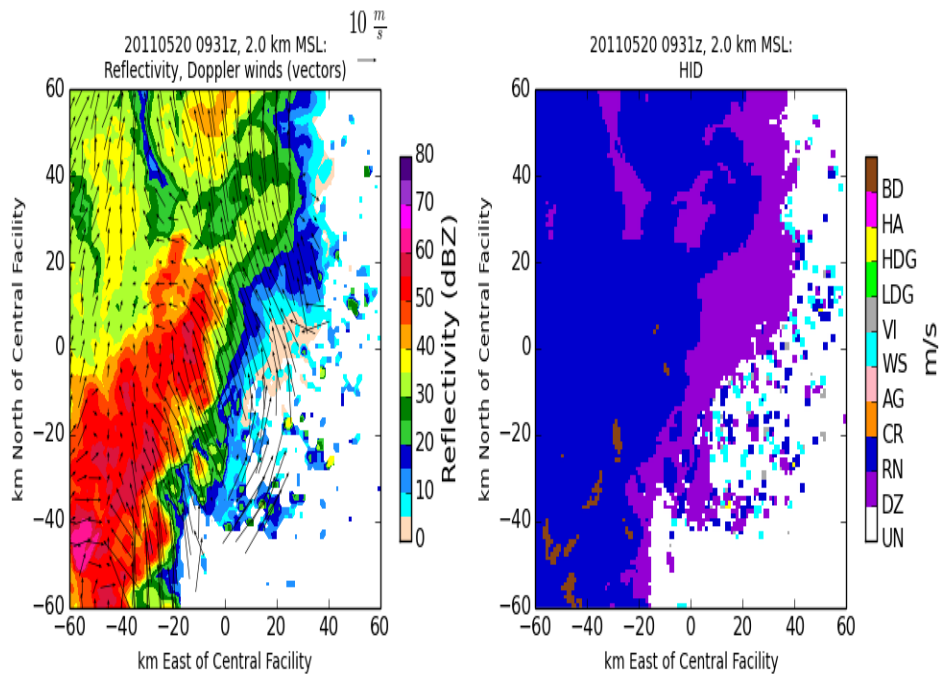


FIGURE 4.28. 2 km constant altitude plot of reflectivity with overlaid wind vectors at 0931 UTC.

4.1.3.1. *Kinematics.* The mean vertical wind was negligible, meaning there was a near equal balance between updraft and downdraft in the multi-Doppler region, as shown in figure

4.29. Updrafts peaked at 2 m s^{-1} at a height of 9 km, while downdrafts peaked at -2 m s^{-1} at a slightly higher height of 9.5 km. Radar echo tops were quite high, reaching 18 km, which is the highest point the radar data is gridded to.

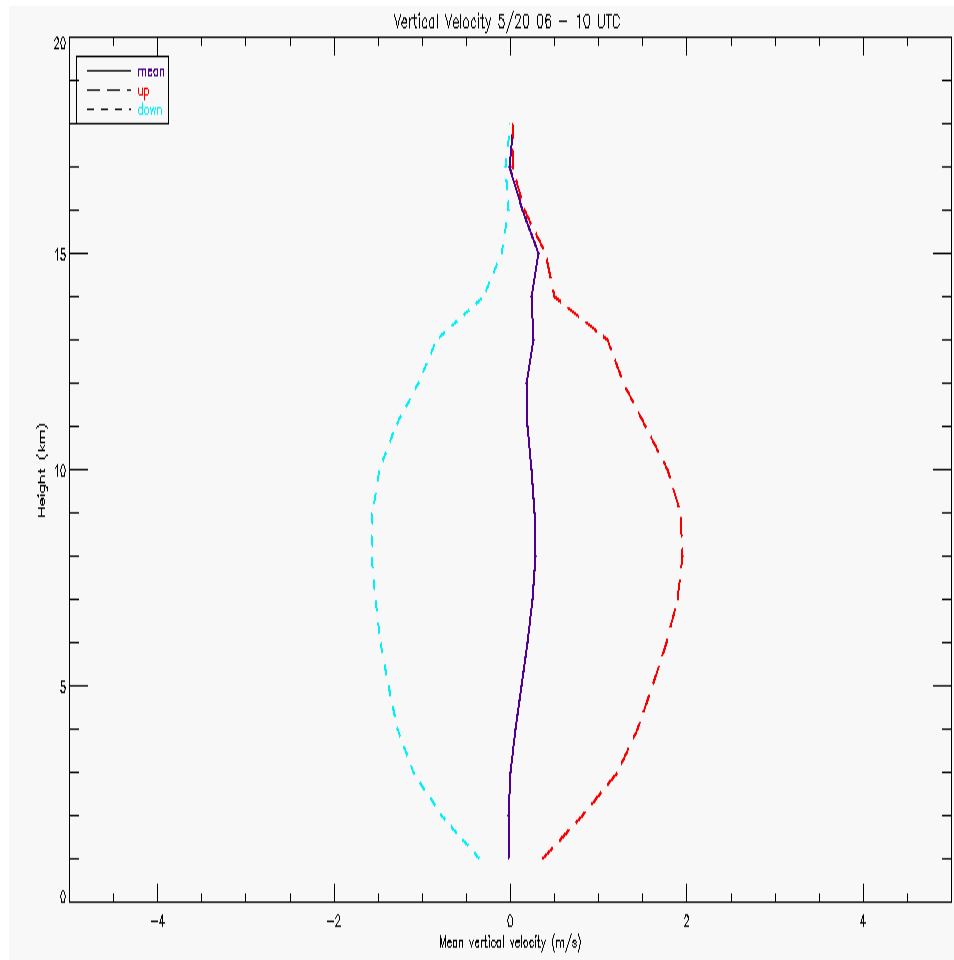


FIGURE 4.29. Mean vertical velocity split by upward and downward motions over the SGP domain and between 6 and 10 UTC.

The maximum updraft winds observed over the entire time period within the domain were 28 m s^{-1} and peaked at a height of 10 km, while the maximum downdraft winds observed were slightly lower, at -24 m s^{-1} and at 9 km in height.

Next, the evolution of the storm kinematics are examined using four example times. This was an interesting case in that the strongest vertical winds occurred at the end of the

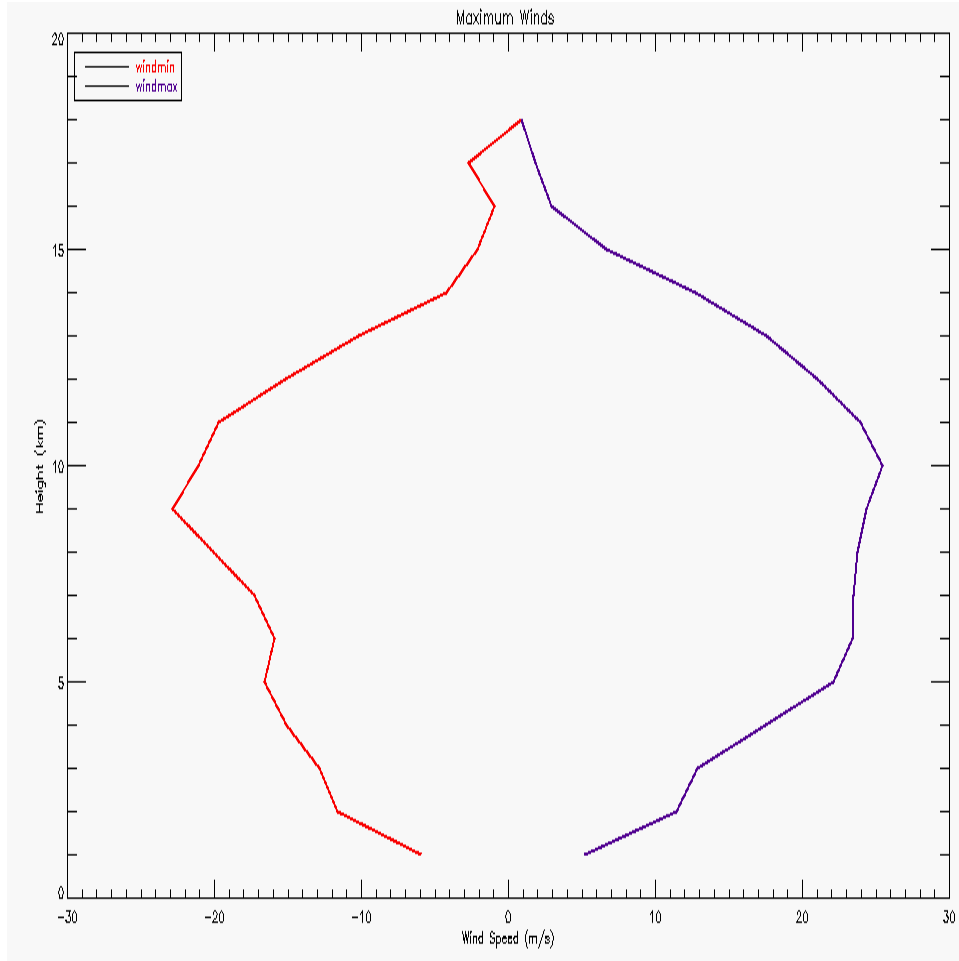


FIGURE 4.30. Maximum and minimum wind at each height over the 6 - 10 UTC time period in the SGP region.

time period while the weakest were observed at the beginning, as is expected as over time the squall line entered the SGP domain. Figure 4.31 shows the mean vertical velocities at each time. Patterns are the weakest at 0635 UTC and are dominated by downward motion, with a peak at the height of the melting layer at approximately 4 km. The strong upward velocity at the top of the cloud is likely erroneous, occurring due to inadequate sampling of the cloud echo top. The next time, 0730 UTC, vertical motions increased in strength and became predominately convective. The third time (0828 UTC) exhibited a downdraft signature below the melting layer and an updraft signature above. This time is taken as

the anvil of the squall line is moving over the region, and is likely the cause of the low level downdraft and mid to upper level updraft. These three times also had equal cloud top heights at 14 km. The final time occurs as the squall line is almost completely within the domain. The cloud top heights are now 17 km, and the winds are dominated by the updraft.

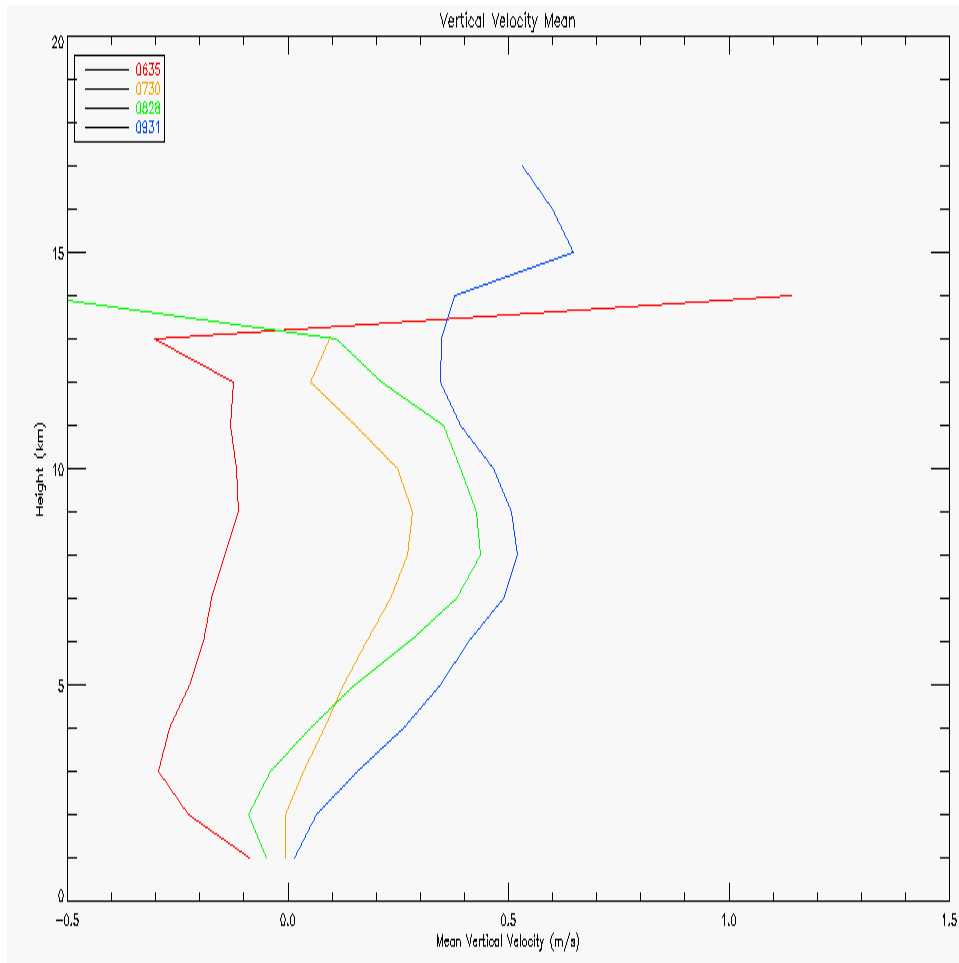


FIGURE 4.31. Mean winds for four selected times (0635, 0730, 0828, 0931 UTC).

Figure 4.32 shows the mean vertical velocity of each time split between upward and downward motions. The first time, 0635 UTC, has a peak of $|1.5| \text{ ms}^{-1}$ at a height of 10 km for both the updraft and downdraft. This increases in magnitude and lowers in height for the next two time steps. At 0730 UTC, peaks of 1.75 ms^{-1} at a height of 8 km for

the updraft occur, while the next time at 0828 UTC has a peak of 2 ms^{-1} at a height of 9 km. The downdraft shape is similar for these three times. The final time has the strongest mean updraft of 3 ms^{-1} with its peak occurring at a height of 7 to 8 km. Its largest mean downdraft is -2 ms^{-1} at a height of 7 km.

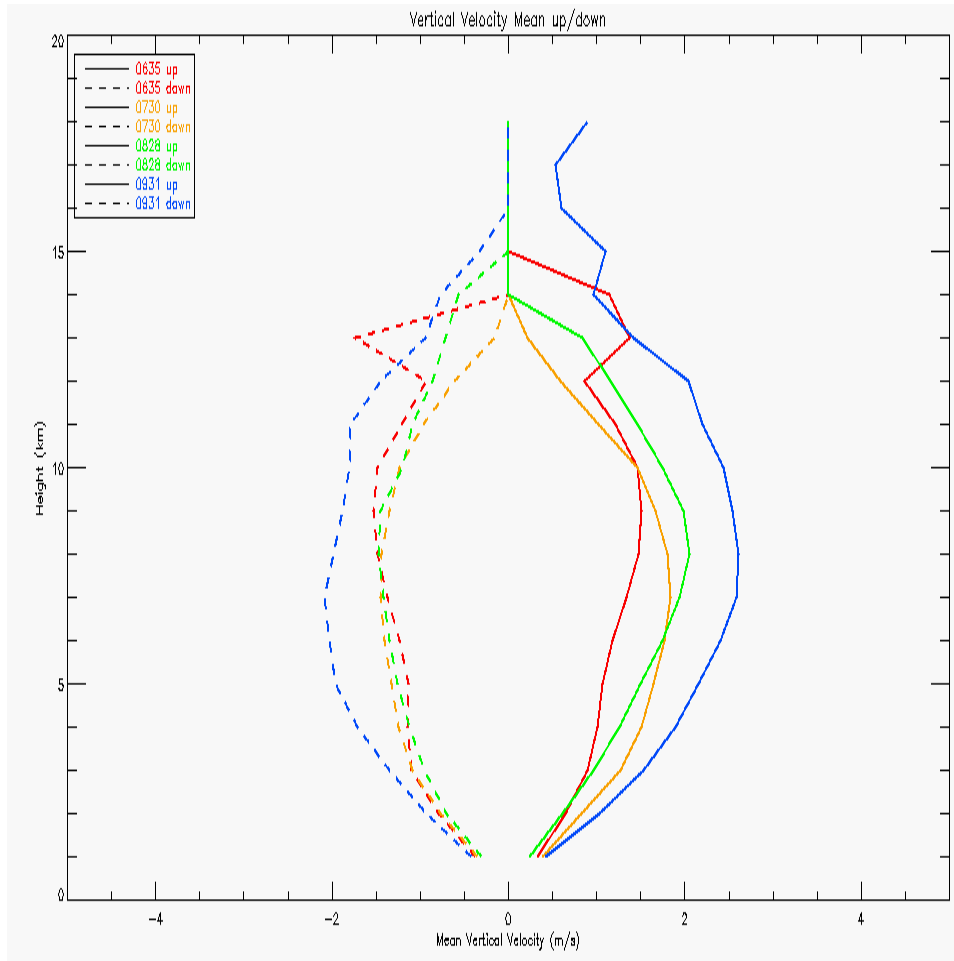


FIGURE 4.32. Mean upward and downward motions for the four selected times (0635, 0730, 0828, 0931).

4.1.3.2. *Microphysics.* The hydrometeor classification frequency as a function of height for each category is shown in figure 4.33. There was very little hail noted for the time period examined, with none of it reaching the surface. Some big drops were noted at the surface, likely from hail melting. There was a relatively small frequency of low and high density

graupel, closer to what was observed during the transition case (01 May) but more stretched through the top of the cloud due to the stronger vertical velocities and higher cloud tops. It is hypothesized that had analyses been feasible during the squall line, a larger amount of hail and big drops would have been seen, as there were severe hail reports on this day, and even more vigorous vertical motion within the squall line.

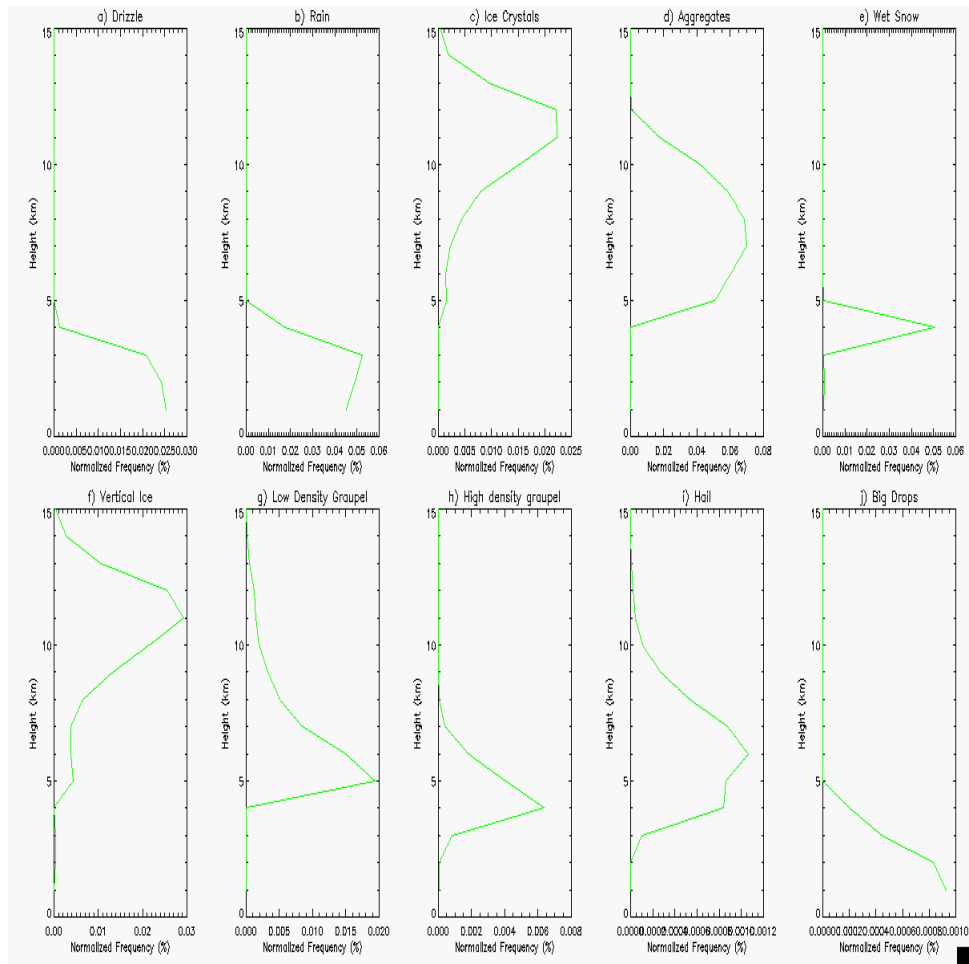


FIGURE 4.33. Frequency of hydrometeor classification for each category for each case.

4.1.4. 23 MAY 2011. This day began as a stationary front hovered just to the northwest of the SGP (figure 4.34). A dry line was situated to the west of the SGP. Temperatures were quite warm, at 28°C with dew points in the 15 to 20°C range.

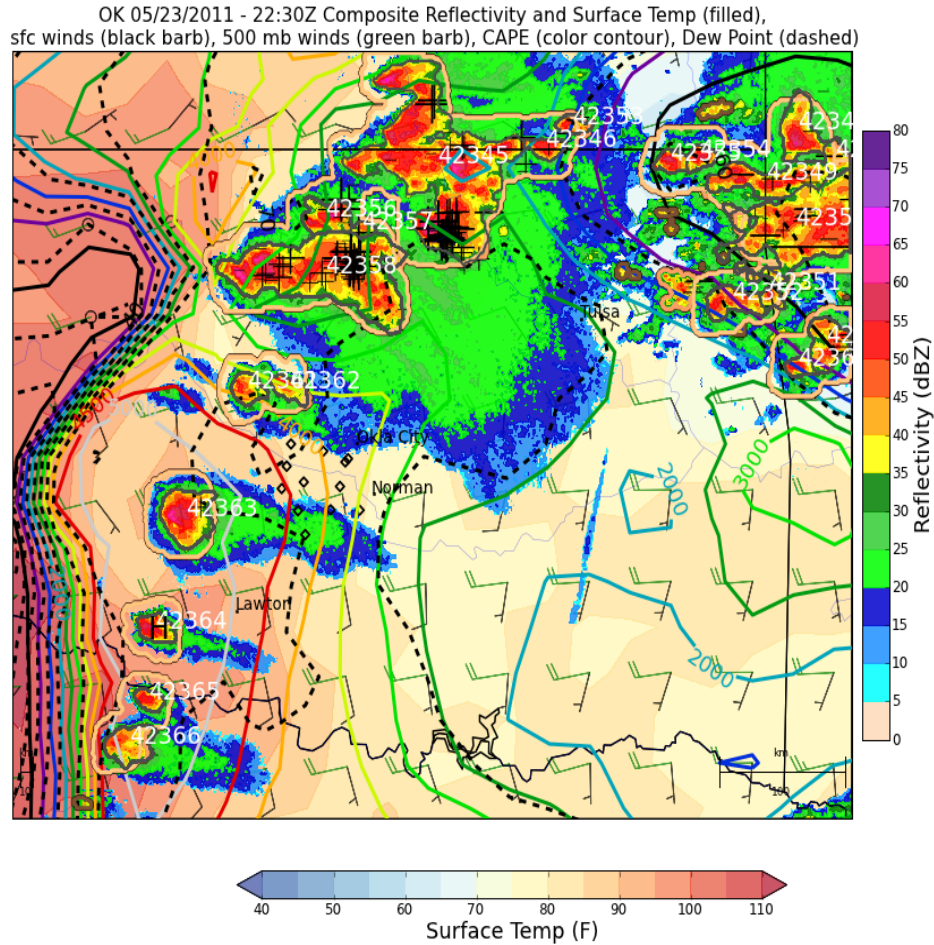


FIGURE 4.35. Surface analysis with overlaid radar from 2230 UTC showing surface temperature (filled), surface winds (black barb), 500 mb winds (green barb), CAPE (color contours), dew points (dashed lines), cell tracking (orange contour). Plot courtesy of Brody Fuchs in the CSU-RADARMET research group.

and moving east towards SGP. The time period chosen for analysis was 21-24 UTC, as this time period enveloped the majority of the storms in the SGP domain. The radars used for this analysis were: XSW, XSE, CSAPR, and KVNK.

Figure 4.37 shows the maximum reflectivity from each radar within the analysis domain used for SGP at 2230 UTC, the same time as shown for all of Oklahoma in 4.35, with overlaid wind vectors. This shows the storm motion and outflow (at $x = -20, y = 15$), as well as convergence in the center of the convective cores (at $x = -10, y = -35$).

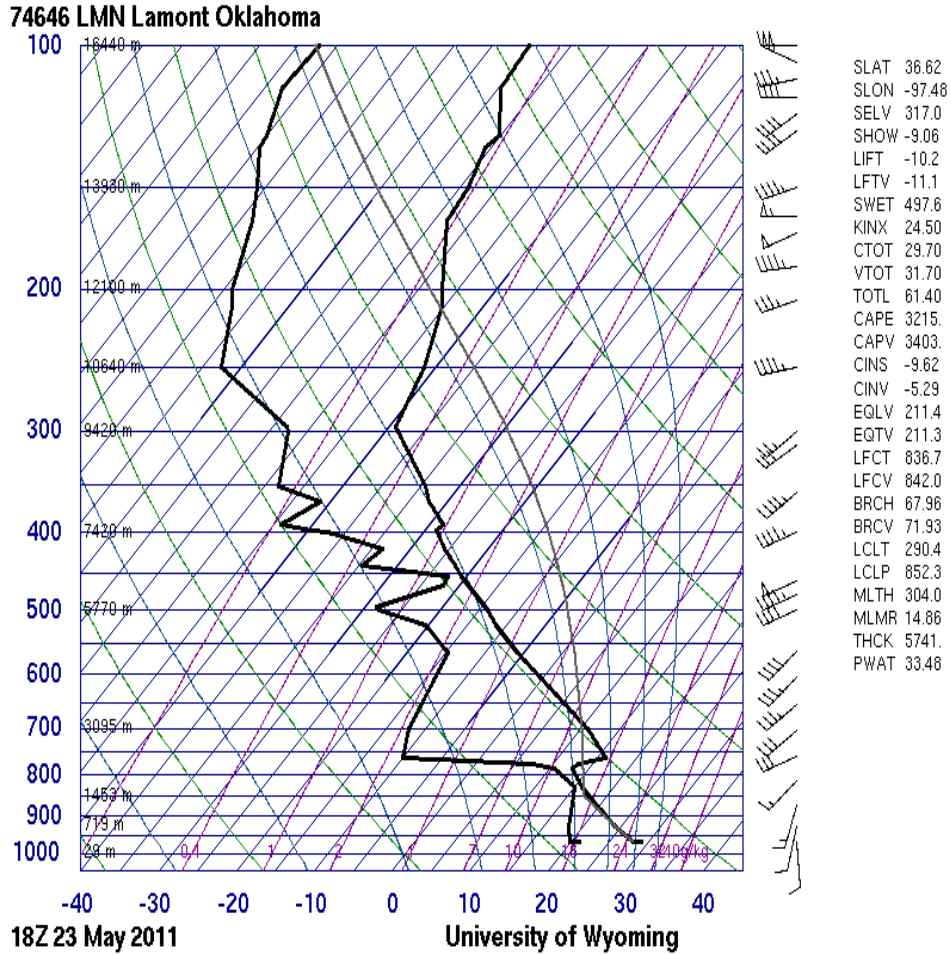


FIGURE 4.36. 18 UTC sounding for Lamont, Oklahoma for the 23 May case.

4.1.4.1. *Kinematics.* This case contained very strong vertical motion in the convective cores, although this does not show up well in the means over the entire analysis period and domain, as not everywhere had strong winds. These strongest winds were limited to the supercellular storms. The mean vertical winds are shown in figure 4.38. The updraft has a peak of 2.5 ms^{-1} at a height of 7 km, while the downdraft has a peak of just under 2 ms^{-1} at a height of 4 km. The overall mean is dominated slightly by the downdraft below the melting layer and by the updraft above the melting layer.

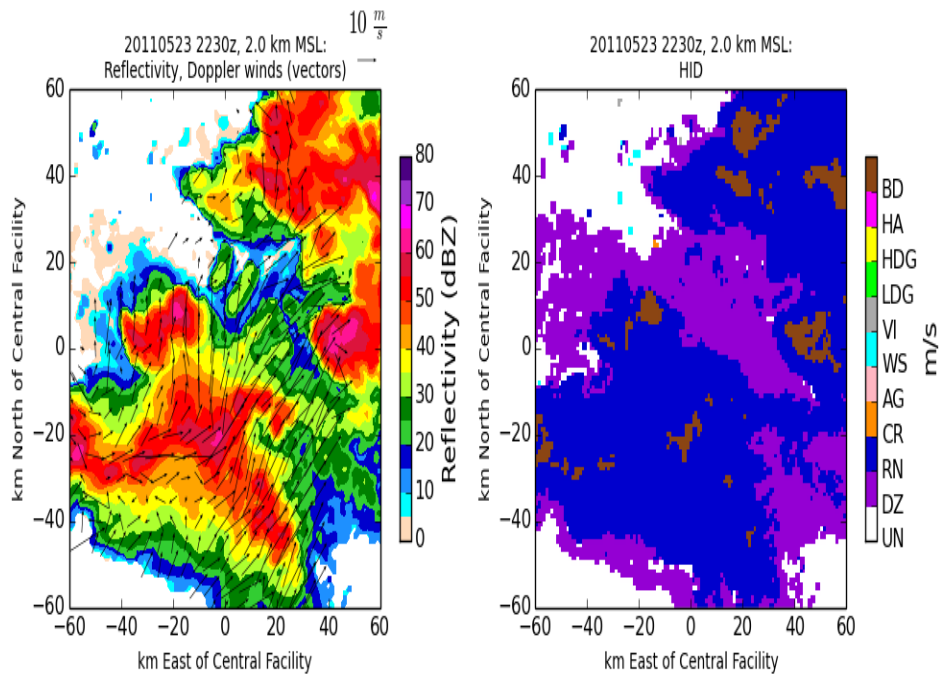


FIGURE 4.37. CAPPI taken at 2 km at 2230 UTC showing reflectivity with overlaying wind vectors.

The maximum and minimum winds in figure 4.39 are quite impressive. The maximum downward winds are relatively consistent throughout the troposphere, with a peak of -20 m s^{-1} at 8 km. The updraft maximum occurs at 9 km, up to 38 m s^{-1} . The updraft is not consistent with height, rather increasing nearly linearly with height to its peak value at 9 km.

Since storms moved so quickly through the SGP region, we chose to examine four different storms. The vertical velocity means of these storm times (2134, 2209, 2237, 2336 UTC) are shown in figure 4.40. The weakest of these storms was the final time analyzed, as storms

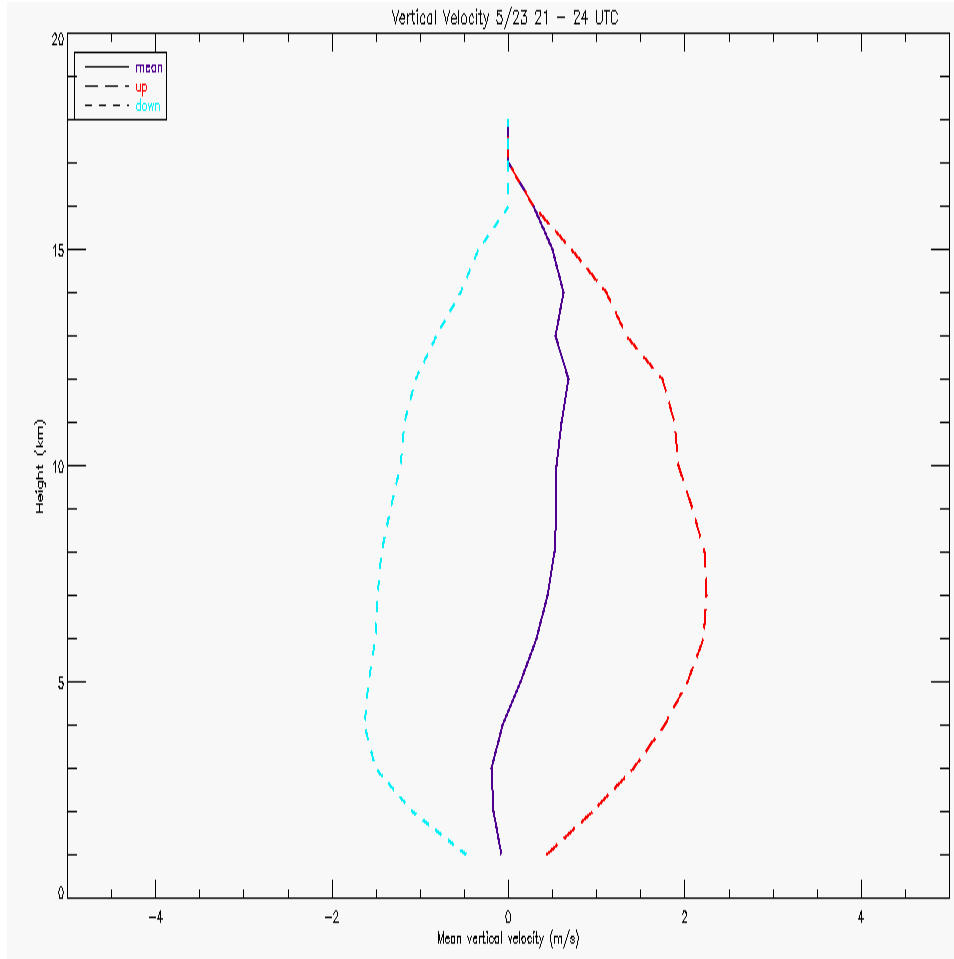


FIGURE 4.38. Mean vertical velocities, also split into upward and downward motions.

were weakening as the dry line weakened. The other three were relatively similar in their mean winds. The time periods of 2237 and 2336 UTC were dominated by downward motions below the melting layer and weak upward motions aloft, while the first two timesteps (2134 and 2209 UTC) were characterized by upward motion.

Differences between each time become more clear when examining the mean vertical velocity split between upward and downward motions, as shown in figure 4.41. The first time (2134 UTC) has a double peak in mean updraft magnitude. The lowest occurs at 6 km and has a peak of 2.5 ms^{-1} . The upper peak reaches 4 ms^{-1} at a height of 12 km. The

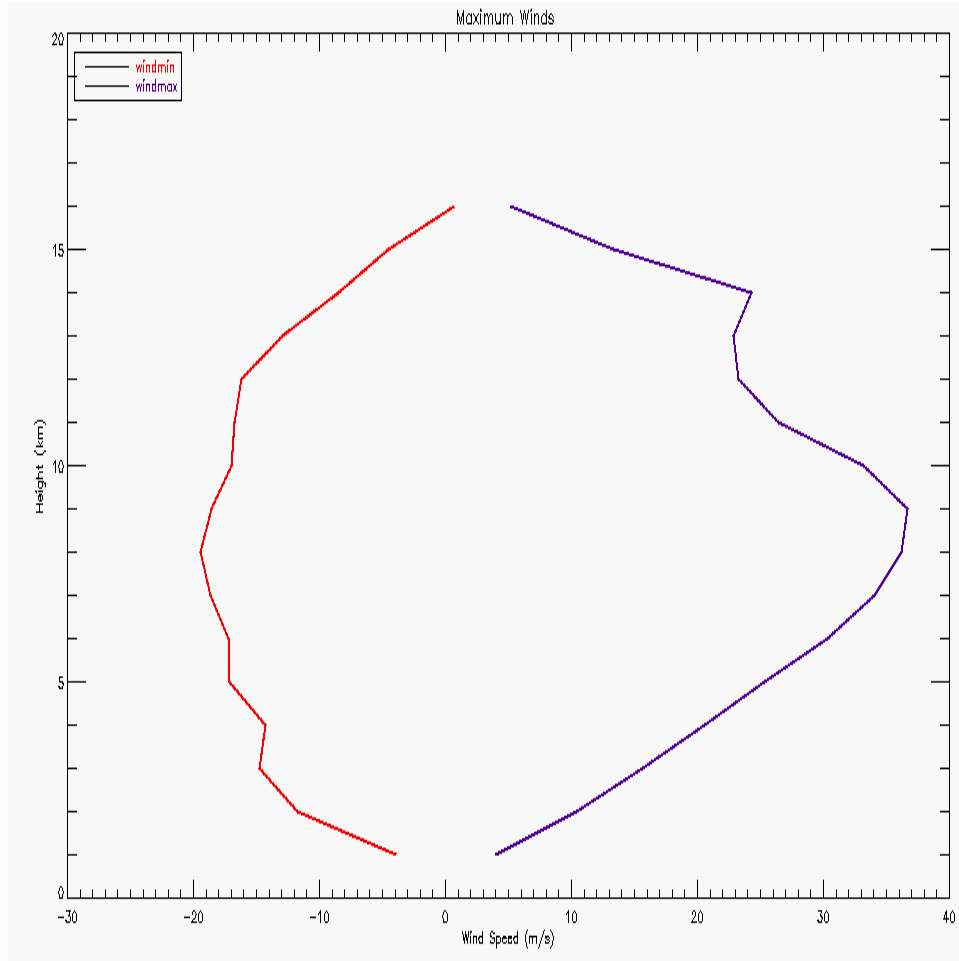


FIGURE 4.39. Minimum and maximum vertical wind velocities.

following time, 2209 UTC, is the strongest in terms of updraft strength overall, peaking at 3.5 m s^{-1} at a height of 7 km. The downdraft approximately balances this, with a peak of -2 m s^{-1} at 5 km. The third time (2237 UTC) has the highest occurring peak, of 2.5 m s^{-1} at heights ranging from 7 to 11 km. The final and weakest time, 2336 UTC, has an updraft maximum mean of 2 m s^{-1} at a height of 9 km.

4.1.4.2. *Microphysics.* Figure 4.42 shows the hydrometeor classification frequency as a function of height for each category. Ice crystals for this case occurred at high altitudes, due to the strong updrafts. Aggregates were also shifted to slightly higher altitudes, along with

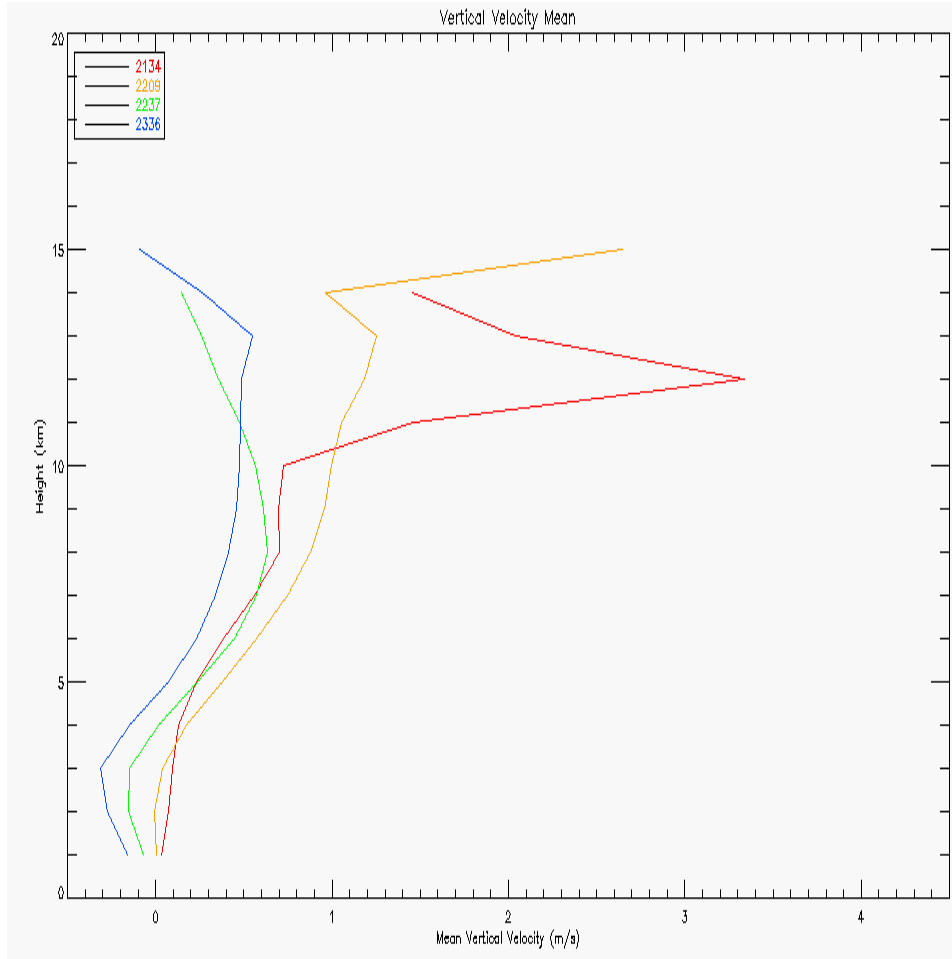


FIGURE 4.40. Mean vertical velocity for four selected time steps (2134, 2209, 2237, 2336 UTC) on 23 May

vertical ice. Vertical ice also occurred in a very large volume due to the high electrification of the storm leading to vertical alignment of ice crystals, with the lightning source density shown in figure 4.43 is taken from the Oklahoma Lightning Mapping Array. High density graupel occurred just above the melting layer, while low density graupel appears frequently above the high density graupel peak. The most interesting aspect of this storm is the large amount of hail aloft and big drops at the surface. There were severe hail reports this day, so the presense of hail at the surface is physically reasonable. The big drops in this case may

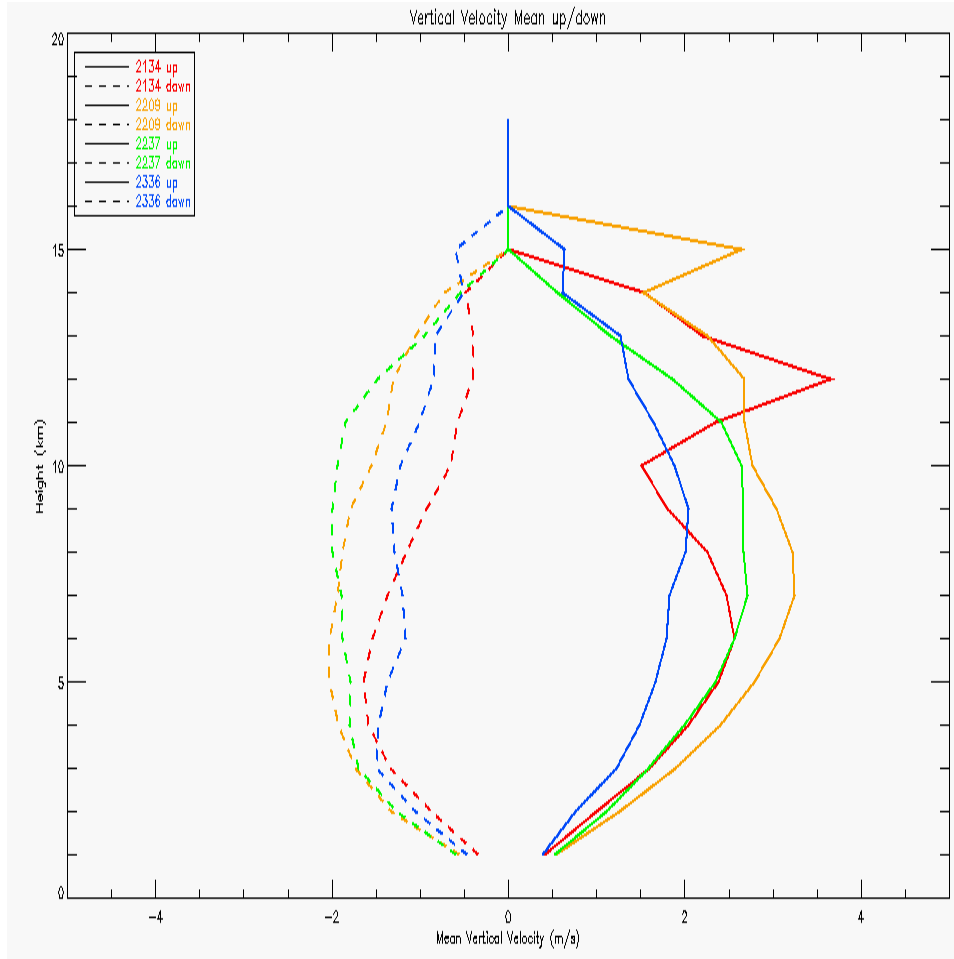


FIGURE 4.41. Mean vertical velocities split into upward and downward components for the four selected times (2134, 2209, 2237, 2336)

have formed through melting hail, or consist of water coated hail as the warm cloud depth was shallow (1.5 km) and the hail may not have had time to fully melt.

4.1.5. 25 FEBRUARY 2013. The final case to be analyzed did not occur during the MC3E field campaign, but two years later during winter, in February of 2013. It is important to analyze as it will show if the analysis method works for all seasons or is best for just summer-type precipitation.

The synoptic setup this day began with a cold front that had become stationary over the North-Central Oklahoma region (figure 4.44). Temperatures were cool ahead of it, at

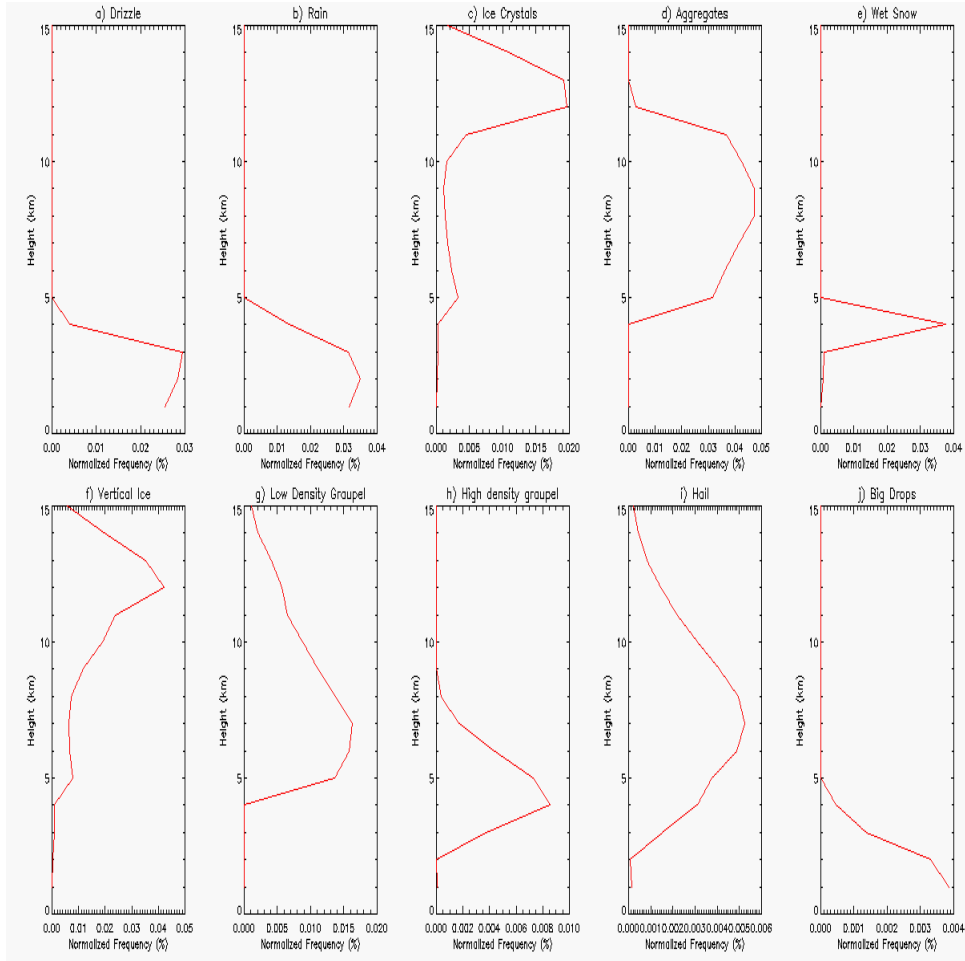


FIGURE 4.42. Frequency of hydrometeor classification for each category for each case. At this time, the red line depicting 23 May 2011 is of interest.

8 ° C with dewpoints of 0 ° C, while behind the front it was slightly cooler and moister, with temperatures of 3 ° C and dewpoints of 2.5 ° C. The SGP site was located right along the stationary front and therefore experienced some mixed precipitation and snow, as was evident from the Community Collaborative Rain, Hail & Snow Network (CoCoRahs), which noted up to five inches of snow occurring on this day, although this did not occur during the analysis period in which the required radars were running.

The LMN sounding taken at 12 UTC (figure 4.45), during an time of active precipitation, was very moist. The LCL was low, at 900 mb, and there was no CAPE. Surface temperatures

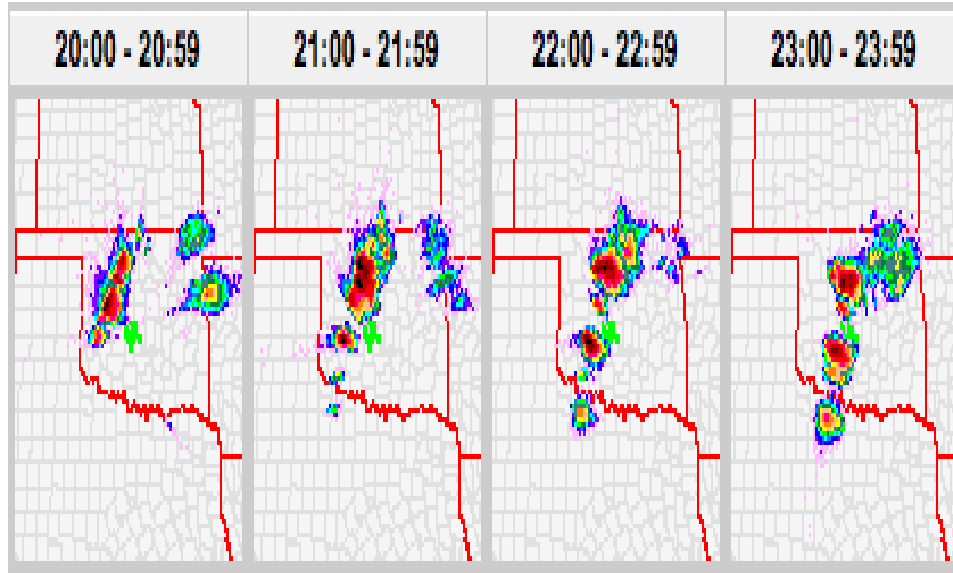


FIGURE 4.43. Lightning source density from the Lightning Mapping Array in Oklahoma.

were just above freezing, but the LCL occurred at the melting level (1.5 km) and the majority of the temperature sounding was below 0 C.

Figure 4.46 shows a constant altitude reflectivity plot taken at 2 km at 0948 UTC showing reflectivity with overlaid wind vectors. Horizontal winds were weak this day, generally remaining below 10 ms^{-1} , while reflectivity was also relatively low, never above 45 dBZ.

For analysis, CSAPR, XSW, and KVNK were used. XSE, which was used in all previous cases, was not operational on this day. The time period analyzed was chosen to be from 06 UTC to 10 UTC.

4.1.5.1. *Kinematics.* Despite being a mixed-precipitation event, mean vertical winds were relatively strong, nearly reaching what was observed in some of the convective case studies previously discussed. Mean winds separated into upward and downward motion are shown in figure 4.47. Mean upward motion peaks slightly lower than the downward motion, at a height of 5 km, versus the 6 km height of the downward motion peak, while the downward

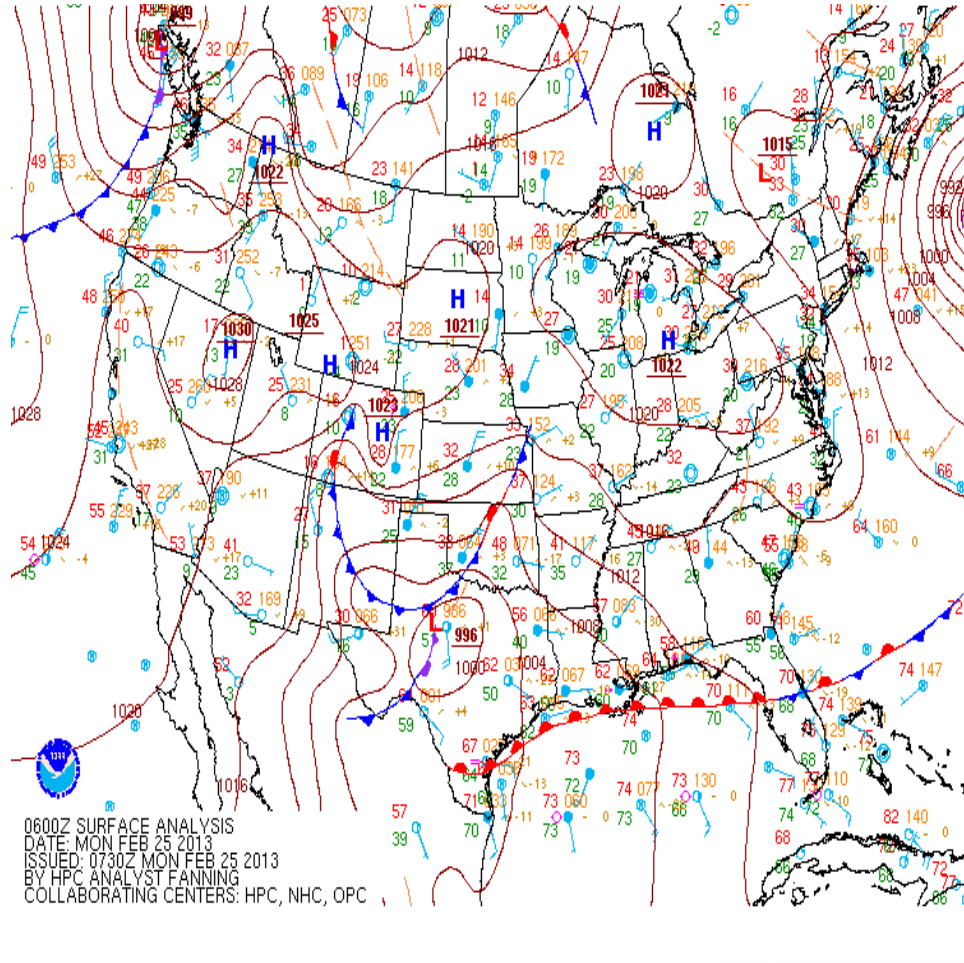


FIGURE 4.44. Surface analysis and frontal positions.

motion dominates in the upper atmosphere. The upward motion peaks at 2 ms^{-1} , while the downdraft peaks at -1.5 ms^{-1} . Cloud tops were shallower than the typical spring convection cases, at just 11 km, but taller than the spring transitional case of 01 May.

The maximum vertical winds observed are shown in figure 4.48. The maximum updraft occurred at 17 ms^{-1} at a height of 6 km, while the maximum downdraft occurred at -14 ms^{-1} at a height of 5 km, during a more convectively driven time as the storm transitioned from snow to rain.

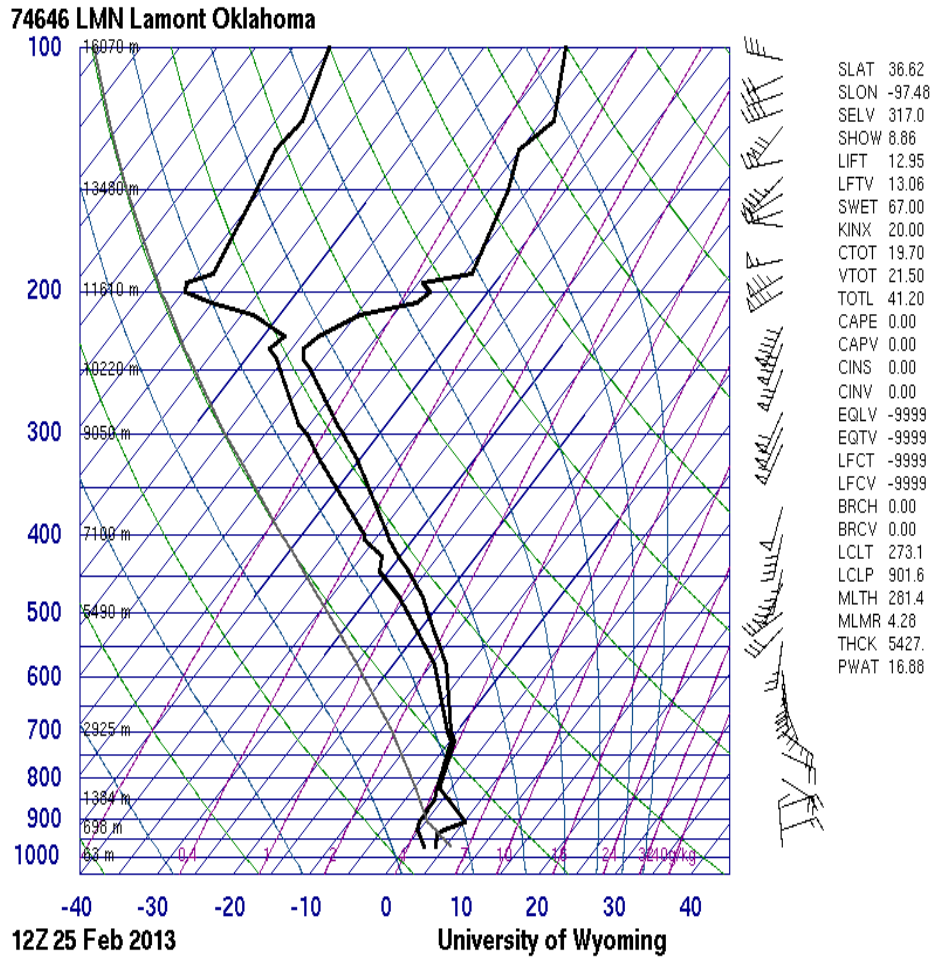


FIGURE 4.45. 12 UTC sounding for Lamont, Oklahoma.

The four times chosen for further analysis were: 0705, 0811, 0909, and 0940 UTC. The mean vertical velocities for these times can be seen in figure 4.49. All of the times chosen were dominated by upward motion throughout, with the strongest mean vertical winds occurring at 0909 UTC.

The vertical velocity means were then separated into their upward and downward components, as shown in figure 4.50. The final time of 0940 UTC time is the weakest, but all times are quite similar in shape and magnitude. 0909 UTC had slightly weaker winds than 0705

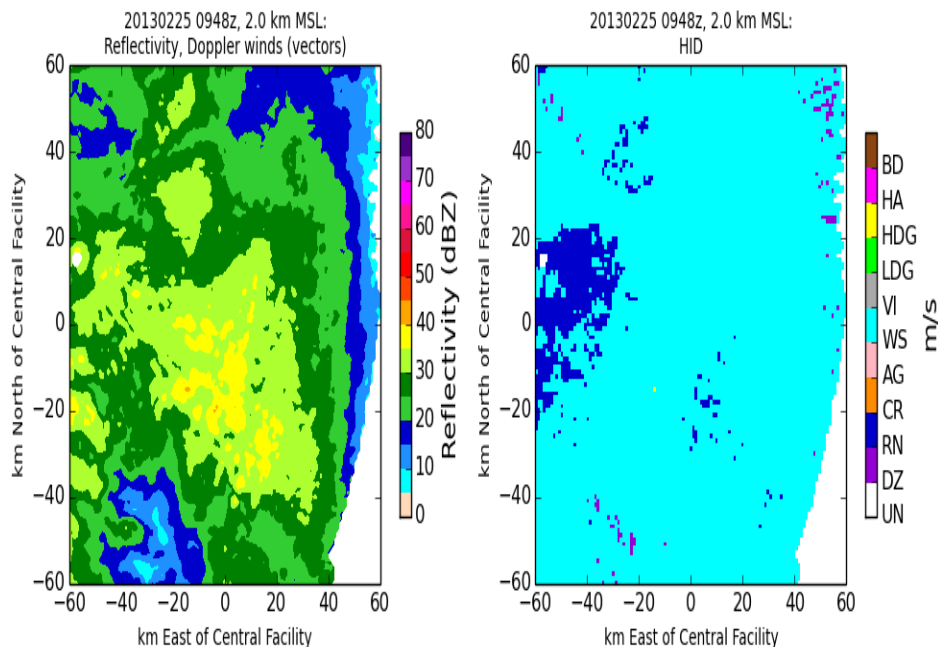


FIGURE 4.46. 2 km cappi showing reflectivity with overlying wind vectors at 0948 UTC.

and 0811 UTC, but had taller echo top heights at 15 km. This is likely a more convectively driven time than the other times analyzed in this way.

4.1.5.2. *Microphysics*. When examining the microphysics, we used the same HID classification algorithm used previously, as this was a transitional case with strong winds and had the potential to support more spring convection type particles.

Figure 4.51 shows the frequency of each hydrometeor category at each height. Below the low melting layer, mostly rain and drizzle are present. A small amount of hail, high density graupel, and ice crystals are noted at the surface level. These are likely misclassified snow

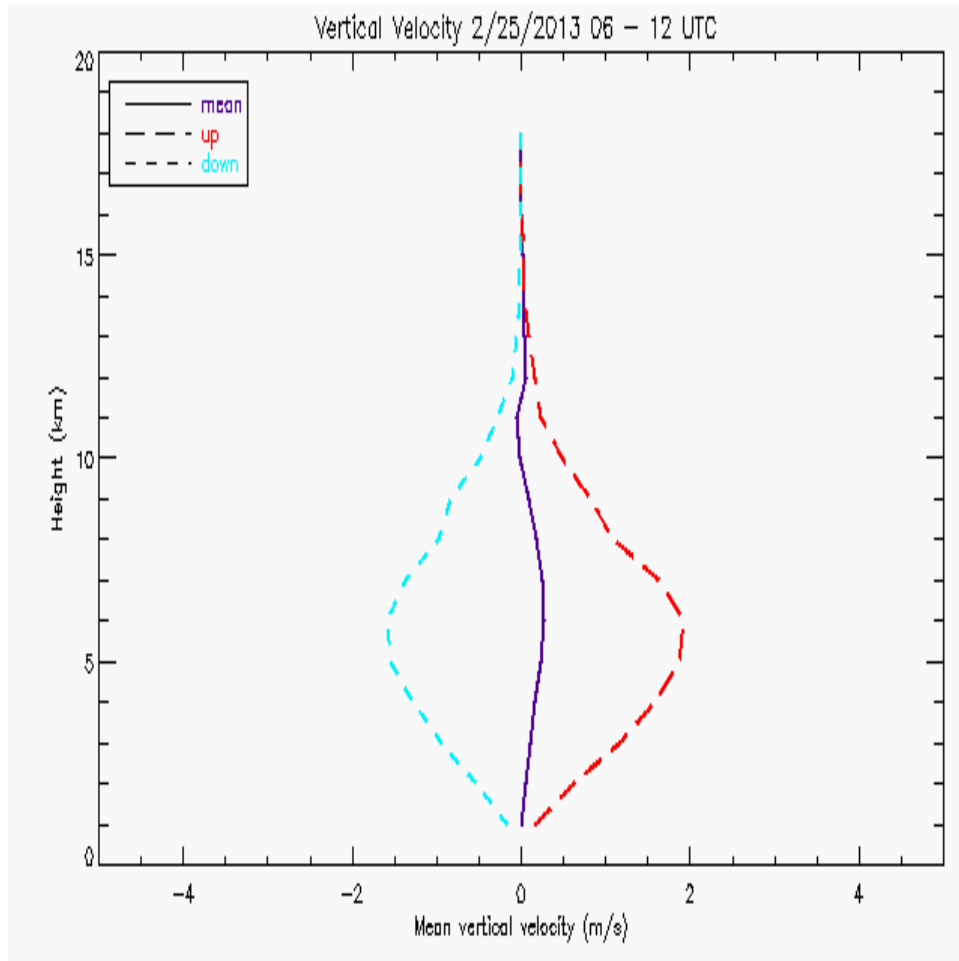


FIGURE 4.47. Mean vertical velocities split into upward and downward motion over the entire analysis time period and domain.

type particles that may occur in a cold transitional season storm. Above the melting layer, small ice particles such as ice crystals, aggregates, and vertical ice dominate.

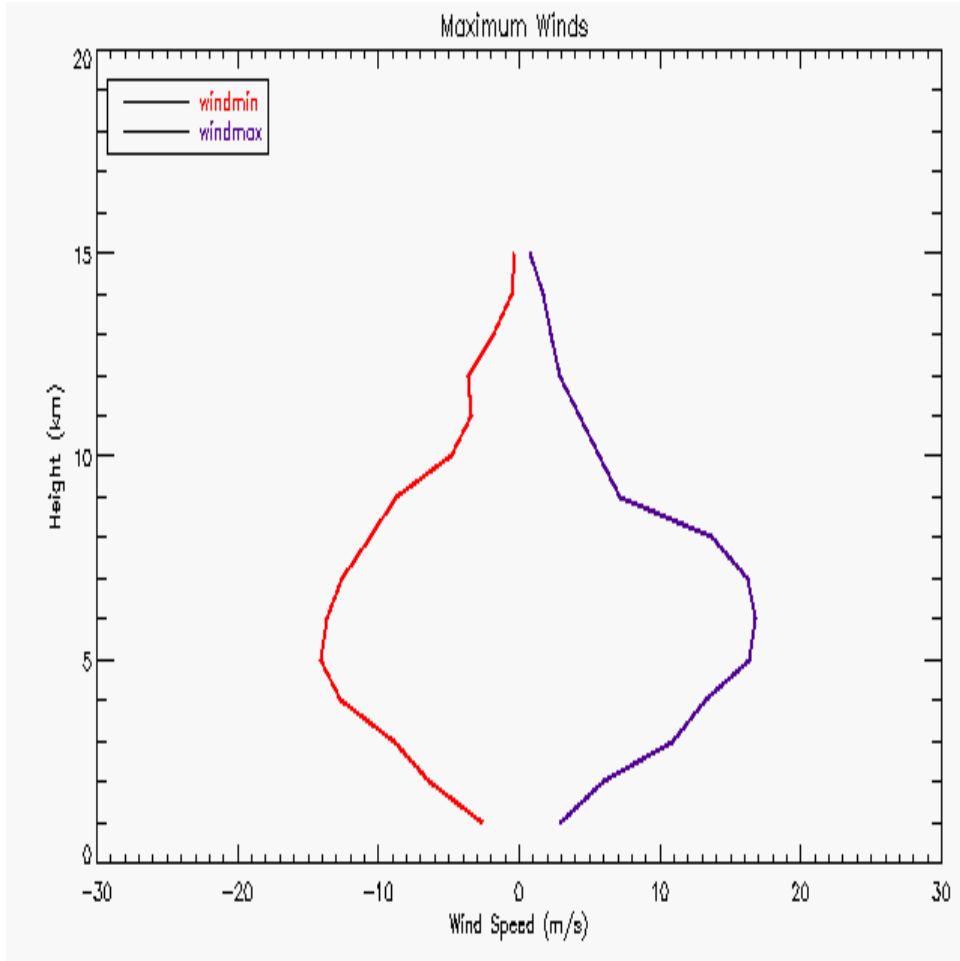


FIGURE 4.48. Maximum and minimum vertical wind speeds over the entire analysis time period and domain.

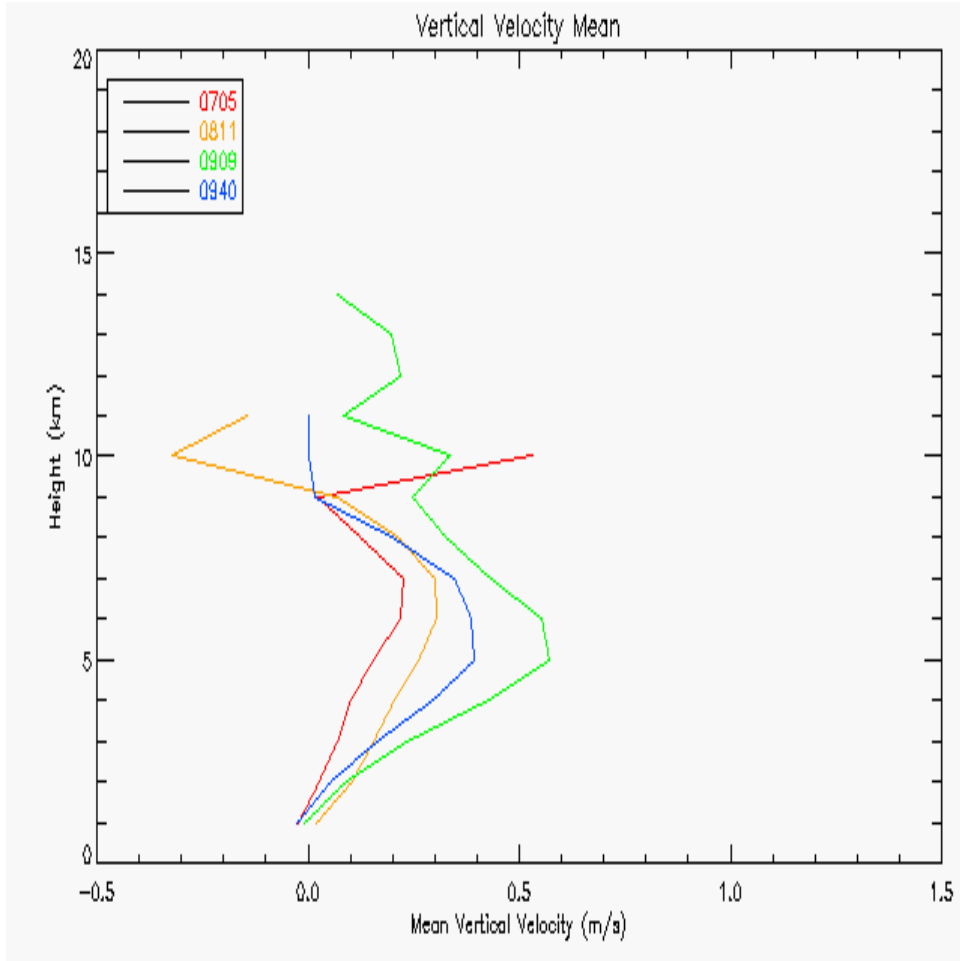


FIGURE 4.49. Mean vertical velocities for 0705, 0811, 0909, and 0940 UTC.

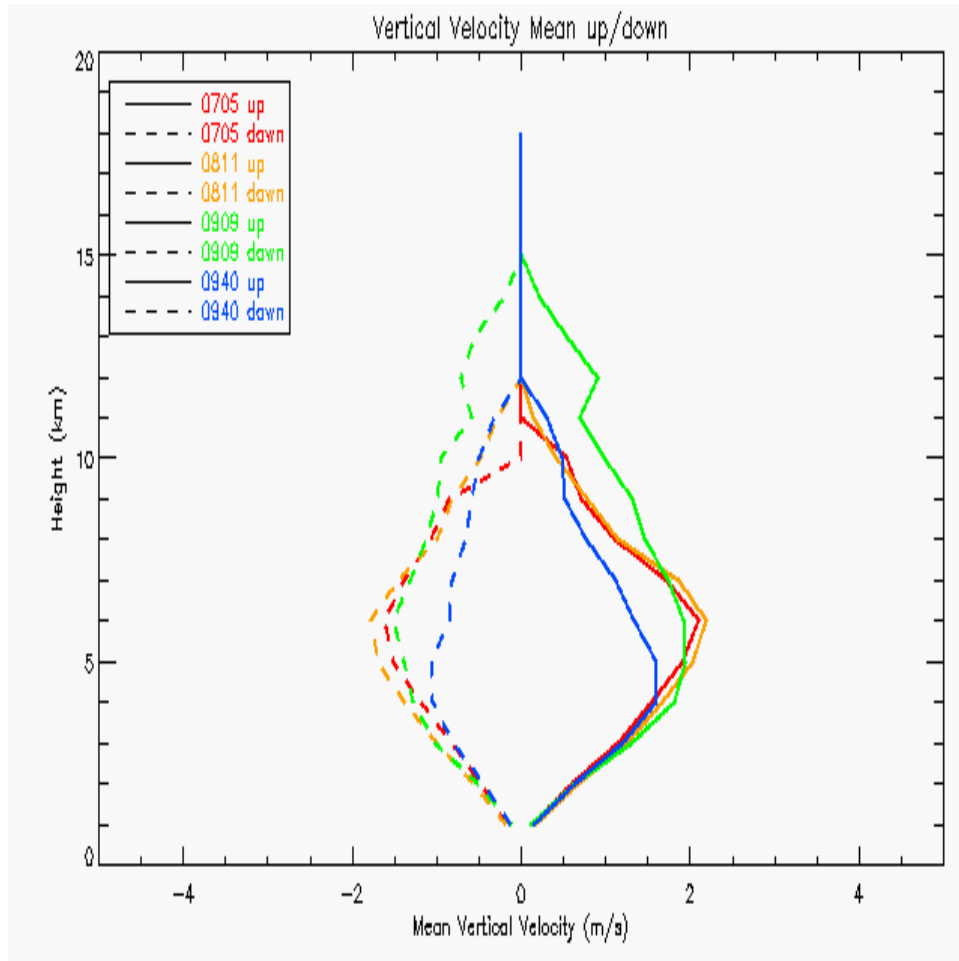


FIGURE 4.50. Mean vertical velocities split into upward and downward motions for 0705, 0811, 0909, and 0940 UTC.

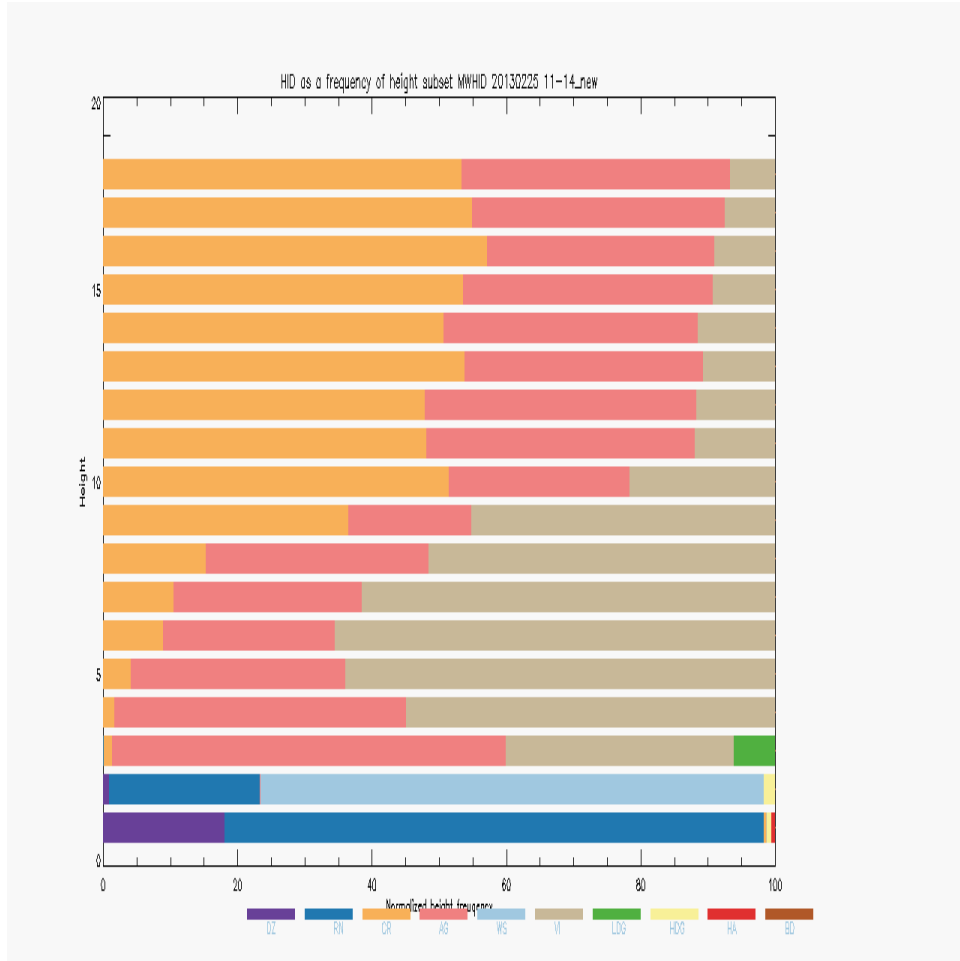


FIGURE 4.51. Normalized height frequency of hydrometeor category for the 25 February case.

CHAPTER 5

CONCLUSION

In this research, the kinematic and microphysical structures of multiple types of precipitating events were analyzed using various datasets from the ARM-SGP site in North-Central Oklahoma. The large number of instruments present during the Midlatitude Continental Convective Clouds Campaign (MC3E) and provided by the ARM organization as permanent installments allowed for multi-Doppler analysis using three to four radars, as well as a multi-wavelength hydrometeor classification. The presence of the S-band profiler allowed for validation of the multi-Doppler radar derived vertical winds to within 1 ms^{-1} , and showed that the downward motions may be undersampled by the radar derived method possibly due to the difficulty the multi-Doppler method has in detecting low level divergence (Nelson and Brown, 1987) due to the radar sampling missing the low levels of the atmosphere. A method was also developed to allow analysis of multiple cases using the same methodology. Analysis of a more wintery transitional precipitation event showed that the HID method used in convective cases is applicable to transitional cases, although may misclassify ice particles below the melting layer.

The consistent methodology applied to several cases that occurred during MC3E allows for a unique opportunity to compare the different cases that occurred within a month of each other. The first case discussed, 25 April 2011, consisted of organized elevated thunderstorms. The 1 May case exhibited characteristics of an early spring transitional event. The 20 May case analyzed was for storms forming ahead of a squall line, as well as the beginning of the same squall line entering the SGP area. Finally, the 23 May case contained strong

thunderstorms, some of which were supercellular. This would help modelers improve their models through comparison as a wide range of storm types were observed and analyzed with similar methodology.

The kinematics of each of these cases differed wildly. Figure 5.1 shows the mean upward and downward motions for each case over the entire domain and time period of each case. The winds are limited to only where the radars topped the storms, requiring a minimum of 20 dBZ at the top of the storm in order for it to count as topped. This 20 dBZ threshold was chosen to ensure the storms were completely topped and that no effects due to errors in meeting the upper boundary conditions of the multi-Doppler wind retrieval were included (Dolan and Rutledge (2010)). The 23 May case had the strongest winds and the tallest storms, while the 1 May case had the weakest winds and storms with the least vertical development. When examining these updrafts, the 23 May case mean vertical winds peaked at 3 ms^{-1} at 6 km and stayed fairly consistently at approximately 3 km up to the top of the storm. The 25 April case exhibited a more curved updraft profile, with a peak of 2.5 ms^{-1} at 7 km. The 20 May case had the highest occurring peak at a height of 10 km, but had weaker updrafts at 2 ms^{-1} . The 1 May case updraft peaked at 1 ms^{-1} at 3 km. The downdraft curves (dashed) are also quite different. The 23 May storm downdraft mean peaked low in height, at 3 to 4 km, which was the melting layer height for this case, and had a speed of nearly -2 ms^{-1} , the strongest seen of all the cases analyzed. The 20 May case had the second strongest downdrafts and the highest peak in mean downward motion, of -1.5 ms^{-1} at a height of 10 km. This case also has the most equally matched updraft and downdraft regions, meaning that the storms were mostly mature storms and entering the beginning

dissipation stages. The 25 April case had consistent mean downward motion of -1.25 m s^{-1} peaking at 3 to 4 km and slowly weakening with height. Once again, the 1 May case is shown to be more closely related to stratiform or winter precipitation, as its downdraft is stronger than its updraft at the surface, at just over 1 m s^{-1} peaking at 3 km in height.

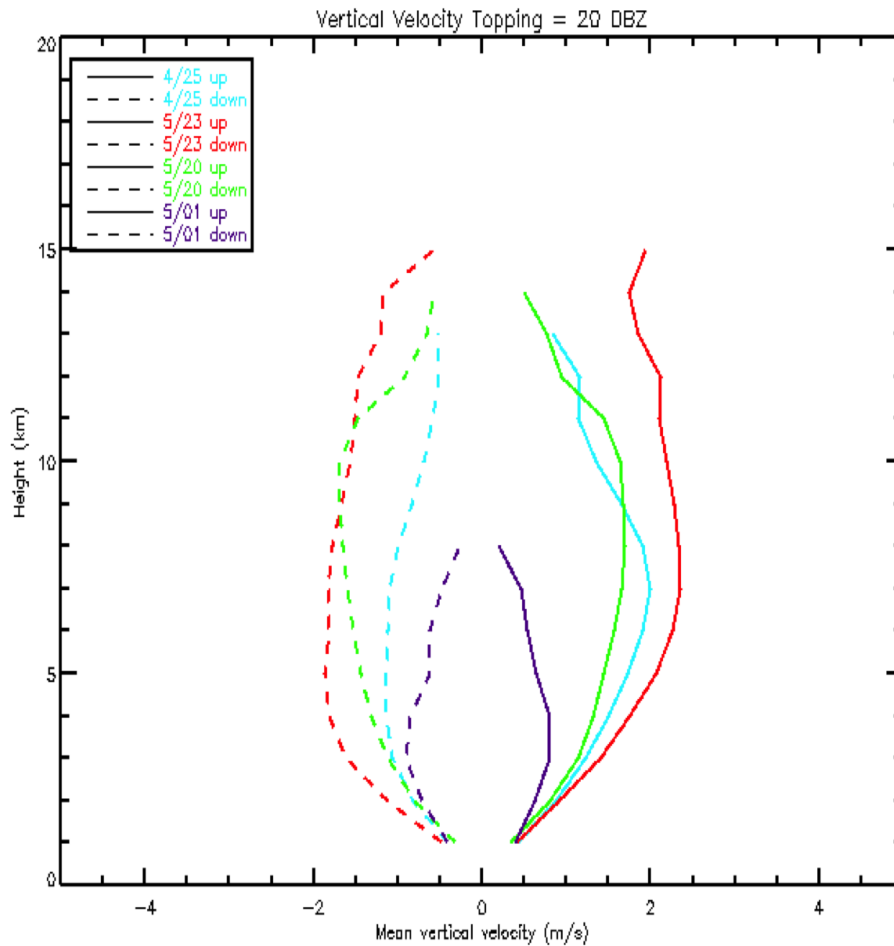


FIGURE 5.1. Multi-Doppler vertical wind means split into upward and downward motion for storms in which the radar topped up to at least 20 dBZ for all cases examined during MC3E.

The hydrometeor classifications of each storm are also different, as shown in figure 5.2. The 23 May case has the largest volume of hail, which is logical as it also had the strongest updraft and is able to support the development and growth of hail stones. It also had the

most vertical ice aloft, likely due to the large electrification of the storm seen in the previous chapter. This case also had the highest occurring peak in high density graupel (4 km) and low density graupel (5 km) owing to the presence of the strongest vertical winds. The 20 May case had the same melting layer height, but its weaker vertical winds were apparently unable to support the formation of the high density or low density graupel as well ahead of the squall line. A significantly lower hail frequency was also noted, although this was likely due to being unable to conduct observations during the intense squall line phase. Both 23 May and 25 April have a high frequency of big drop occurrence. One possible formation mechanism for this is melting hail. This is likely the situation for both cases, as both had deep warm cloud depths for a surface lifted parcel. This would give plenty of time for the hail to melt into large drops as it fell through this warm layer. In all cases, there was a peak in high density graupel at or slightly above the melting layer. Low density graupel did not peak for any case until after this peak in high density graupel had occurred and begun decreasing.

Comparisons were done for the 25 April case between radar observations and simulations from the WRF-SBM model. Both model and radar observations show reasonable agreement for kinematic and microphysical characteristics of the storm. Both showed a peak updraft occurring at 7 km in height, and a maximum reflectivity generally below 60 dBZ. However, the model simulations showed stronger updraft maximums, higher reflectivities, and higher echo tops, implying that the simulated convection was too strong for the weakly forced case. The model and radar observations both exhibited weaker downdrafts generally remaining below -10 ms^{-1} in both deep and shallow regimes, although the radar did show stronger

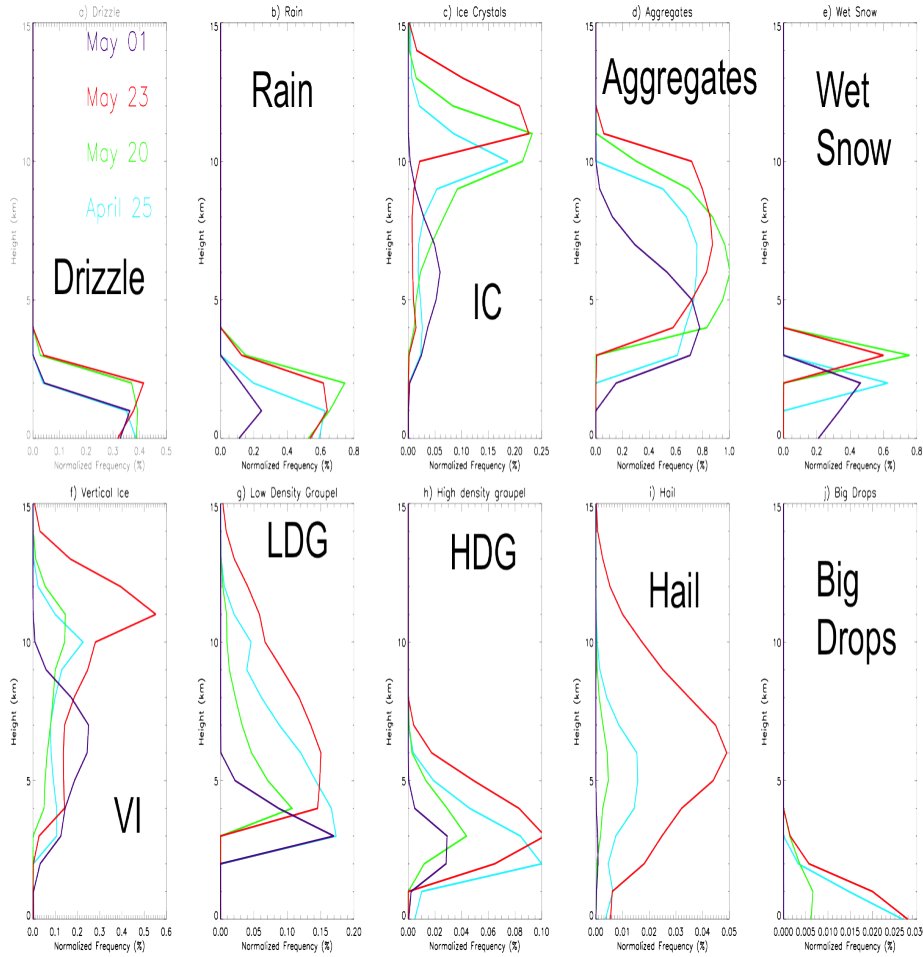


FIGURE 5.2. Frequency of classification for each hydrometeor category for each case examined during MC3E.

downdrafts than the model. Examinations of the microphysical characteristics of the model and radar observations revealed that the model classifies more graupel and snow aggregates above 10 km, while the radar observations indicated mostly ice crystals in this region. The model underestimated drizzle below the melting layer in shallow regimes, but in general the model and radar observations agreed above the melting layer in areas of shallow convection. These differences likely occurred due to the overlapping of several categories, such as low and high density graupel, and small low density graupel vs aggregates.

The winter transitional precipitation case analyzed had weaker winds than most of the convective spring cases, but stronger than the late spring transitional case of 1 May 2011. It also had a low melting level with rain and ice particles below it and aggregates, ice crystals, and vertical ice above. Modifications will need to be done to the methodology in order to improve hydrometeor classifications for ice particles below the melting layer, which would allow for further analysis of winter precipitation events using the radar network.

5.1. FUTURE WORK

The ARM-SGP facility offers an abundance of instruments, from scanning and profiling radars to disdrometers, that would be useful for more detailed analysis of future storms in the region. Oklahoma provides a chance to observe both strong storms in late spring, pyrocumulus in summer from large wildfires, and transitional precipitation or snow in winter. In the long term, the methodology developed in this research could be applied to all three years of data, as well as all future cases that may occur. This would provide an idea of the climatological changes occurring in the region, as well as the characterization of the general climatology of precipitation and storms in the region from a kinematic and microphysical perspective. The many wavelengths of precipitation radars present are ideal for achieving the best hydrometeor classification available, as was shown in the multi-wavelength hydrometeor identification algorithm based on Dolan et al. (2014). The presence of so many radars also allows for an over-analyzed multi-Doppler wind retrieval over the region as well as comparison to a profiling radar for validation.

All of the above mentioned benefits of the ample measurements available could provide a better insight into the processes present in a wide variety of precipitation and clouds. These

measurements could then be compared to more model simulations to improve the model analysis. A suggested future research would be to create a polarimetric radar emulator, as this would be able to simulate polarimetric data based on cloud model outputs (such as done by Ryzhkov et al. (2011)) that could then be run through the hydrometeor classification algorithm for precipitation radars for a more direct comparison to radar based observational analyses.

BIBLIOGRAPHY

- Baldini, L., E. Gorgucci, V. Chandrasekar, and W. Petersen, 2005: Implementations of csu hydrometeor classification scheme for c-band polarimetric radars. *Preprints, 32nd Conf. on Radar Meteorology, Albuquerque, NM, Amer. Meteor. Soc., P11R*, Vol. 4.
- Beard, K. V. and C. Chuang, 1987: A new model for the equilibrium shape of raindrops. *Journal of the Atmospheric sciences*, **44 (11)**, 1509–1524.
- Bringi, V. and V. Chandrasekar, 2001: *Polarimetric Doppler weather radar: principles and applications*. Cambridge University Press.
- Collis, S., A. Protat, P. T. May, and C. Williams, 2013: Statistics of storm updraft velocities from twp-ice including verification with profiling measurements. *Journal of Applied Meteorology and Climatology*, **52 (8)**, 1909–1922.
- Dolan, B. and S. A. Rutledge, 2009: A theory-based hydrometeor identification algorithm for x-band polarimetric radars. *Journal of Atmospheric and Oceanic Technology*, **26 (10)**, 2071–2088.
- Dolan, B. and S. A. Rutledge, 2010: Using casa ip1 to diagnose kinematic and micro-physical interactions in a convective storm. *Monthly Weather Review*, **138 (5)**, 1613–1634.

- Dolan, B., S. A. Rutledge, S. Lim, V. Chandrasekar, and M. Thurai, 2013: A robust c-band hydrometeor identification algorithm and application to a long-term polarimetric radar dataset. *Journal of Applied Meteorology and Climatology*, **52** (9), 2162–2186.
- Fawbush, E. J. and R. C. Miller, 1954: The types of air masses in which north american tornadoes form. *Bull. Amer. Meteor. Soc.*, **35** (4), 154–165.
- Fujiyoshi, Y., N. Yoshimoto, and T. Takeda, 1998: A dual-doppler radar study of longitudinal-mode snowbands. part i: A three-dimensional kinematic structure of meso- γ -scale convective cloud systems within a longitudinal-mode snowband. *Monthly weather review*, **126** (1), 72–91.
- Giangrande, S. E., S. Collis, J. Straka, A. Protat, C. Williams, and S. Krueger, 2013: A summary of convective-core vertical velocity properties using arm uhf wind profilers in oklahoma. *Journal of Applied Meteorology and Climatology*, **52** (10), 2278–2295.
- Gorgucci, E., V. Chandrasekar, and L. Baldini, 2006: Correction of x-band radar observation for propagation effects based on the self-consistency principle. *Journal of Atmospheric and Oceanic Technology*, **23** (12), 1668–1681.
- Heistermann, M., et al., 2014: The emergence of open source software for the weather radar community. *Bulletin of the American Meteorological Society*.

- Herzogh, P. H. and A. R. Jameson, 1992: Observing precipitation through dual-polarization radar measurements. *Bulletin of the American Meteorological Society*, **73** (9), 1365–1374.
- Hubbert, J. and V. Bringi, 1995: An iterative filtering technique for the analysis of copolar differential phase and dual-frequency radar measurements. *Journal of Atmospheric and Oceanic Technology*, **12** (3), 643–648.
- Iguchi, T., T. Matsui, A. Tokay, P. Kollias, and W.-K. Tao, 2012a: Two distinct modes in one-day rainfall event during mc3e field campaign: Analyses of disdrometer observations and wrf-sbm simulation. *Geophysical Research Letters*, **39** (24).
- Iguchi, T., et al., 2012b: Numerical analysis using wrf-sbm for the cloud microphysical structures in the c3vp field campaign: Impacts of supercooled droplets and resultant riming on snow microphysics. *Journal of Geophysical Research: Atmospheres* (1984–2012), **117** (D23).
- James, C. N. and R. A. Houze Jr, 2001: A real-time four-dimensional doppler dealiasing scheme. *Journal of Atmospheric and Oceanic Technology*, **18** (10), 1674–1683.
- Kessinger, C. J., P. S. Ray, and C. E. Hane, 1987: The oklahoma squall line of 19 may 1977. part i: A multiple doppler analysis of convective and stratiform structure. *Journal of the*

atmospheric sciences, **44 (19)**, 2840–2865.

Khain, A., D. Rosenfeld, A. Pokrovsky, U. Blahak, and A. Ryzhkov, 2011: The role of ccn in precipitation and hail in a mid-latitude storm as seen in simulations using a spectral (bin) microphysics model in a 2d dynamic frame. *Atmospheric Research*, **99 (1)**, 129–146.

Khain, A. and I. Sednev, 1995: Simulation of hydrometeor size spectra evolution by water-water, ice-water and ice-ice interactions. *Atmospheric research*, **36 (1)**, 107–138.

Lim, S. and V. Chandrasekar, 2006: A dual-polarization rain profiling algorithm. *Geoscience and Remote Sensing*, **44 (4)**, 1011–1021.

Liu, H. and V. Chandrasekar, 2000: Classification of hydrometeors based on polarimetric radar measurements: Development of fuzzy logic and neuro-fuzzy systems, and in situ verification. *Journal of Atmospheric and Oceanic Technology*, **17 (2)**, 140–164.

Marshall, J. S. and W. M. K. Palmer, 1948: The distribution of raindrops with size. *Journal of meteorology*, **5 (4)**, 165–166.

Matsui, T., et al., 2014: Introducing multisensor satellite radiance-based evaluation for regional earth system modeling. *Journal of Geophysical Research: Atmospheres*, **119 (13)**, 8450–8475.

Meischner, P., V. Bringi, D. Heimann, and H. Höller, 1991: A squall line in southern germany: Kinematics and precipitation formation as deduced by advanced polarimetric and doppler radar measurements. *Monthly weather review*, **119** (3), 678–701.

Mohr, C. G. and L. J. Miller, 1983: Cedric—a software package for cartesian space editing, synthesis and display of radar under interactive control. *Preprints*, American Meteorological Society, 569–574, 21st Conference on Radar Meteorology.

Nelson, S. P. and R. A. Brown, 1987: Error sources and accuracy of vertical velocities computed from multiple-doppler radar measurements in deep convective storms. *Journal of Atmospheric and Oceanic Technology*, **4** (1), 233–238.

NOAA, N. S. S. L., 2014: Dual-pol radar technology. URL http://www.nssl.noaa.gov/news/factsheets/Dual-pol_Fact_Sheet_2014.v5.pdf.

O'Brien, J. J., 1970: Alternative solutions to the classical vertical velocity problem. *Journal of Applied Meteorology*, **9** (2), 197–203.

O'Brien, V., 1961: Why raindrops break up-vortex instability. *Journal of Meteorology*, **18** (4), 549–552.

- Ray, P. S. and K. L. Sangren, 1983: Multiple-doppler radar network design. *Journal of climate and applied meteorology*, **22** (8), 1444–1454.
- Ray, P. S., C. L. Ziegler, W. Bumgarner, and R. J. Serafin, 1980: Single-and multiple-doppler radar observations of tornadic storms. *Monthly Weather Review*, **108** (10), 1607–1625.
- Rinehart, R. E., 2010: *Radar for Meteorologists*. 5th ed., Rinehart Publications.
- Ryzhkov, A., M. Pinsky, A. Pokrovsky, and A. Khain, 2011: Polarimetric radar observation operator for a cloud model with spectral microphysics. *Journal of Applied Meteorology and Climatology*, **50** (4), 873–894.
- Ryzhkov, A. V., S. E. Giangrande, V. M. Melnikov, and T. J. Schuur, 2005: Calibration issues of dual-polarization radar measurements. *Journal of Atmospheric and Oceanic Technology*, **22** (8), 1138–1155.
- Steiner, M., R. A. Houze Jr, and S. E. Yuter, 1995: Climatological characterization of three-dimensional storm structure from operational radar and rain gauge data. *Journal of Applied Meteorology*, **34** (9), 1978–2007.
- Thompson, E. J., S. A. Rutledge, B. Dolan, V. Chandrasekar, and B. L. Cheong, 2014: A dual-polarization radar hydrometeor classification algorithm for winter precipitation.

Journal of Atmospheric and Oceanic Technology, (2014).

Wang, Y. and V. Chandrasekar, 2009: Algorithm for estimation of the specific differential phase. *Journal of Atmospheric and Oceanic Technology*, **26** (12), 2565–2578.

Wilson, J. W. and R. D. Roberts, 2006: Summary of convective storm initiation and evolution during ihop: Observational and modeling perspective. *Monthly weather review*, **134** (1), 23–47.

Wu, J., A. D. Del Genio, M.-S. Yao, and A. B. Wolf, 2009: Wrf and giss scm simulations of convective updraft properties during twp-ice. *Journal of Geophysical Research: Atmospheres (1984–2012)*, **114** (D4).